学位論文

Suzaku Studies of Supernova Remnants
Hosting Non-Rotation-Powered Neutron Stars
(非回転駆動型の中性子星をもつ超新星残骸の「すざく」による研究)

平成26年12月 博士 (理学) 申請

東京大学大学院理学系研究科
物理学専攻 中野 俊男

Abstract

Core Collapse supernovae leave various kinds of neutron stars, including radio pulsars, central compact objects, and magnetars. Magnetars are a subclass of young neutron stars considered to have extremely strong magnetic fields, and keep their activities consuming the field energies instead of the rotational energy. While the number of known magnetars are rapidly increasing over last decade, their origin is still an open issue. In the same way as other neutron stars like canonical radio pulsars, magnetars must be produced by supernova explosions of massive stars. In fact, some magnetars are associated with supernova remnants (SNRs). Therefore, X-ray studies of magnetars-hosting SNRs are expected to provide valuable clues to the issue of what kinds of supernova explosion produce such strongly magnetized neutron stars.

For the above purpose, we chose the core-collapse SNR, CTB 109, which hosts, at its right center, the prototypical magnetar 1E 2259+586. The remnant has a peculiar half moon shape, possibly due to giant molecular clouds lying next to it. The 1E 2259+586/CTB 109 system was observed with the *Suzaku* observatory on two occasions, in 2009 and 2011. The observation successfully covered almost the entire remnant, including vicinity of the half moon edge. Utilizing the imaging spectroscopic capability of the X-ray Imaging Spectrometer onboard *Suzaku* , we derived spatial distribution of the basic parameters of the X-ray emitting plasma of CTB 109. There include the temperature, the emission measure, and the ionization state of some heavy ions and their abundances.

The X-ray study revealed that the giant molecular clouds obstructed the SNR expansion in the western diffraction, rather than absorbing X-ray emission. All over the SNR, the X-ray emission was found to consist of two plasma components with temperatures of 0.24 keV and 0.59 keV, which can be identified with shock-heated interstellar medium and stellar ejecta, respectively. The obtained plasma parameters enabled investigation into the explosion dynamics. The SNR was confirmed to be in the Sedov-adiabatic phase, and is expanding with a velocity of $\sim$ 450 kms^{-1}. From these and the emission measures, the mass of the progenitor and the explosion energy were derived as $\sim$ 39 $M_{\odot}$ and 0.7×10^{51} erg, respectively. Although the latter is rather ordinary as a core-collapse supernova, the former suggests that the progenitor was very massive, in agreement with some theoretical predictions. The high progenitor mass is supported also by the measured elemental abundances.

From the reconstructed SNR dynamics, and independently from the measured degree of plasma ionization, the age of the 1E 2259+586/CTB 109 system is estimated as 13 kyr. This reconfirms the previously reported discrepancy with the characteristic age of the magnetar, 230 kyr. The age discrepancy is considered to be caused by overestimation of the characteristic age of 1E 2259+586, rather than an underestimation of the age of CTB 109. Similar age overestimations are seen in other SNR-associated magnetars systems, compared with estimated age of their host SNRs.

Through analytic modeling of the magnetic field evolution of magnetars, we successfully solved that their characteristic age, calculated assuming a constant magnetic dipole, becomes systematically overestimated. This on one hand solves the age discrepancy in the 1E 2259+586/CTB 109 system, and on the other hand, agrees with the postulated nature of magnetars, since they are believed to keep shining as they consume the energy stored in their strong magnetic fields. This age estimation implies that magnetars are significantly younger than was considered so far. This inference is supported by the Galactic latitudinal distribution of magnetars, which is much narrower than those of radio pulsars. This feature raises a possibility that magnetars are produced more frequently by core-collapse supernovae with a much higher probability than previously thought, and they actually account for a considerable fraction of new-born neutron stars.

Contents

Chapter 1

Introduction

Core-collapse (CC) supernova (SN) explosions which take place when massive stars die, are one of the most energetic events in the Universe. The explosions release huge gravitational energies, and leave compact objects such as neutron stars (NS) or black holes. Although the energies are mostly carried away by neutrinos, the remaining energies, still large, are divided into the NSs and the ejected matters. The matter containing heavy elements synthesized in the progenitors or during the explosions are thrown into interstellar spaces with high velocities, and form supernova remnants (SNRs) through interactions with the surrounding medium. As SNRs expand, they sometimes collide with molecular clouds and mix ingredients to induce the formation of next-generation stars. The NSs store the inherited energies, heats, magnetic fields and rotation, and release them on different timescales through different mechanisms such as magnetic dipole radiation, thermal radiation and gravitational waves. Such circulations of matter and energies play an important role in the evolution of galaxies.

Over the last decade, diverse population of NSs have been gradually revealed by the progress of observational technologies. Among them, some new kinds of NSs, including magnetars, are considered to sustain their activity with different ways from the major rotation-powered pulsars. Instead of rotational energies, the magnetic field is considered to be the primary energy source of such *non-rotation-powered* NSs, Magnetars best represent the nature of such magnetically-powered NSs, because they exhibit peculiar activities that are difficult to explain without invoking their extremely strong magnetic fields. However, we do not yet understand what kind of mechanisms determine whether a newborn NS becomes magnetically-powered or rotation-powered.

Recently, the formation of magnetars are studied both observationally and theoretically. Some magnetars have been found to associate with young massive stellar clusters. This suggests that magnetars are produced by massive star with mass $30-50\ M_\odot$ (e.g., Figer et al. 2005), where $M_\odot$ is the mass of the Sun. The abundance pattern of a SNR associated with a magnetar also indicates their massive progenitors (Kumar et al., 2014). There is an opposite result that suggests a much lower progenitors mass of $\sim 17\ M_\odot$ (Davies et al., 2009). Hence, we do not have a consensus as to the types of the progenitor; or else, the progenitor mass may not be the

critical quantity. However, these estimates are somehow indirect, more direct measurements are needed.

In order to investigate the nature of magnetar formation directly, imaging spectroscopic observations of the CC SNR, CTB 109, was performed with *Suzaku* in 0.2-1.4 keV X-rays. The SNR has an association with the prototypical magnetar 1E 2259+586. We conducted spatially resolved X-ray spectroscopy of the SNR, and successfully obtained its plasma parameters, such as temperatures, densities, ionization state and abundances of elements. These observables allow us to estimate the mass of the progenitor, the explosion energy, and age of the system independently of the characteristic age of the magnetar. The comparison of these two age estimates gives us an opportunity to consider the evolution of the magnetic field of 1E 2259+586. Through these observational studies, we aim deepening our understanding of magnetars and their production mechanism.

Chapter 2

Review of Supernova Remnants

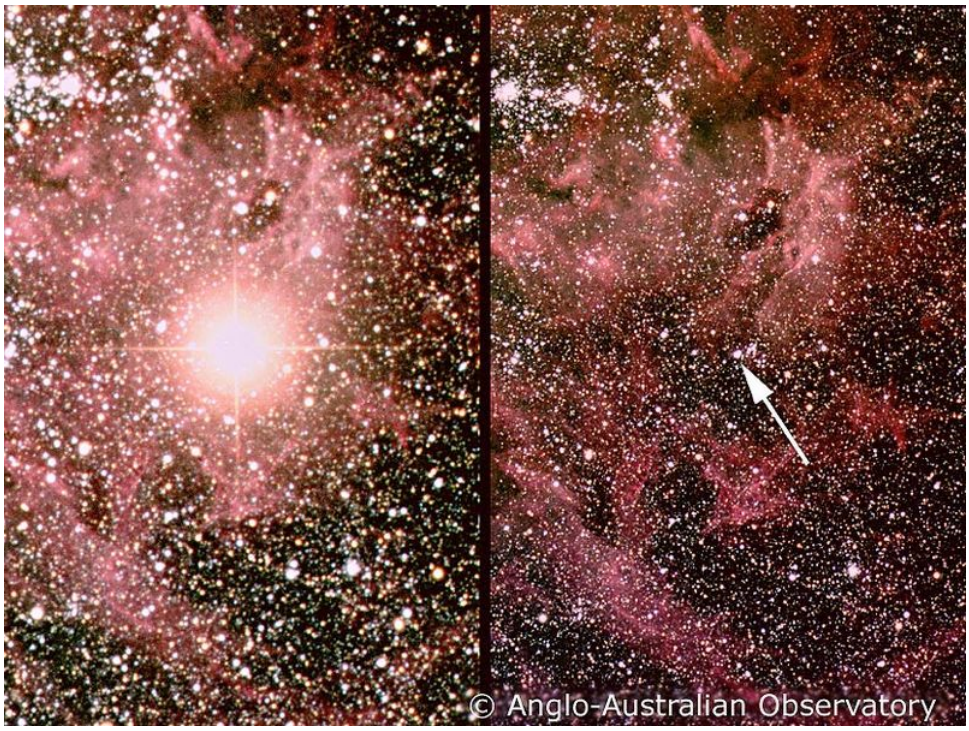

Figure 2.1: Pictures of the SN 1987A.

A supernova (SN) is explosion of a star at the end of its evolution and one of the most energetic events in the universe. The explosion energy is typically larger than 10^{51} erg and its brightness is comparable to that of whole galaxy as seen in figure 2.1 . They synthesize various heavy elements and release them into space. And in the cases of core collapse SNe of massive stars, the explosions leave compact stars such as neutron stars or black holes. In addition, SN explosions play a main role of evolution of galaxies.

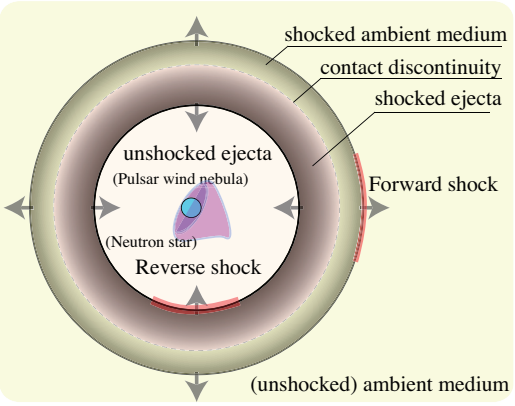

Figure 2.2: A schematic illustration of an SNR.

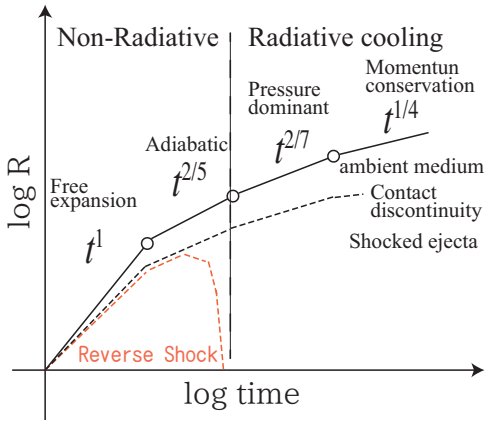

Figure 2.3: A schematic representation of the radius evolution of an SNR.

2.1 Structure and Evolution of Supernova Remnants

2.1.1 Structure

A supernova remnants is one of the products of a supernova explosion. In a narrow definition, a *Supernova remnant* (SNR) often means a diffused celestial object consisting of the shock heated plasmas as shown in figure 2.2. Generally, an SNR has the structures composed of a spherical shell and a filling ingredient.

At the front of the outer shell, a strong shock wave called blast wave or forward shock is propagating outside. Surrounding ambient matter is swept by the shock and involved into the shell. The temperature of the swept-up matter is raised to a few keV, which can emit X-ray (§2.3). There is a structure called a contact discontinuity that isolates the inner ingredient from the swept-up matter composing of the shell. The inner side of the contact discontinuity is filled by an ejecta component originating from progenitor star. The ejecta component is also heated by another shock called reverse shock, propagating from the contact discontinuity toward the center of the remnant. Then, the ejecta are heated up to emit X-ray.

A core-collapse SN explosion , observed as Type Ib,c and Type II, is thought to produce a compact object. Only neutron star species have been found in SNRs as pulsars, but black holes not yet. Some SNRs contain pulsar wind nebulae together with centered pulsars, for example 3C 58, PSR J1124-5916 in SNR G292.0+1.8 and PSR J1846-0258 in SNR Kes75. In contrast, SN 1054 as famous as Crab Pulsar (Nebula) show no emission from the shocked shell.

2.1.2 Evolution phase and expansion index of SNR

When an SN occurs, the matter is ejected into space at high velocities. The explosion produces a supernova remnant, which expands as it sweeps up the ambient matter such as interstellar medium (ISM) and circumstellar medium (CSM). An SNR consists of shock-heated plasmas

created by interactions between the ejecta and the swept-up matter. As illustrated in figure 2.3, the evolution of an SNR is divided into several distinct phases based on the ratios between the ejecta mass and the swept-up mass. In each phase, the shock radius $R_{\rm snr}$ evolves in proportion to a certain power β of time t after the explosion, and called the expansion index.

$$\beta \equiv \frac{d \ln R_{\rm snr}(t)}{d \ln t} , \tag{2.1}$$

where $R_{\rm snr}(t)$ and t are the radius and the time after the SN explosion, respectively (e.g., Chevalier 1974, 1977; Woltjer 1972).

2.1.3 Free expansion phase

The first stage of the SNR evolution is called free expansion phase, where the swept-up mass does not yet exceed the ejecta mass. The energy released by the SN is distributed into the ejecta mass $M_{\rm ej}$ as kinetic energy E_0. Thus the ejecta obtains a mean velocity $\upsilon_{\rm ej}$ as

$$E_0 = \frac{1}{2} M_{\rm ej} \upsilon_{\rm ej}^2 \Rightarrow \upsilon_{\rm ej} = \sqrt{\frac{2E_0}{M_{\rm ej}}} . \tag{2.2}$$

In this phase, the ejecta can freely expand into space, since the effect of swept-up matter is still negligible. The characteristic radius $R_{\rm snr}$ of the SNR (more correctly, of the outer shock) and its expansion velocity $\upsilon_{\rm snr}$ are hence described as

$$R_{\rm snr} = V_{\rm snr}\, t = \upsilon_{\rm ej} t. \tag{2.3}$$

The swept-up mass is described as

$$\begin{aligned} M_{\rm sw} &= \frac{4}{3}\pi\rho_0\, R_{\rm snr}^3 = \frac{4}{3}\pi\rho_0 \left(\upsilon_{\rm ej} t\right)^3 \\ &= \frac{4}{3}\pi\rho_0 \left(\frac{2E_0}{M_{\rm ej}}\right)^{3/2} t^3 \end{aligned} \tag{2.4}$$

where ρ_0 in this case means the ambient density. The SNR is growing in this phase until $M_{\rm sw}$ becomes comparable to $M_{\rm ej}$. The characteristic radius and the associated time at the transition from this to the next phase is hence given from $M_{\rm sw} = M_{\rm ej}$ in equation 2.4 as

$$R_{\rm I\to II} = \left(\frac{3}{4\pi}\frac{M_{\rm ej}}{\rho_0}\right)^{1/3} \sim 1.9 \times \left(\frac{M_{\rm ej}}{M_\odot}\right)^{1/3} \left(\frac{n_0}{\rm cm^3}\right)^{-1/3} \ {\rm pc} \tag{2.5}$$

$$t_{\rm I\to II} = \frac{R_{\rm I\to II}}{V_{\rm snr}} \sim 2 \times 10^2 \times \left(\frac{M_{\rm ej}}{M_\odot}\right)^{1/3} \left(\frac{n_0}{\rm cm^3}\right)^{-1/3} \left(\frac{V_{\rm snr}}{10^4\ {\rm km\cdot s^{-1}}}\right)^{-1} \ {\rm yr}. \tag{2.6}$$

Here, we hare employed a relation $\rho_0 = 1.2 m_{\rm P} n_0$ (assuming solar abundance), where n_0 is the number density and $m_{\rm p}$ is the proton mass. Typically, the transition occurs when the SNR radius reaches 2 pc, in 200 years after the explosion.

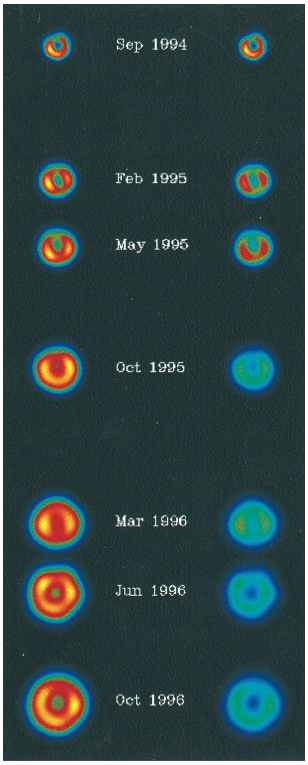

Figure 2.4: A sequence of radio images of SN 1993J (1994-1996) taken from Marcaide et al. (1997).

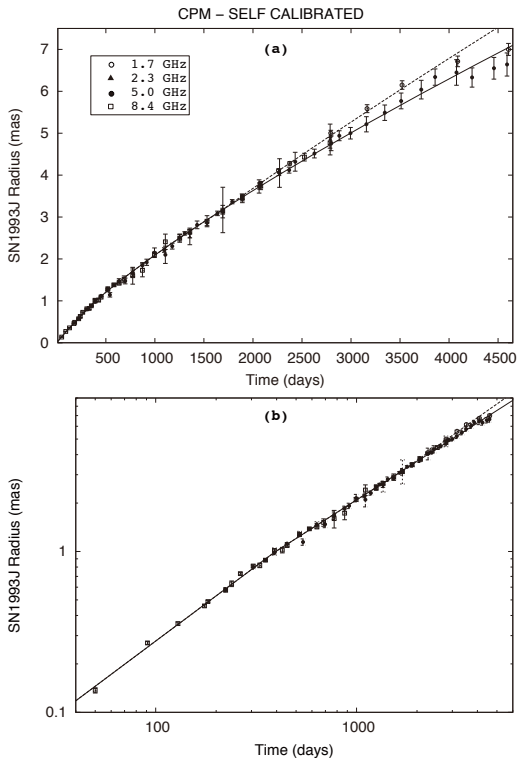

Figure 2.5: Expansion of SN 1993J (1993-2005) taken from Martí-Vidal et al. (2011)

To be more realistic, the expansion is decelerated gradually by the swept-up mass, thus β changes from 1 to 0.4, and the SNR comes into the next stage. Observationally, Marcaide et al. (1997) find deceleration in expansion of SN 1993J (Ripero et al., 1993) by using VLBI (Very-Long-Baseline-Interferometry) observations. Figure 2.4 is a sequence of radio images of SN 1993J which clearly reveals the expansion of this SNR, and figure 2.5 represents evolution of the SN as a function of time. A value of $\beta = 0.85$, which is somewhat smaller than that of the ideal free expansion, is reported by some papers (see details; Marcaide et al. 2009; Martí-Vidal et al. 2011), indicating that the deceleration has already started.

2.1.4 Adiabatic phase (Sedov-Taylor phase)

When $M_{\rm sw}$ becomes larger than $M_{\rm ej}$, the SNR enters the second stage. Since radiative losses are still negligible in this phase, the SNR can be considered as adiabatic, and this phase is called adiabatic phase. A similarity solution assuming a point-like explosion in a uniform ambient density was obtained independently by Taylor (1950) and Sedov (1959). Thus, this phase is alternatively called Sedov phase or Sedov-Taylor phase. Shklovskii (1962) applied the solution to the SN(SNR) evolution. In this stage, the SNR evolution is solved by dimensional analysis

as

$$R_{\rm snr} = \xi \left(\frac{E_0}{\rho_0}\right)^{1/5} t^{2/5} \tag{2.7}$$

and

$$V_{\rm snr} = \frac{dR_{\rm snr}}{dt} = \frac{2}{5}\frac{R_{\rm snr}}{t} \, . \tag{2.8}$$

Here, ξ is a dimensionless constant, and the Sedov-Taylor solutions give $\xi_{st} = 1.15$ for non-relativistic ideal gases with an adiabatic index of $\gamma = 5/3$. The temperature behind the shock front is determined by the Rankine-Hugoniot relations at high Mach number, described later in equation (2.33), as

$$T(R,t) = \frac{3}{4 \cdot 5^2}\xi^2 \left(\frac{E_0}{\rho_0}\right)^{2/5} t^{-6/5} \, . \tag{2.9}$$

The initial condition affecting the SNR evolution is only the ratio (E_0/ρ_0), because $M_{\rm ej}$ is negligible. Eliminating t from equation 2.7 and 2.8, the explosion energy E_0 is described as

$$E_0 = \left(\frac{5}{2}\right)^2 \xi^5 \, \rho_0 R_{\rm snr}^3 \, V_{\rm snr}^2 \, . \tag{2.10}$$

The forward shock is decelerated by the swept-up mass, and the deceleration produces revers shock which propagates backwards in the ejecta and ultimately reach the center of the SNR (McKee, 1974). Although neither the reverse shock nor the contact discontinuity are considered by the Sedov-Taylor solutions, it can be modified into a more general form, which can analytically take into account the two features. In the modified model, equation (2.7) is generalized as

$$\begin{aligned} R_{\rm snr} &= \xi_{\rm ch} \, t^{\,\beta} \\ \beta &\equiv \frac{n-3}{n-s} \, . \end{aligned} \tag{2.11}$$

Here, density distributions of the ejecta and ambient matter are both assumed to be described as power-law functions of the radius r ($\rho_{\rm ej} \propto r^{-n}$ and $\rho_{\rm am} \propto r^{-s}$). For an SNR formed in a wind-bubble produced by the massive progenitor, $s = 2$ is a good approximation to the ambient CSM distribution ($\rho_{\rm cms} = \dot{M}/4\pi v_{\rm w} r^2$) where $\dot{M}$, $v_{\rm w}$ and $\rho_{\rm cms}$ are mass loss rate and wind velocity of the progenitor, and the density of CMS, respectively. The case of $n = 7$ is appropriate for the ejecta structure of Type Ia SNe, and that of $n = (9-12)$ is a good approximation for CC SNe. Chevalier (1982) studied self-similar solutions for this model, and analytically calculated detail structures around the contact discontinuity to derive the results as shown in (figure 2.6). Truelove & McKee (1999) conducted analytic and numerical studies of the dynamical evolution of SNRs, and showed trajectories of the reverse shock as again in figure 2.7. The solution gives a smooth transition from the free expansion phase to the adiabatic phase (as non-radiation phase), and its β asymptotically approaches 2/5 as specified by the original Sedov-Taylor solutions.

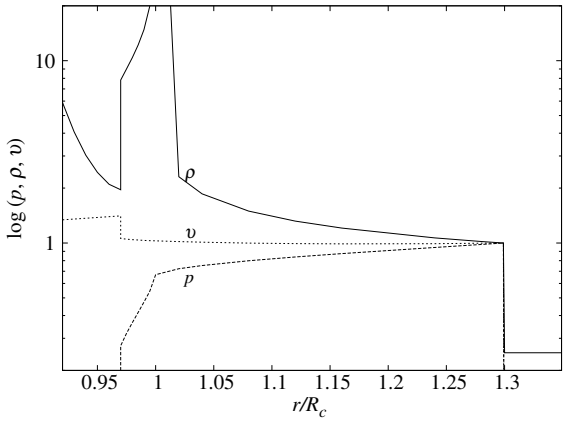

Figure 2.6: The structure around the contact discontinuity obtained by a self-similarity solution for $n = 2$ and $s = 12$ (Chevalier, 1982). Solid line, dashed line and dotted line correspond to density, velocity and pressure, respectively. All quantities have been normalized to the values at the forward shock.

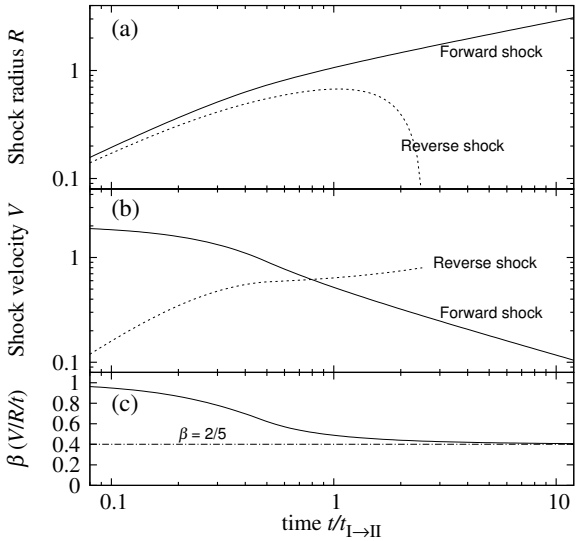

Figure 2.7: The trajectory of an SNR evolution taken from an analytical model of Truelove & McKee (1999). Solid lines represent quantities of the forward shock, and dotted lines those of the reverse shock. Panel (a) shows the radius profiles and Panel (b) the velocity profiles. Reverse shock velocity is plotted in the frame of the unshocked ejecta ahead of it. Panel (c) show index, $\beta = V/(Rt)$.

2.1.5 Radiative Phase

When the age of the SNR becomes much larger than the cooling time of its plasma, the adiabatic phase does not last any longer, since radiative cooling cannot be neglected. The time scale of cooling is given, e.g., by Blondin et al. (1998) as

$$\tau_{\rm cool} = \frac{3/2kT}{8n_0\Lambda} = \frac{0.69\ kT}{n_0\Lambda}. \tag{2.12}$$

Here, n_0 is the plasma density, and Λ is a quantity called cooling function, to be explained later. Since SNRs consist of optically-thin thermal plasmas, their radiative energy loss is proportional to their volume and Λ as

$$L_{\rm rad}\,(T) = \frac{16\pi}{3}R^3 n_0^2 \Lambda(T). \tag{2.13}$$

Here, we assumed that the emission volume is a spherical shell with a thickness $\delta r = R/12$.

When the temperature is relatively high ($T \geq 10^{7.5}$) and the chemical abundance of the plasma is not much higher than the Solar value, the cooling process is dominated by the thermal Bremsstrahlung, and we can write analytically as

$$\Lambda(T) = 1.0 \times 10^{-23} \left(\frac{T}{\rm keV}\right)^{0.5} \ {\rm ergs^{-1}cm^3}. \tag{2.14}$$

However, at lower temperatures, line emission process from various ion species become dominant, and hence $\Lambda(t)$ can no longer be calculated analytically; details need to be studied under numerical calculations (e.g., Kaastra & Jansen 1993; Masai 1984; Raymond & Smith 1977; Schure et al. 2009; Sutherland & Dopita 1993). Figure 2.8 shows one of such examples. As indicated therein, $\Lambda(T)$ can be approximated, for $T > 10^{5.5}$, as

$$\begin{aligned} \Lambda(T) &\sim C_{-0.7}T^{-0.7} + C_{0.5}T^{0.5} \\ &\sim 2.5 \times 10^{-23} \left(\frac{T}{\rm keV}\right)^{-0.7} + 1.0 \times 10^{-23} \left(\frac{T}{\rm keV}\right)^{0.5} \end{aligned} \tag{2.15}$$

where the second term is simply identical to equation 2.14. Combined with the time dependence of $T \propto t^{-6/5}$ (equation 2.9) and $R \propto t^{0.4}$ (2.7), the radiative luminosity $L_{\rm rad}$ is approximately proportional to $t^{0.6}$ for $T > 2$ keV and $t^{2.4}$ for $T < 2$ keV. After the temperature drops to a few keV, the shocked matter dramatically cools down.

Assuming that a certain fraction of η of the expansion energy E_0 (excluding the neutrino loss), is converted into thermal energy of the SNR, and then radiated away with a time-dependent luminosity $L_{\rm cool}$, we can write as

$$\int_0^{t_{\rm cool}} L_{\rm cool}(t)\ dt = \eta E_0. \tag{2.16}$$

Then, if we choose the first term of equation 2.15 and assume $\eta = 0.3$, the cooling time $t_{\rm cool}$ becomes

$$t_{\rm II\to III} \sim 3 \times 10^4 \left(\frac{E_0}{10^{51}\ {\rm erg}}\right)^{0.22} \left(\frac{n_0}{\rm cm^3}\right)^{-0.55} \ {\rm year}\ . \tag{2.17}$$

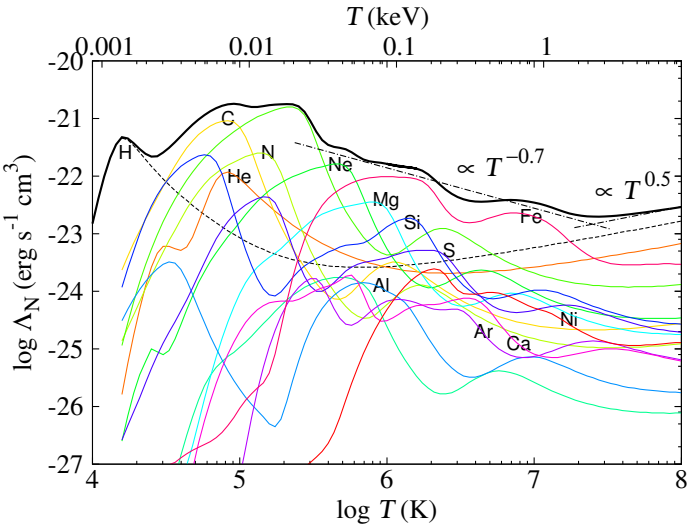

Figure 2.8: The cooling function Λ calculated by Schure et al. (2009). The black solid line indicates the total emission, while each colored line shows contributions from individual element.

At that time, the radius of the SNR becomes, from equation 2.7,

$$R_{\mathrm{II}\to\mathrm{III}} \sim 20 \left(\frac{E_0}{10^{51}\mathrm{erg}}\right)^{0.29} \left(\frac{n_0}{\mathrm{cm}^3}\right)^{-0.42} \ \mathrm{pc}\ . \tag{2.18}$$

The SNR has a cool-dens shell, but the plasma inside that region still has a high temperature and a high pressure. Thus the inner plasma expands adiabatically ($pV^{3/5} \sim$ constant). In this case, the pressure of the inner plasma is described as

$$p_1 = 0.35 \times \frac{2E_0/3}{(4\pi/3)R^3}. \tag{2.19}$$

As a result, the equation of motion for the shell becomes

$$\frac{d}{dt}\left(\frac{4\pi}{3}R^3\rho_0 V_{\mathrm{snr}}\right) = 4\pi R^2 p_1 \left(\frac{R}{R_{\mathrm{II}\to\mathrm{III}}}\right)^{-5}. \tag{2.20}$$

Integrating this, we can obtain the radius expansion (McKee & Ostriker, 1977) as

$$R_{\mathrm{snr}}(t) = \left[\frac{5.15}{4\pi}\left(\frac{E_0}{\rho_0}\right)R_1^2\right]t^{2/7}. \tag{2.21}$$

This phase is called pressure-drive snowplow phase (figure 2.3).

As the SNR further expands, the inner plasma becomes cooler and its pressure becomes negligibly small. In this case, we can apply momentum conservation to the expansion formula as

$$\left(\frac{4\pi}{3}\right)R^3\rho_0\dot{R} = \left(\frac{4\pi}{3}\right)R_2^3\rho_0 R\dot{R}^2 \tag{2.22}$$

and integrating this, we obtain

$$R_{\mathrm{snr}}(t) = R_2\left[1 + \frac{4\dot{R}_2}{R_2}(t - t_2)\right]^{1/4}. \tag{2.23}$$

In this phase, the SNR expand as $\propto t^{1/4}$ (figure 2.3).

When the expansion velocity of the SNR becomes comparable to the sound velocity of the ISM, shock waves can no longer persist, and the SNR gradually merges into ISM and disappears. This is called disappearance phase.

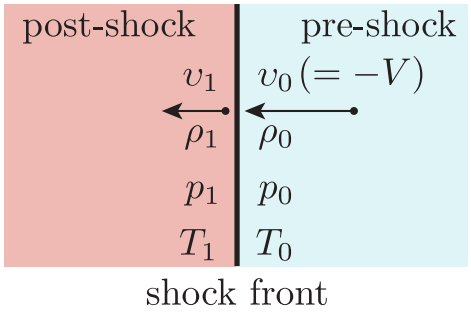

Figure 2.9: Configuration of a shock front, as seen from the shock rest frame.

2.2 Physics of Supernova Remnants

2.2.1 Shocks and Rankine-Hugoniot relations

As detailed in §2.1.1, the expansion velocity of SNRs typically reaches $1000 - 10000\ \mathrm{km \cdot s^{-1}}$, which is much higher than the sound velocity of the inter stellar medium. Mach number of an object moving with velocity v is defined using the sound velocity of the medium $a = (\gamma p/\rho)^{1/2}$ as

$$\mathcal{M} \equiv \frac{v}{a} = v\left(\frac{\gamma p}{\rho}\right)^{-1/2} = v\left(\frac{\gamma kT}{\bar{m}}\right)^{-1/2}, \tag{2.24}$$

where p, ρ , T and $\bar{m}$ respectively represent pressure, density, temperature, and mean particle mass of the medium. While $\mathcal{M}$ is low (≤ 0.5), such a system can be described as a simple incompressible fluid where sound waves propagate. However, when $\mathcal{M}$ becomes high (e.g., ≥ 0.5), like expanding SNRs, we need to consider the formation of a shock discontinuity and its propagation in the forms of shock waves. In this section, we briefly introduce the physics of shocks which play a significant role in SNRs, such as plasma heating and particle acceleration.

We consider a perpendicular shock wave (i.e., the shock front is perpendicular to the flow direction) and employ the shock rest frame. The subscripts 0 and 1 represent *pre-shock* and *post-shock* regions, respectively. Across the shock front, namely, the boundary between the post and pre shock regions, the conservation of mass, momentum and energy must be satisfied. For ideal gases, these relations are described respectively as

$$\rho_0 v_0 = \rho_1 v_1 \tag{2.25}$$

$$\rho_0 v_0^2 = \rho_1 v_1^2 \tag{2.26}$$

$$\frac{1}{2}v_0^2 + \frac{\gamma}{\gamma - 1}\frac{p_0}{\rho_0} = \frac{1}{2}v_0^2 + \frac{\gamma}{\gamma - 1}\frac{p_1}{\rho_1}. \tag{2.27}$$

We can define the compression ratio $\mathcal{X}$ and pressure ratio $\mathcal{Y}$, and using them together with $\mathcal{M}_0 = v_0/a_0$, the above equations are transformed into more useful forms as

$$\mathcal{X} \equiv \frac{\rho_1}{\rho_0} = \frac{v_0}{v_1} = \frac{(\gamma - 1)\, p_0 + (\gamma + 1)\, p_1}{(\gamma + 1)\, p_0 + (\gamma - 1)\, p_1} = \frac{(\gamma + 1)\, \mathcal{M}_0^2}{(\gamma - 1)\, \mathcal{M}_0^2 + 2}, \tag{2.28}$$

and

$$\mathcal{Y} \equiv \frac{p_1}{p_0} = \frac{2\gamma\mathcal{M}_0^2 - (\gamma - 1)}{\gamma + 1}. \tag{2.29}$$

Incorporating the equation of state for an ideal gas, the temperature ratio $\mathcal{Y}/\mathcal{X}$ can be expressed as

$$\frac{T_1}{T_0} = \frac{p_1}{\rho_1} \cdot \frac{\rho_0}{p_0} = \frac{\left[2\gamma\mathcal{M}_0^2 - (\gamma - 1)\right]\left[(\gamma - 1)\,\mathcal{M}_0^2 + 2\right]}{(\gamma + 1)^2\,\mathcal{M}_0^2}. \tag{2.30}$$

For the case of SNR physics, strong shocks with $\mathcal{M}_0 \gg 1$ and $\gamma = 5/3$ are important. Then, the limiting case of equation (2.28) and equation (2.27) can give useful information as

$$\mathcal{X} = \frac{\gamma + 1}{\gamma - 1} = 4 \quad \Rightarrow \quad \rho_1 = 4\,\rho_0 \tag{2.31}$$

$$\mathcal{Y} = \frac{2\gamma}{\gamma + 1}\mathcal{M}_0^2 \quad \Rightarrow \quad p_1 = \frac{3}{4}\rho_0 v_0^2 = \frac{3}{4}\mu_0 m_\mathrm{p} n_0 v_0^2 \tag{2.32}$$

$$\mathcal{Y}/\mathcal{X} = \frac{2\gamma\,(\gamma - 1)}{(\gamma + 1)^2}\mathcal{M}_0^2 \quad \Rightarrow \quad kT_1 = \frac{3}{16}\mu_1 m_\mathrm{p} v_0^2\,. \tag{2.33}$$

Interestingly, equations (2.31) and (2.32) mean that the density of the shocked medium is determined only by that of the pre-shocked medium. Since $\rho_0 v_0^2$ in equation (2.32) virtually works as pressure, the term ρv^2 is called *ram pressure*. These relations specify how these physical quantities make discontinuous jumps across the shock fronts of SNRs.

While a shock front is characterized by significant jumps in the density, pressure and the temperature, an SNR also involves another form of characteristic boundary, called contact discontinuity (§2.1.1). As illustrated in figure 2.2, this forms at an interface between the expanding ejecta and the ambient medium, and is characterized as

$$\rho_0 \neq \rho_1,\ p_0 = p_1,\ v_0 = v_1 = 0 \tag{2.34}$$

in its rest frame. Thus, the density jumps, but the pressure and velocity are continuous across the interface.

2.3 Radiation Process and Characteristics of X-ray Spectra

Since plasmas comprising SNRs with $T = 10^{6.5-7.5}$ K efficiently emit high energy photons in the X-ray band and are optically thin for the emitted photons, X-ray spectroscopy is one of the strongest ways to probe the plasma conditions of SNRs, such as the temperatures, ionization states and chemical abundances. A spectrum from a thin thermal plasma consists of a continuum due to thermal Bremsstrahlung, and many characteristic emission lines due to ionized atoms. The shape of continuum is mainly determined by the electron temperature, and the emission lines provide crucial information on abundances of elements. Relations between the continuum temperature and line ratios for each element allow us to estimate the ionization state of the plasma.

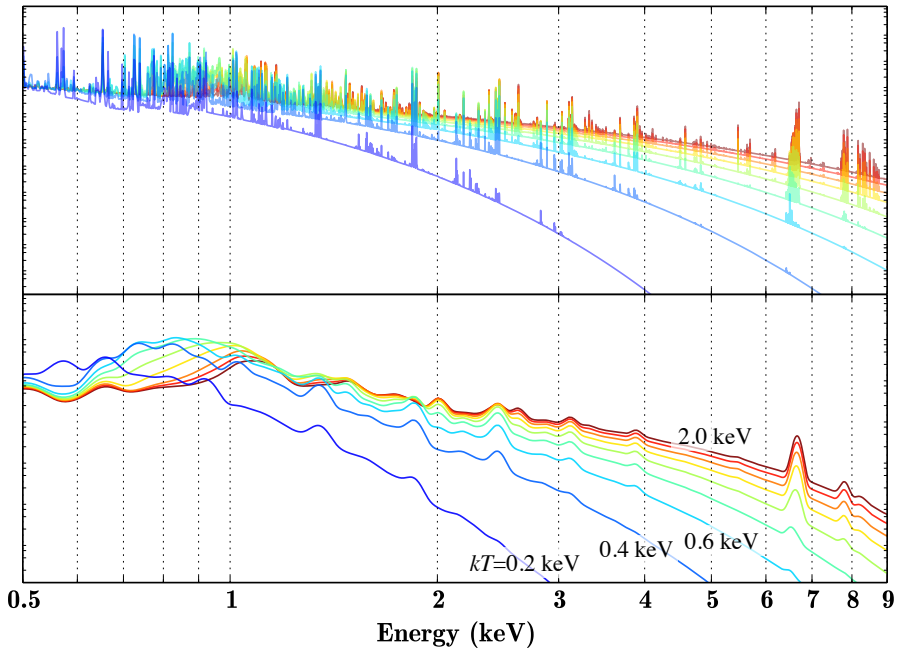

Figure 2.10: Examples of model X-ray spectra from a thin thermal plasma in full equilibrium, calculated by APEC code. Panel (a) shows the incident spectra. Panel (b) is the same but convolved with the *Suzaku* XIS response. The spectra are plotted for a temperature from 0.2 keV to 2.0 keV with 0.2 keV step, with the colors changing from blue to red.

2.3.1 Bremsstrahlung

When a charged particle is accelerated, it radiates electromagnetic waves. Bremsstrahlung (free-free emission), the emissions from electrons moving and accelerated in the Coulomb fields of other heavy charged particles, dominates in the continuum spectrum of a thin-thermal plasma. Since the velocities of ions are smaller than those of electrons (in equilibrium $\bar{v}_\mathrm{p}/\bar{v}_\mathrm{e} = \sqrt{m_\mathrm{e}/m_\mathrm{p}}$), and their q/m ratios (where m is the mass and q is the electric charge) are also small, we need to consider only motions of electrons; heavy ions are considered immobile and their radiation is negligible here.

For a moving charged particle, the radiated energy per unit angular frequency ω is described by

$$\frac{dW}{d\omega} = \frac{2}{3\pi c^3}\left(\frac{q}{m}\right)^2 \left|\tilde{\boldsymbol{F}}(\omega)\right|^2 \tag{2.35}$$

where c is the light velocity and $\boldsymbol{F}(\omega)$ is the electromagnetic force. Employing the straight line approximation for the motion of an electron, the Coulomb force from a heavy ion is described as

$$\boldsymbol{F}_\mathrm{c}(t) = -Ze^2\frac{\boldsymbol{b}+\boldsymbol{v}t}{|\boldsymbol{b}+\boldsymbol{v}t|^3} \Rightarrow \tilde{\boldsymbol{F}}_\mathrm{c}(\omega) = \int_{-\infty}^{\infty} dt\, e^{-i\omega t}\boldsymbol{F}_\mathrm{c}(t). \tag{2.36}$$

where $\boldsymbol{b}$ is impact parameter. Substituting this into equation (2.35), we obtain bremsstrahlung spectrum of a single interaction between an electron and an ion as

$$\frac{dW}{dt} \simeq \frac{8Z^2e^6}{3\pi m_e^2 c^3 v^4}\begin{cases} \left(\dfrac{v}{b}\right)^2 & \dfrac{b\omega}{v} \ll 1 \\ \dfrac{\pi}{2}\left(\dfrac{v\omega}{b}\right)\exp\left[-2\left(\dfrac{b\omega}{v}\right)\right] & \dfrac{b\omega}{v} \gg 1\,. \end{cases} \tag{2.37}$$

This formula considers a monochromatic electron and does not take into account the thermal distribution of electrons in a plasma or the distribution of b. A more realistic expression for the spectra of thermal bremsstrahlung is described by using gaunt factor $\bar{g}_{ff}$(Gaunt, 1930) which gives corrections for the continuum emission and absorption. Using it, the spectral volume emissivity (radiation energy emerging from a unit volume in a unit time per unit photon energy) is givens as

$$\epsilon_\mathrm{br} = \frac{dW}{d\nu dV dt} = \sum_i \frac{2^5}{3}\frac{Z_i^2 n_i n_e e^6}{(m_e c^2)^2}\sqrt{\frac{2\pi}{3}\left(\frac{m_e c^2}{kT}\right)}\,\bar{g}_{ff}(h\nu : kT)\exp\left(-\frac{h\nu}{kT}\right) \quad \mathrm{erg\ cm^{-3}\ Hz^{-1}} \tag{2.38}$$

where $\bar{g}_{ff}$ is a correction factor called Gaunt factor. It is approximated as

$$\bar{g}_{ff}(kT) \simeq \begin{cases} \dfrac{\sqrt{3}}{\pi}\ln\left(\dfrac{2}{\Gamma}\dfrac{kT}{h\nu}\right) & \dfrac{h\nu}{kT} \ll 1 \\ 1 & \dfrac{h\nu}{kT} \gg 1\,. \end{cases} \tag{2.39}$$

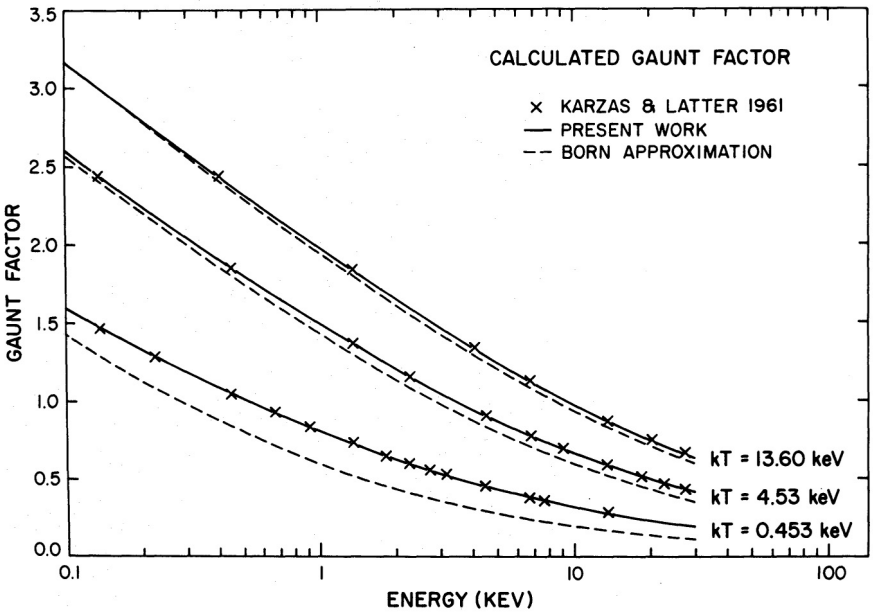

Figure 2.11: The photon-energy distribution of the Gaunt factor, calculated for several temperature by different authors (from Kellogg et al. 1975)

Figure 2.11 exemplifies the Gaunt factor for several conditions (e.g., Hummer 1988; Karzas & Latter 1961; Nozawa et al. 1998). In the `bremss` model of `xspec`, a standard X-ray spectroscopic software, the calculation of Kellogg et al. (1975) is used, which first applied the Gaunt factor of Karzas & Latter (1961) to plasma emissions of cluster of galaxies. If $h\nu \sim kT \sim 1$ keV which is relevant to SNRs, neither of the two approximations of equation 2.39 is valid. Instead, as shown in figure 2.11, we can approximate as $g(h\nu; kT) \propto (h\nu)^{-0.3} \times g'(kT)$, where g' is a function of kT only. Then, equation (2.38) reduces to

$$\epsilon(h\nu : kT) \propto g'(kT)(kT)^{-1/2}(h\nu)^{-0.3} \exp\left(-\frac{h\nu}{kT}\right) \tag{2.40}$$

so that the continuum has an approximately exponential shape. Integration of this equation over $h\nu$ gives the cooling function of equation (2.14)

2.3.2 Recombination continua

When a free electron is captured into an atomic shell of ions, a photon is emitted; this process is called *free-bound emission* or *recombination radiation* (Tucker & Gould, 1966). The emitted photon has an energy which is equal to a sum of the initial kinematic energy of the electron and ionization potential χ_n binding the electron. The spectrum of this process is given as

$$\epsilon_{\rm rrc} = \sqrt{\frac{2}{\pi}}\, n_e n_{z+1} \frac{g_i}{g_{i+1}} c\sigma(h\nu)\left(\frac{h\nu}{\chi_n}\right)\left(\frac{\chi_n^2}{m_e c^2 kT}\right)^{3/2} \times \exp\left[-\frac{(h\nu - \chi_n)}{kT_e}\right] \text{ erg s}^{-1}\text{cm}^{-3}\text{Hz}^{-1} \quad (h\nu \geq \chi_n), \tag{2.41}$$

where n_{z+1} is the density of an ion with charge $z+1$, g_{z+1} and g_z are statistical weights of the ion before and after this process, and $\sigma(h\nu)$ is the photoionization cross section of the final state of the ion (see also good review by Vink 2011). These continua have slopes similar to those of thermal bremsstrahlung radiation, but also characteristic edge structures, called recombination edge, corresponding to χ_n. This is the most outstanding characteristic of the spectra of this radiation, so called radiative-recombination continua (RRCs), and has been identified in X-ray spectra of several evolved SNRs by *Suzaku* (e.g., IC 443 by Yamaguchi et al. 2009; W49B by Ozawa et al. 2009).

2.3.3 Line emission

Collisional excitations and radiative deexcitations recur in SNR plasmas. Deexcitations between two discrete quantum levels causes photon emission called *line emission* or *bound-bound emission*. As a result, narrow emission lines are produced in a spectrum at the corresponding energy. For hydrogen-like (H-like) ions, the energy of photons emitted by transition between principal quantum numbers n and n' is governed by a relation known as *Moseley's law*,

$$E_{nn'} = Z^2 R_{\rm y} \left(\frac{1}{n^2} - \frac{1}{n'^2} \right) \tag{2.42}$$

where Z is charge number of the ion, and $R_{\rm y} = 13.6$ eV is the Rydberg constant. If $n = 1$ and $n' \geq 2$, these lines are called *Lyman series*. These energies further split due to by the azimuthal quantum number, into multiple lines specified by subscripts α, β and γ.

Ions with more than two electrons have more complicated line structures. For example, He-like ions have three intense lines, namely, resonance (K$\alpha_{\rm r}$:$1s2p\ ^3{\rm P}_1 \rightarrow 1s^2\ ^1{\rm S}_0$), forbidden (K$\alpha_{\rm f}$:$1s2s\ ^3{\rm S}_1 \rightarrow 1s^2\ ^1{\rm S}_0$) and inter-combination (K$\alpha_{\rm i}$: $1s2p^3{\rm P}_{2,1} \rightarrow 1s^2\ ^1{\rm S}_0$) lines, as illustrated in figure 2.12. When ignoring such fine structures, the line energies for ions with more than one electrons can be approximately described, by generalizing equation 2.42, as

$$E_{nn'} = (Z - \eta)^2 R_{\rm y} \left(\frac{1}{n^2} - \frac{1}{n'^2} \right) \tag{2.43}$$

where η is a correction factor describing the effects of electrostatic shielding; $\eta = 0$ for H-like ions, $\eta \simeq 0.4$ for He-like ones, and $\eta \simeq 1.0$ for neutral atoms.

2.4 Temperatures and equilibria

In the simplest hydrogenic plasma in a thermal equilibrium, both electrons and ions have Maxwellian distributions, and their common temperature is givens as

$$kT = \frac{3}{2} m_p \left\langle v_p^2 \right\rangle = \frac{3}{2} m_e \left\langle v_e^2 \right\rangle . \tag{2.44}$$

However, in SNR plasmas, we need to pay attention to two additional complications. One is that electrons and ions can have different temperatures, and the other is that heavy ions can have three separate definitions of "temperature".

Table 2.1: Energies (in eV) of emission lines from major elements.

Element	Line energy (eV)							
	H-like			He-like				
	Lyα	Lyβ	Lyγ	Kα_r	Kα_f	Kα_i	Kβ	Kγ
C	367	436	459	308	299	204	355	371
N	500	593	625	431	420	426	498	522
O	654	774	817	574	561	569	666	698
Ne	1022	1211	1277	921	905	914	1073	1127
Mg	1472	1745	1840	1352	1330	1343	1579	1660
Si	2006	2377	2506	1865	1840	1854	2183	2294
S	2623	3107	3277	2461	2431	2447	2884	3033
Ar	3323	3936	4151	3140	3104	3124	3685	3875
Ca	4106	4864	5130	3908	3845	3892	4582	4918
Fe	6966	8266	8732	6702	6641	6670	7798	8217

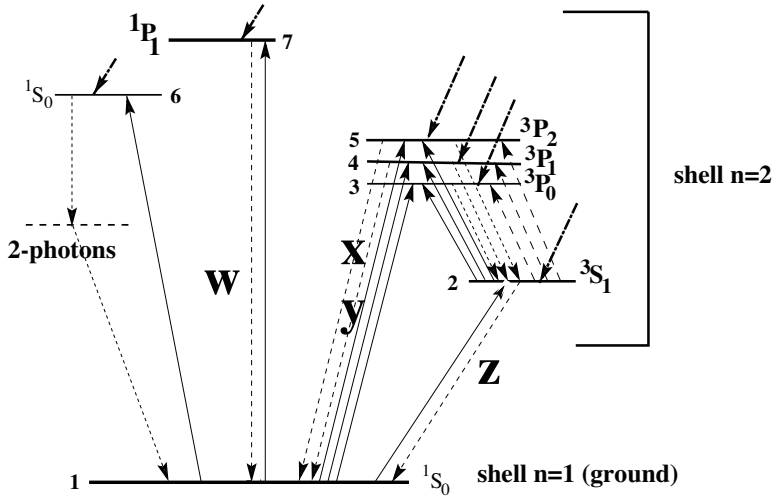

Figure 2.12: Simplified Grotrian diagram of He-like ions taken from Porquet et al. (2001). **w** is resonance, **x** and **y** are intercombination, and **z** is forbidden transition.

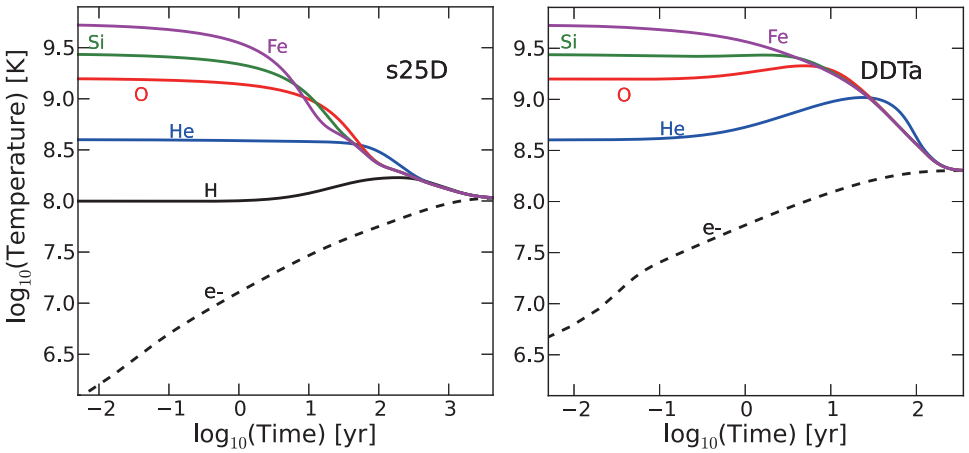

Figure 2.13: The evolution of electron and ion temperatures in SNRs calculated by Lee et al. (2014). Left is for a CC-SN assuming element abundance "s25", while right is for a Type Ia SN with abundance "DDTa".

2.4.1 Electron and ion temperatures

In SNR plasmas (§2.2.1), generally, heavy particles such as protons and ions are first heated by the strong shock, and obtain temperature $kT_{\rm p} = (3/16)\, m_{\rm p} v_{\rm p}^2$. Later, electrons are gradually heated by ions, finally a thermal equilibrium is achieved. The time scale of an equilibration between two different particles (Spitzer, 1962) is given by

$$\tau_{\rm eq} = \frac{3}{8\sqrt{2\pi}} \frac{m_i m_j}{n_j Z_i^2 Z_j^2 e^4 \log\beta} \left(\frac{kT_i}{m_i} + \frac{kT_j}{m_j} \right)^{3/2}, \tag{2.45}$$

where subscripts i and j represent the two particle species, m means particle mass, n is the number of density, and $\log\beta = \log(b_{\rm max}/b_{\rm min})$ is the pair of the coulomb impact factor. If electrons (of mass $m_{\rm e}$) and ions of mass M_i have relatively similar temperature, the electron-electron, ion-ion, and ion-electron equilibrium time scales scale as

$$\tau_{\rm ee} : \tau_{\rm ii} : \tau_{\rm ie} = 1 : \sqrt{\frac{M_{\rm i}}{m_{\rm e}}} : \frac{M_{\rm i}}{m_{\rm e}}.$$

Figure 2.13 is a recent calculation, by Lee et al. (2014), and show the temperature evolution toward the equilibrium for some elements. Since measuring the ion temperature is difficult, thermal equilibration behind the shock of SNRs has not been well understood yet.

2.4.2 Non-equilibrium ionization

In addition to the ordinary "kinetic" temperature defined by equation (2.44), a heavy ion species has two more temperatures; excitation temperature, and ionization temperature. The number ratio between the ionization states i and $i+1$ in an equilibrium plasma is given by the *Saha* equation as

$$\frac{n_{i+1}}{n_i} = \frac{Z_{i+1}}{Z_i} \exp\left(-\frac{\mu_e + I_i}{kT_z} \right), \tag{2.46}$$

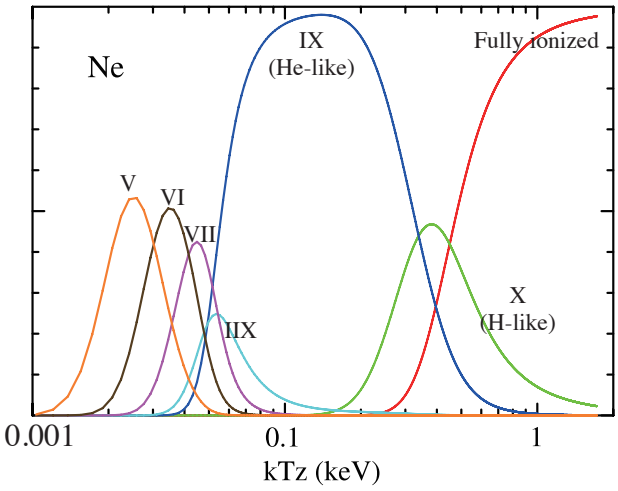

Figure 2.14: Fractions of Ne ions of various ionization states, shown against the ionization temperature, taken from Ozawa (2010). A plasma with higher ionization temperature has larger fractions

where T_z is defined as ionization temperature, μ_e is the chemical potential for non degenerate free electrons, and $Z_{i+1,i}$ is statistical weight of each ionization state. Figure 2.14 shows how the fractions of different ionization states change as a function of T_Z, taking Ne as an example. We can see that the He-like state is dominant over a wide T_Z range, because of the stability of its electric configuration. In SNR plasmas, this T_z, however, does not always corresponds to the other temperatures such as T_e or T_p, because of the low density and the lack of time to achieve equilibration. Time evolution of the number fraction of ionization state i obeys a rate equation

$$\frac{1}{n_\mathrm{e}}\frac{dF_i}{dt} = \alpha_{i-1}(T)F_{i-1} - [\alpha_i(T) + R_{i-1}(T)]\,F_i + R_i(T)F_{i+1}, \tag{2.47}$$

where $\alpha_i(T)$ and $R_i(T)$ are the ionization rate and recombination rate for a given temperature T. While a collisional ionization equilibrium (CIE) plasma has achieved $dF_i/dt = 0$, the non-equilibrium ionization (NIE) plasma has not. As can be seen from the left-hand side of equation (2.47), the ionization structure (i.e., distribution of F_i) is determined by the quantities $n_\mathrm{e}t$, which is sometimes called "ionization age". The reason why it appears only n_e (but not on n_i) is because the ionization proceeds mostly due to bombardment by the electrons. Numerically, a plasma is still under-ionized if $n_\mathrm{e}t \leq 10^{11}$ s cm^{-3}, while relatively close to an ionization equilibrium if $n_\mathrm{e}t \geq 10^{12}$ s cm^{-3}. Assuming $n_\mathrm{e} \sim 4$cm^{-3}, the threshold of $n_\mathrm{e}t \sim 3 \times 10^{11}$ s cm^{-3} is translated to a physical age of $\sim$ 2.5 kyr. As already mentioned, we do not have the way to measure ions temperatures directly with an X-ray observation yet, simple estimations for ion temperatures are considered by using the relation of $n_\mathrm{e}t$ and electron temperature T_e, for

example a proton temperature is estimated by

$$kT_p = 2.4 \times 11^{11} \left(\frac{n_e t}{\mathrm{cm}^{-3}\ \mathrm{s}} \right)^{-1} \left(\frac{kT_e}{keV} \right) \ \mathrm{keV}. \tag{2.48}$$

Figure 2.15 shows examples of spectra from NEI plasma with same temperature and different $n_e t$. We can see that $n_e t$ gets to be larger, the line intensities of H-like ions becomes stronger and features of recombination continua stand out more.

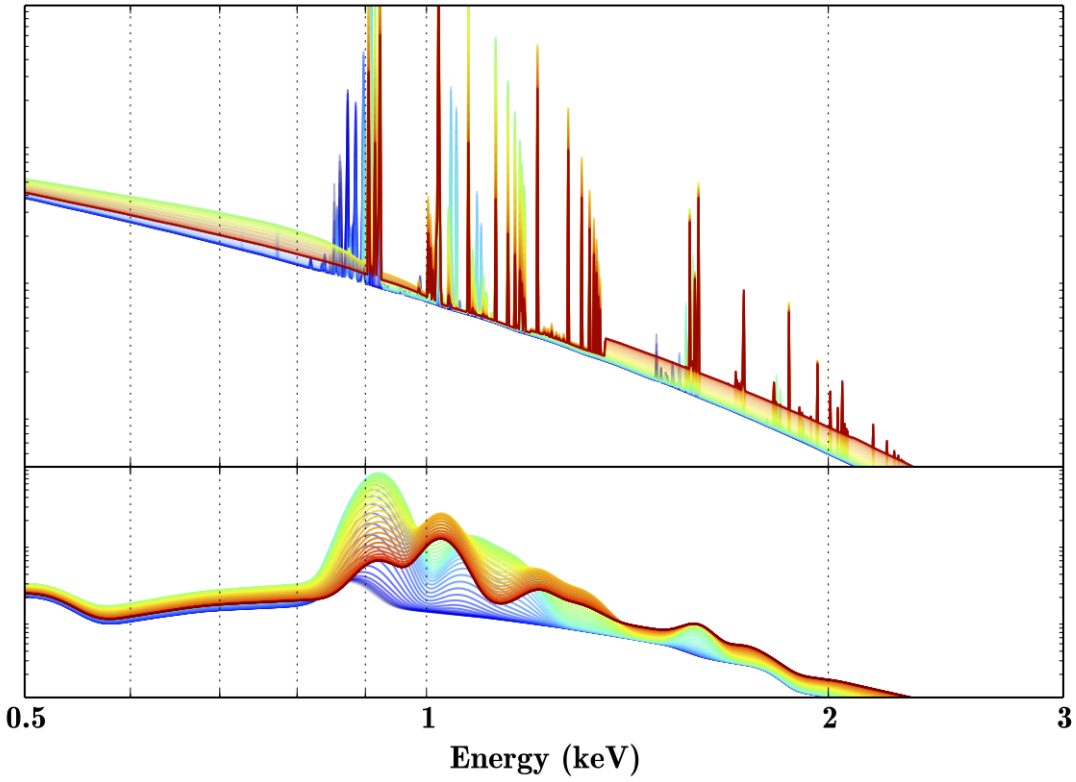

Figure 2.15: Examples of model X-ray spectra of NEI plasmas with different ionization age, made employing `NEI` code in `XSPEC`. The ionization age is changed from strongly non-equilibrium (blue, 10^8 s cm^{-3}) to full equilibrium (red, 5×10^{12} s cm^{-3}). The temperatures are fixed as 0.6 keV , and plotted by changing color from blue to red. To emphasize the relation in figure 2.14, only H and Ne are included. The Ne abundance is assumed to be solar, while those of other elements (heavier than He) are set to zero.

Chapter 3

Review of Neutron Stars

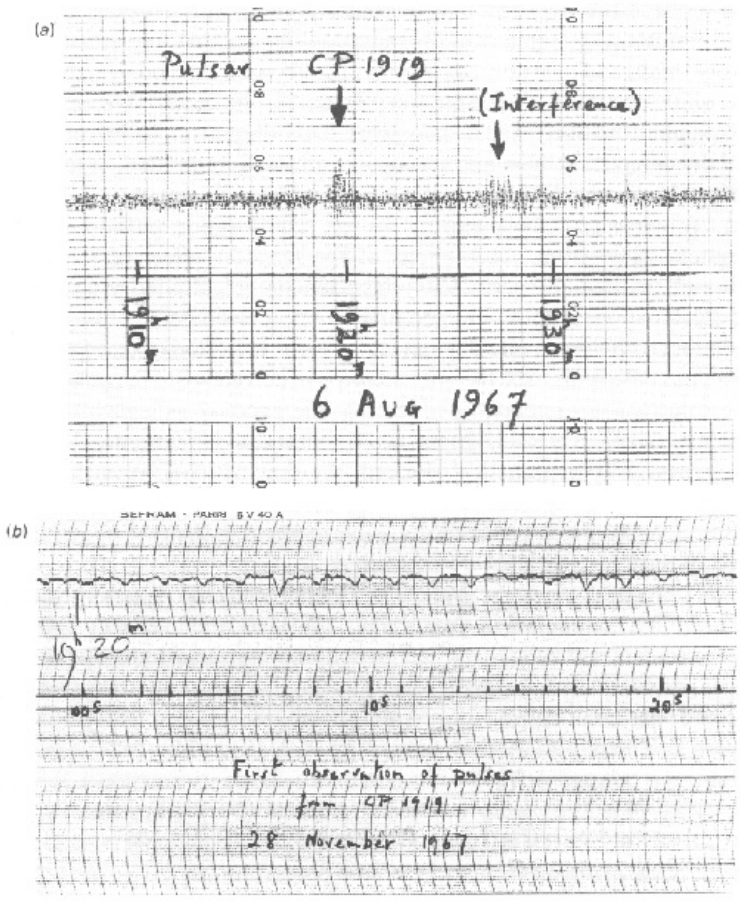

Figure 3.1: The first chart record of PSR B1919+21 (Hewish et al., 1968).

Since the first radio pulsar PSR B1919+21 was discovered in 1967 by Jocelyn Bell and Antony Hewish, neutron stars (NS) have been attracting researchers because of their extreme physical conditions such as rapid rotation, high densities and strong magnetic fields. They are born by core-collapse supernova (CC-SN) explosions which occur at the end of the evolution of massive stars as they run short of the nuclear fuel. The central region of the exploding

star collapses into an extremely dense and small object, namely an NS, which has a radius about 12 km and a mass $\sim 1.4\ M_\odot$, and is sustained by the balance between gravitational force and the degeneracy pressure of neutrons. The conservation of angular momenta and magnetic fluxes give them rapid rotation (down to a period of 1.4 ms) and strong magnetic fields (up to $\sim 10^{15}$ G or even higher), respectively. Today, they are observed in various forms in various electromagnetic frequencies, most typically as regularly pulsating objects as pulsars.

3.1 Overview of Neutron Stars

Recent advancement of observational techniques has been revealing the various characteristics and diverse species of NSs beyond our imagination. The classification of NSs may be carried out according to their environment (isolate or binary), the primary power sources for their emission (rotation energy, magnetic filed energy or gravitational energy of accreting matters), or wavelength in which they are mainly emitting (radio, X-ray, γ-ray or the other lengths). Furthermore, one of the fundamental quantities lying under the classification is the strengths of their magnetic fields.

Figure 3.2, called $P - \dot{P}$ *diagram*, serves as an important tools of the NS classification. The pulse period P and its derivative $\dot{P}$ plotted in figure 3.2 provide various pieces of fundamental information on NSs in the following way. As shown in the left-bottom side of figure 3.2, the spin periods of the fast spinning pulsars reach 1.4 ms; for example, PSR J1748-2446 is rotating with a period of $P = 1.396$ ms (Hessels et al., 2006). Such fast rotations can strongly constrain the average density of NSs, classical equality between the gravitational force and centrifugal force at the NS equator as $\rho_{\rm NS} > (3/4\pi)\ \omega_{\rm NS}^2/G \sim 10^{14}$ g cm^{-3}, where $\omega_{\rm NS} = 2\pi/P$ is the angular frequency, and G is gravitational constant. This $\rho_{\rm NS}$ is close to the density of the nuclear matter, 2.3×10^{14} g cm^{-3}, and is much higher than that of a white dwarf. Therefore, such short-period pulsars are not explained as white dwarfs, and provide compelling evidence that they are sustained against the strong gravity by the degeneracy force of neutrons.

The maximum number $N_{\rm max}$ of the neutrons that can be included in such a degenerate star is determined by the balance between the gravitational energy and Fermi energy as

$$N_{\rm max} \sim \left(\frac{\hbar c}{G m_{\rm n}^2}\right)^{3/2} \sim 2 \times 10^{57}\ , \tag{3.1}$$

where the dimensionless quantity $G m_{\rm n}^2/\hbar c \simeq 5.9 \times 10^{-39}$, called *gravitational fine-structure constant*, represents the strength (or "weakness") of gravity. Then, the maximum mass of an NS is described as $M_{\rm NS} = N_{\rm max} m_{\rm n} \sim 1.5\ M_\odot$. The total energy per neutron is given as

$$\varepsilon_{\rm n} = \frac{3}{10 M_{\rm NS}} \left(\frac{9\pi\hbar^3 N_{\rm max}}{4}\right)^{2/3} R^{-2} - \frac{3 G N_{\rm NS} M_{\rm NS}^2}{5} R^{-1}\ , \tag{3.2}$$

where the first and second term represents to the Fermi energy and the gravitational energy per neutron, respectively. Since the two terms in equation 3.2 have different dependence on R, the

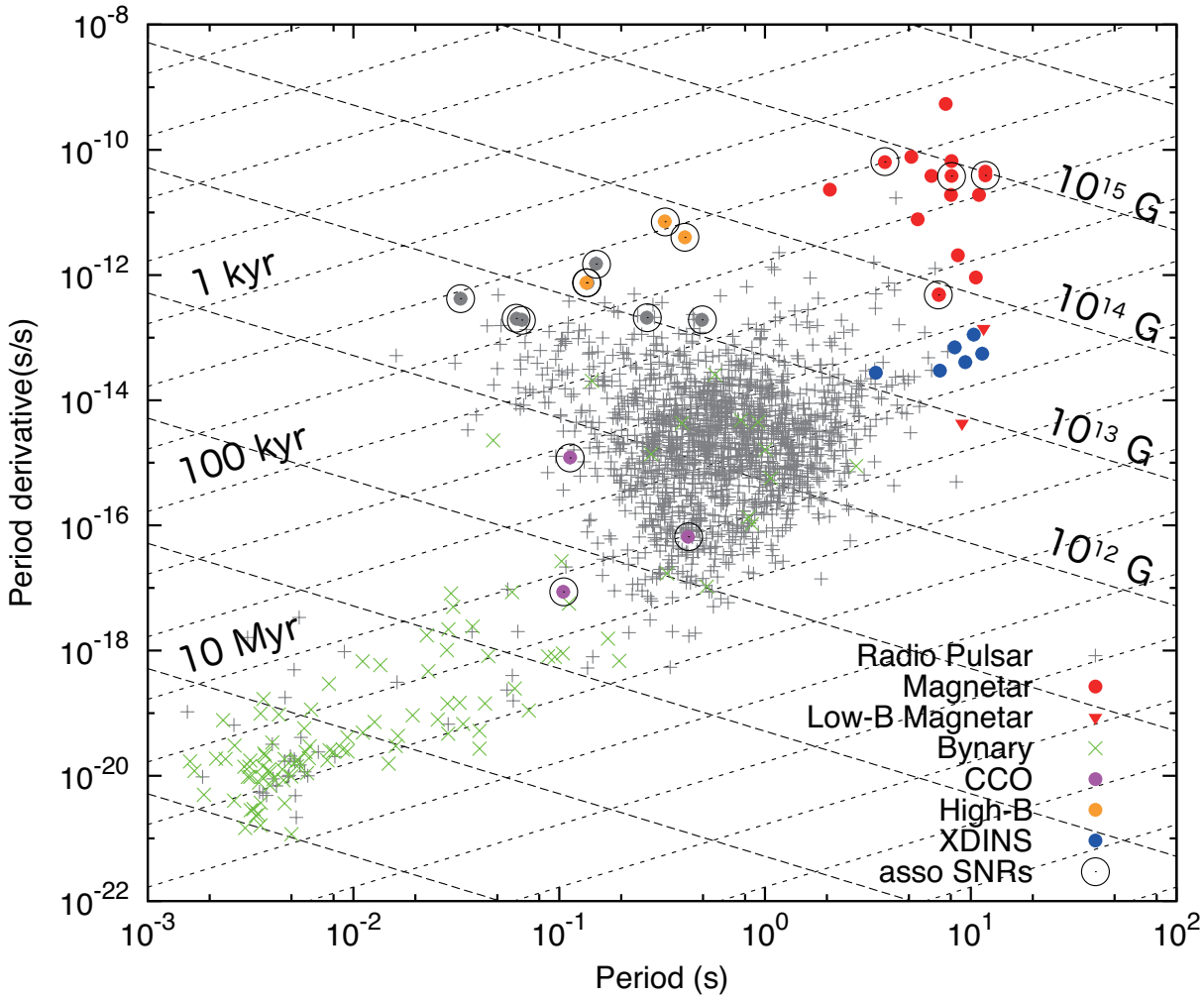

Figure 3.2: A P-$\dot{P}$ diagram plotted based on the *ATNF pulsar catalogue* (Hobbs et al., 2004). Gray and orange indicate radio pulsars and High-B pulsars, respectively. Red and blue are magnetars and XDINSs, respectively. The ones associated with SNRs are encircled, and those found in binary systems are represented by green. Dashed grid lines (rising to the left) specify the characteristic age ($= P/2\dot{P}$), while dotted ones (rising to the right) the dipole magnetic field ($\propto \sqrt{P\dot{P}}$).

radius of an NS can be calculated thorough minimization of $\varepsilon_{\rm n}$ as

$$\frac{d\varepsilon_{\rm n}}{dR} = 0 \Rightarrow R_{\rm NS} = \frac{\hbar^2 (9\pi/4)^{2/3}}{G M_{\rm NS}^3 N_{\rm max}^{1/3}} \sim 12 \text{ km} . \tag{3.3}$$

Since we have thus rough estimates of the mass and radius of the NS, we can calculate the gravitational energy released by the formation of an NS as

$$E_{\rm G} \sim -\frac{G M_{\rm NS}^2}{R_{\rm NS}} \sim 10^{53} \text{ erg} . \tag{3.4}$$

In reality, only a few percent of this $E_{\rm G}$ is thought to be transformed into kinetic energy which drives a supernova remnant (§2.1.1). As already mentioned, we can estimate a plausible initial angular frequency of a newborn NS by the angular momentum conservation as

$$\boldsymbol{I}_{\rm ST}\boldsymbol{\omega}_{\rm ST} = \boldsymbol{I}_{\rm ST}\boldsymbol{\omega}_{\rm ST} + \boldsymbol{L}_{\rm ej} \;\Rightarrow\; \omega_{\rm NS} \sim \frac{I_{\rm ST}}{I_{\rm NS}}\omega_{\rm ST} = \frac{M_{\rm ST}R_{\rm ST}^2}{M_{\rm NS}R_{\rm NS}^2}\omega_{\rm ST},$$

where $\boldsymbol{I}_{\rm ST}$ and $\boldsymbol{I}_{\rm NS}$ means the moments of inertia of the progenitor and the NS, respectively, $M_{\rm ST}$ and $M_{\rm NS}$ their masses, and $R_{\rm ST}$ and $R_{\rm NS}$ their radii. We note that $M_{\rm ST}$ does not mean the initial mass of the star but that of the end point (i.e., the progenitor mass just before the SN explosion), because such massive stars lose their masses by their strong stellar winds. For simplicity, if we assume that a progenitor with an explosion mass of $M_{\rm ST} = 1.4\ M_\odot (\sim 2.8 \times 10^{33}$ kg), a radius of $R = R_\odot (\sim 7.0 \times 10^5$ km) and $\omega_{\rm ST} = 2\pi/2$ month $\sim 1.15 \times 10^{-6}$ rad s^{-1} makes an SN explosion and leaves an NS with $M_{\rm ST} = M_{\rm NS}$ and $R_{\rm NS} = 12$ km, the initial rotation period of the NS becomes $P_0 = 1.5$ ms. This estimate of course is too simple, and the distribution of the initial rotation of NSs is still an open issue (e.g., Igoshev & Popov 2013).

In an analogy to the above estimation, if the magnetic flux conservation holds during the collapse, the magnetic filed strength also increases in proportion to the $(R_{\rm ST}/R_{\rm NS})^2$ ratio. Then the initial magnetic filed of the NS potentially attains $\sim 10^{12}$ G from the 10^2 G which is a typical global filed strength of the Sun. Also, a neutron has an intrinsic angular momentum and thus an intrinsic magnetic moment of $\mu_{\rm n} = -1.91 \times (e\hbar/2m_{\rm p}c)$. Then, if we assume that only $\sim 10^{-4}$ of the overall neutrons in an NS are spin-aligned to form a ferromagnetic phase (Makishima et al., 1999), the global magnetic field is expected to become

$$B_{\rm NS} = \frac{\mu_0}{2\pi R_{\rm NS}^3} \times \frac{N_{\rm max}}{100}\mu_{\rm n} = \frac{2\mu_0}{3}\frac{N_{\rm max}}{V_{\rm NS}}\frac{\mu_{\rm n}}{100} \sim 2 \times 10^{12} \text{ G} . \tag{3.5}$$

Owing to the extremely high density, such an exotic mechanism may not be impossible inside NSs.

3.2 Rotation-Powered Pulsars

Soon after the discovery of the radio pulsars, their explanation in terms of rotating magnetized NS were rapidly developed (e.g., Goldreich & Julian 1969; Ostriker & Gunn 1969). This model assumes that the rotation of an NS is gradually slowing down with time by the strong *magnetic braking*.

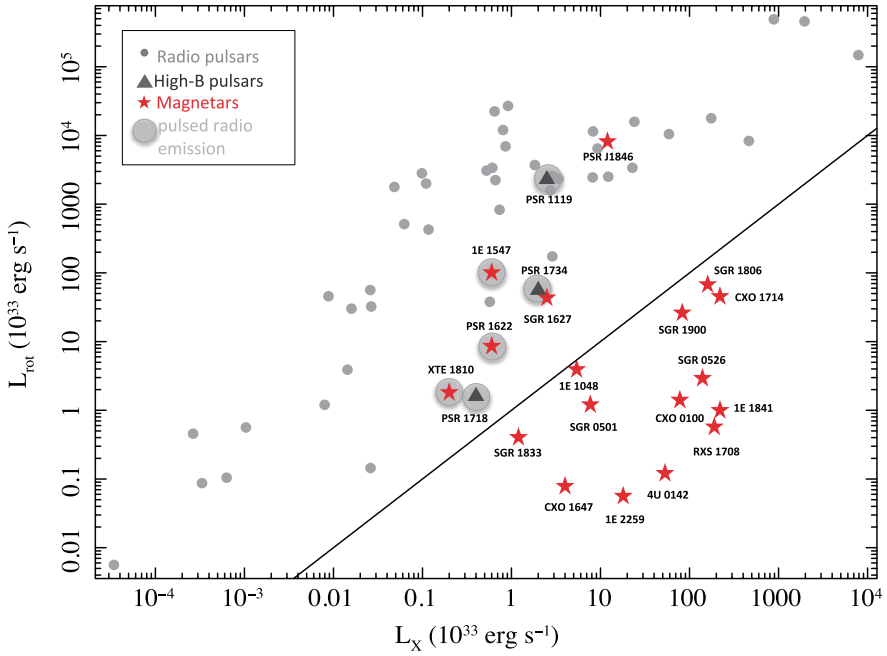

Figure 3.3: The relations between the spin-down luminosity ($L_{\rm rot}$) and the 2-10 keV X-ray luminosity ($L_{\rm X}$) of NSs, taken from Rea et al. (2012). The solid line shows the equal-luminosity condition.

3.2.1 Rotational energy and spin-down luminosity

As shown in figure 3.2, all pulsars are spinning down. In that course, an NS is expected to lose its rotational energy as

$$\begin{aligned} \dot{E} &= \frac{d}{dt}\left(\frac{1}{2}I\omega^2\right) = I\omega\dot{\omega} = -4\pi^2 I\frac{\dot{P}}{P^3} \\ \Rightarrow \quad -\dot{E} &= 3.6\times10^{35}\left(\frac{\dot{P}}{10^{-11}\ \mathrm{ss}^{-1}}\right)\left(\frac{P}{1\ \mathrm{s}}\right)\ \mathrm{erg\ s}^{-1}\ . \end{aligned} \tag{3.6}$$

This -$\dot{E}$ is often called *spin-down luminosity*. The lines representing equal $\left|\dot{E}\right|$ are drawn with the index 3 ($\dot{P} \propto P^3$) in the P-$\dot{P}$ diagram (figure 3.2). The rotational energies are thought to be the primary power source of the most of known pulsars. This view is supported by figure 3.3. The data points of radio pulsars are distributed above the line indicating equal-luminosity, which means that the observed luminosities can be explained by their spin-down luminosities.

Therefore, they are classified into *rotation-powered pulsars*, which are NSs powered by their rotation energy as equation 3.6. Most of the known NSs are observed as radio pulsars, and they are considered as typical rotation-powered pulsars.

3.2.2 Magnetic dipole radiation

Let us next consider how $-\dot{E}$ is converted into radiation. An NS with a dipole magnetic field B is expected to emit magnetic dipole radiation of a luminosity of

$$L_{\rm s} = \frac{\left(BR^3\right)^2}{6\pi c^3 \mu_0}\omega^4 \propto B^2 P^{-4} \,, \tag{3.7}$$

where c and μ_0 are light velocity and permeability respectively, and $P = 2\pi/\omega$ is the rotation period. Then, it is assumed that a pulsar emits this $L_{\rm s}$ spending its rotational energy, namely, $L_{\rm s} = -\dot{E}$. Then, by equating equation 3.7 and equation 3.6, the dipole field is obtained as

$$B_{\rm d} = \sqrt{\frac{2Ic^3 P\dot{P}}{2\pi^2 R^6}} \sim 2.0\times10^{12}\ {\rm G}\left(\frac{P}{1{\rm s}}\right)^{1/2}\left(\frac{\dot{P}}{10^{-15}{\rm ss}^{-1}}\right)^{1/2} . \tag{3.8}$$

Furthermore, independent and more direct measurements of the magnetic fields with cyclotron resonance features in X-ray spectrum spectra indicates that accreting X-ray pulsars mostly have $B \sim 10^{12}$ G (e.g., Makishima et al. 1999), which supports the same view of the distribution of B from the rotating NS model as shown in figure 3.2.

From this, the energy stored by the dipole magnetic fields is roughly estimated as

$$E_B \sim \frac{B^2}{8\pi}R^3 = 4\times10^{42}\left(\frac{B_{\rm d}}{10^{15}\ {\rm G}}\right)^2\left(\frac{R}{10\ {\rm km}}\right)^3\ {\rm erg}\,. \tag{3.9}$$

We can generalize equation 3.6 as

$$\dot{\omega} = -\mathcal{L}_n\omega^n \tag{3.10}$$

where L_n is a constant of proportionality of either sign, while n is a constant called *braking index* or *spin-down index*, and is thought to reflect the physical processes of the spin down. For example, $n = 2$ corresponds to the accretion braking (Alpar et al., 2011) as

$$\dot{\omega} \propto \dot{M}\omega^2, \tag{3.11}$$

$n = 3$ to the magnetic dipole radiation as already mentioned, and $n = 5$ to the gravitational wave radiation as

$$\dot{\omega} = -\frac{32}{5}\frac{G}{c^2}I\epsilon\omega^5 \tag{3.12}$$

where ϵ is the ellipticity of the NS (Palomba, 2000).

3.2.3 Spin down evolution

Assuming that $\mathcal{L}_n$ is constant, we can integrate equation 3.10. Solving it for the time t, and eliminating $\mathcal{L}_{\rm n}$ using equation 3.10 again, we obtain

$$t + t_0 = \frac{P}{(n-1)\,\dot{P}}\,, \tag{3.13}$$

where t_0 is an integral constant meaning that the pulsar would have been spinning with an infinite speed ($P = 0, \omega \to \infty$) at the time t_0 before its birth ($t = t_0$). Assuming that t_0 is small enough (i.e., the rotation was very fast even at $t = t_0$) , the *characteristic age* τ_c can be defined as

$$\tau_c \equiv \frac{P}{(n-1)\,\dot{P}} \,. \tag{3.14}$$

In a narrow sense of the characteristic age, the dipole radiation is assumed to play a main role of the spin down, so that $n = 3$ is generally used. Differentiating equation 3.10, n can be solved as

$$n = \frac{\ddot{\omega}\omega}{\dot{\omega}^2} \,. \tag{3.15}$$

which is represented by observable parameters. Hence measuring $\ddot{\omega}$ ($\ddot{P}$) allow us to determine n of an NS.

Through radio observations, more than 2000 rotation-powered pulsars have been catalogued so far (Manchester et al., 2005), About a hundred of them are detected at X-ray or γ-ray energies. As shown in figure 3.3, the X-ray luminosities are a few % of the spin down luminosities. Totally, $\sim$ 10 % of the spin down power $\dot{E}$ is thought to be released by pulsed electromagnetic radiation. Even though many rotation-powered pulsars are observed in radio wavelength the radio pulsed emission occupy only 10^{-4} of the spin down powers, and most of $-\dot{E}$ is carried by γ-rays around a GeV, except a few cases,

Most of the observed values of n are close to $n = 3$ or slightly smaller. Therefore the dipole radiation model well describes the nature. For example, the birth of the Crab pulsar can be used for the examination of the model. Using observed values of $P = 0.033$ s and $\dot{P} = 4.23 \times 10^{-13}$ ss^{-1} (Lyne et al., 1993), the characteristic age of the crab pulsar is calculated as $\tau_c = 1240$ yr, which is a good estimation for its actual age of $t = 960$ yr (2014 present).

Although it was believed till 1990's that the magnetic field decays with time, a doubt was cast on such a view by Makishima et al. (1999). In fact, recent population studies of radio pulsars indicate that the timescales of the magnetic field decay are longer that the pulsar life time (Regimbau & de Freitas Pacheco, 2001). Then, their magnetic fields can be dealt as constant values.

3.3 Magnetar

Magnetars are a growing subclass of NSs which are generally believed to have extremely strong magnetic fields of 10^{14-15} G. Figure 3.4 shows their discovery history (Olausen & Kaspi, 2014). The number has been increasing rapidly, especially after the late 2000s, reaching 28 (including candidates), as of 2014 December. These are observed as two different classes, as Anomalous X-ray Pulsars (AXPs) and Soft Gamma Repeaters (SGRs). Until the *magnetar hypothesis* was proposed (Duncan & Thompson, 1992; Thompson & Duncan, 1995), they had been composing puzzling NSs species, because their observational characteristic cannot be explained either by the canonical rotating NS model nor by mass accretion. Today, they are both thought to be

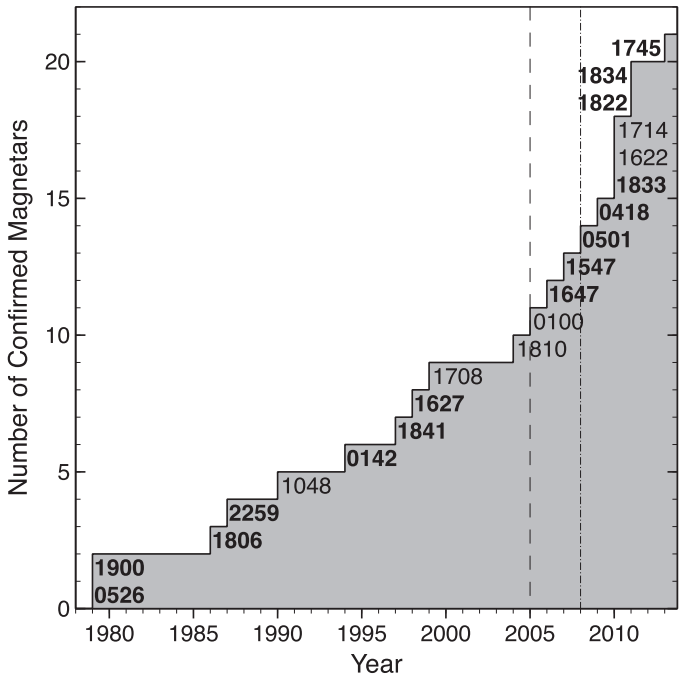

Figure 3.4: The accumulated number of confirmed magnetars, taken from (Olausen & Kaspi, 2014).

representative objects of magnetically-powered NSs, collectively called magnetars, and there is essentially no difference between AXP and SGR. A more detailed history of one particular AXP, namely 1E 2259+586, is reviewed in §5.1, in relation to its host SNR CTB 109. Remarkable properties of magnetars are reviewed below.

Burst activity

In hard X-ray and γ-ray band, they sometimes produce repeated bursts with a duration of several tenths of second. In these bursts, huge energies, $\sim 10^{40}$-10^{41} erg, are released in hard X-ray and

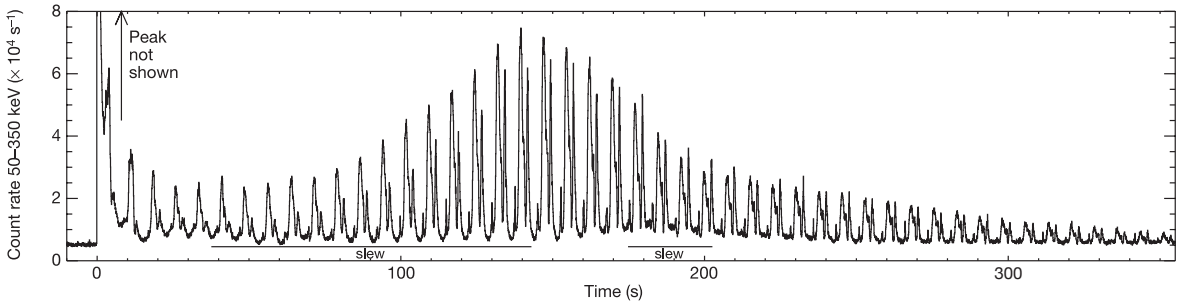

Figure 3.5: The light curve of the giant flare of SGR 1806-20, taken from Hurley et al. (1999)

soft γ-ray bands. Some SGRs showed more energetic activities called *giant flares*, in which tremendous energies, $\sim 10^{45}$-10^{47} erg, were released (e.q., Cline et al. 1980 for SGR 0526-66; Hurley et al. 1999 for SGR1900+14; Palmer et al. 2005 for SGR 1806-20,). Figure 3.5 shows a giant flare of SGR1806+20 detected by the BAT on the *swift* observatory. The signal is strongly modulated at a period of 7.54 sec (Woods et al., 2007), which represents the rotation of the NS. Since such events become much more luminous than the Eddington-Luminosity, it is difficult to explain them by accretion. The number of detection of similar abrupt activity increases, namely, enhanced persistent X-ray flux and production of frequent short burst, have been observed from some AXPs (e.g., 1E 1547.0-5408 by Israel et al. 2010; 1E 2259+586 in §5; AX J1841.0-0536 by Romano et al. 2011). These activities are all considered to be powered by released energies from their strong magnetic fields, rather than via accretion of some materials around them.

Strong magnetic fields and small characteristic ages

On the P-$\dot{P}$ diagram of figure 3.2, magnetars are distributed in the upper right. Compared with radio pulsars, they are slower rotators but have larger $\dot{P}$, meaning that their rotation is braked by some stronger forces. Assuming that this braking force is provided by the emission of magnetic dipole radiation, their dipole magnetic fields are calculated by equation 3.5 in the same way as radio pulsars. Using the typical pulse property of magnetars as $P = 5$ s and $\dot{P} = 10^{11}$ ss^{-1}, the strength of their magnetic field is estimated to be $B_{\rm d} \sim 2.2 \times 10^{14}$ G, which exceeds the quantum limit of $B_{\rm qed} = 4.4 \times 10^{13}$ G. Here, $B_{\rm qed}$ is the energy where split of the Landau levels becomes equals to the electron rest mass, and is given as

$$\hbar \frac{eB_{\rm qed}}{m_{\rm e}c} = m_{\rm e}c^2 \Rightarrow B_{\rm qed} \equiv \frac{m_{\rm e}^2 c^3}{e\hbar}. \tag{3.16}$$

The characteristic age can also be calculated as $\tau_{\rm c} = P/2\dot{P} \sim 8000$ yr, which indicates that they are considerably younger objects compared with the other NS species so far known. While the pulse periods of radio pulsars are widely distributed, those of magnetars are concentrated in a narrow range of 2-12 s.

Enigmatic X-ray spectra

Generally, magnetars are visible only in X-ray and/or soft γ-ray wavelength, and few of them are detected in the other wavelengths such as optical or infrared. As shown in figure 3.6 (den Hartog et al., 2008), their X-ray spectra are mainly composed of two distinct components. The typical spectra below $\sim$ 10 keV are mostly dominated by a blackbody like component with a temperature of $\sim$ 0.5 keV, while the hard X-ray ($\gtrsim$ 10 keV) signals are carried by a very hard power-law like shaped component reaching $\sim$ 100 keV or higher. The nature of this enigmatic hard component, together with its relation to the soft component, remains a big puzzle. As shown in figure 3.3, X-ray luminosities of magnetars exceed their spin-down luminosities. For

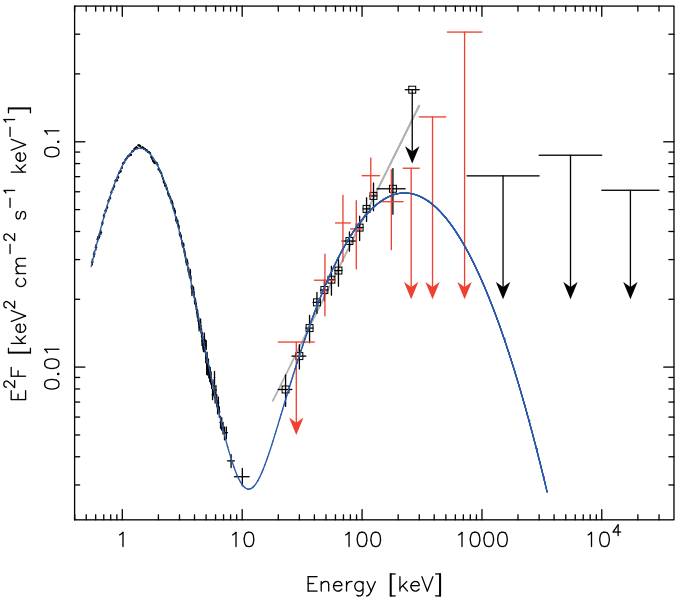

Figure 3.6: A wide-band spectrum of the typical AXP, 4U 0142+61, obtained by *Xmm-Newton* (<10 keV) and *Integral* (>20 keV). From den Hartog et al. (2008).

example, the 2-10 keV X-ray luminosity of 4U 0142+61, $\sim 1.0 \times 10^{36}$ erg s^{-1} (Israel et al., 1994), is much higher than the spin-down luminosity of $L_{\rm x} = 1.2 \times 10^{32}$ erg s^{-1} (Dib & Kaspi, 2014). Therefore, as already described, magnetars cannot be rotation-powered objects, and this fact supports their interpretation as magnetically-driven NSs. In fact, the rotation energy of this magnetar itself ($E_{\rm s} \sim 5 \times 10^{44}$ erg) of 4U 0142+61 is much smaller than that of a radio pulsars ($\sim 4 \times 10^{49}$ erg for the Crab pulsar), but the energy of $E_B \sim 10^{43-44}$ erg is stored in magnetic field. As the small characteristic ages of magnetars imply their magnetic activities do not last as long as the rotational life time of radio pulsars when they run short of their magnetic energies in $E_B/L_{\rm x} \sim 10 - 20$ kyr.

The hard X-ray component of a typical magnetar is represented by a power-law model with $\Gamma = 0 - 2$ (Enoto et al., 2010a), which cannot be explained easily by conventional non-thermal processes. This component is observed from both AXPs and SGRs, thus supporting that these two classes can be merged together. As illustrated by figure 3.7, extensive *Suzaku* observations revealed that the two-component spectral shape of magnetars is tightly correlated with the characteristic age (Enoto et al., 2010a), as

$$\frac{F_{\rm H}}{F_{\rm S}} = (3.3 \pm 0.3) \times \left(\frac{\tau_{\rm c}}{1{\rm kyr}} \right)^{-0.67 \pm 0.04} , \tag{3.17}$$

where $F_{\rm H}$ and $F_{\rm S}$ are the fluxes of the hard X-ray component and the soft component, respectively. Thus, the fraction of energy flux from the hard X-ray component decreases with time. Surprisingly, however, the hard component becomes harder with the increasing characteristic age, as seen in figure 3.7.

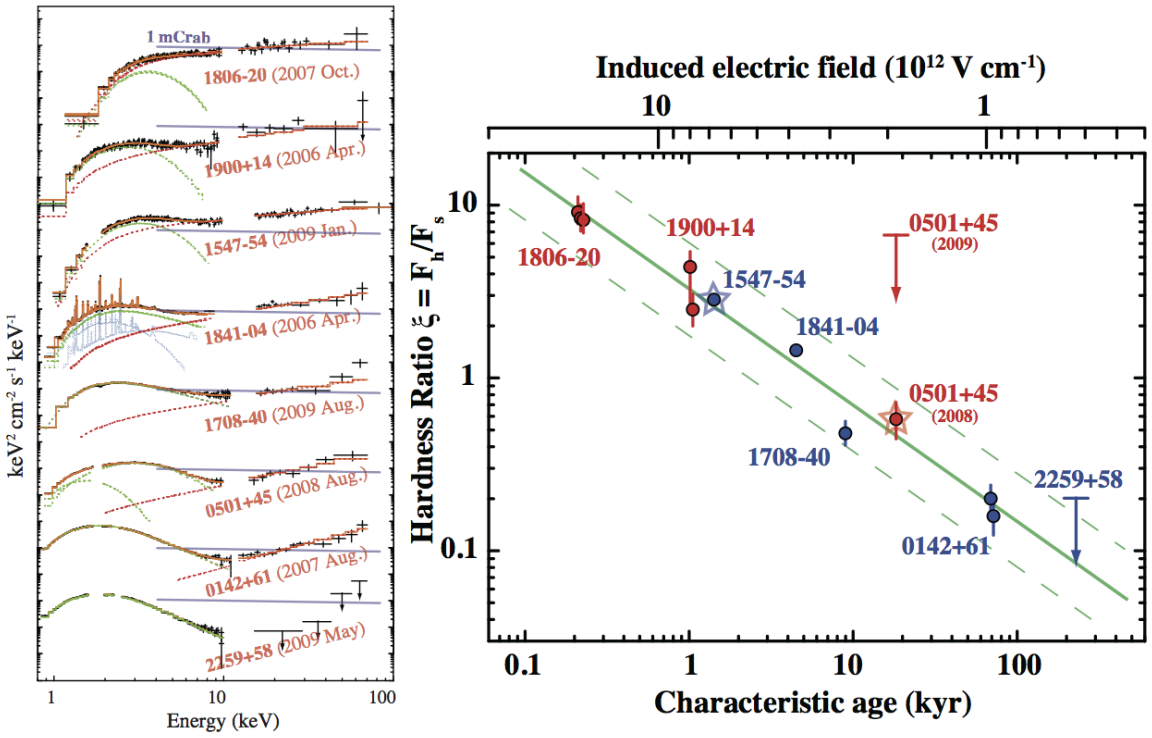

Figure 3.7: The spectral evolution of magnetars revealed with *Suzaku* (Enoto et al., 2010a). (a) Broad-band $\nu F\nu$ spectra of 8 magnetars, obtained with *Suzaku* and shown from younger (top) to older (bottom) objects. (b) The hardness ratio (see text) of *Suzaku* -observed magnetars, plotted against the characteristic age.

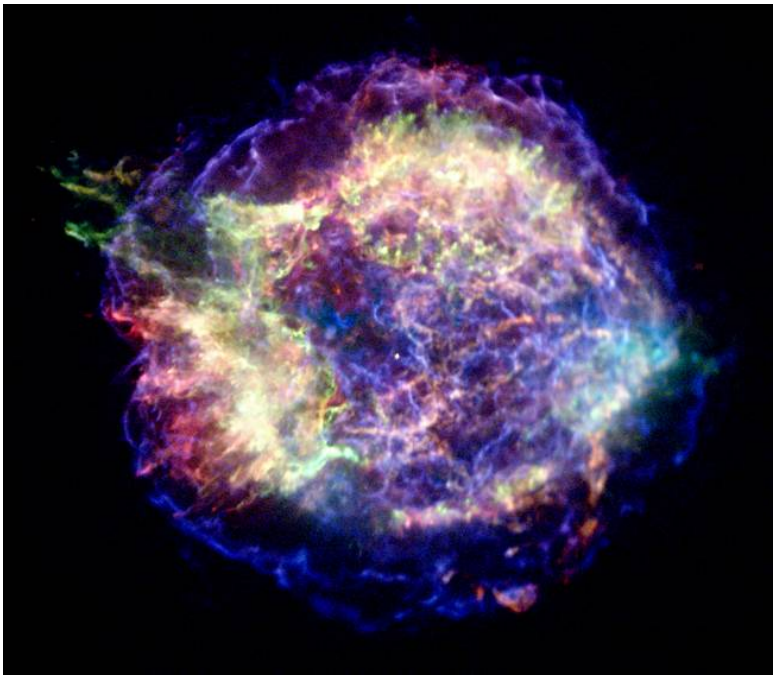

Figure 3.8: A false-color X-ray image of the SNR Cassiopeia A and its CCO CXOU J232327.9+584842 as an example of CCO/SNR associations; credited by NASA/CXC/SAO.

3.4 Central Compact Objects (CCOs)

It is widely believed that a core collapse SN explosion of a massive star leaves some kind of compact object, such as an NS or a black hole (or quark star; Ivanenko & Kurdgelaidze 1967). About two thousand NSs and three hundred SNRs are known in the Milky-way galaxy so far (Ferrand & Safi-Harb, 2012), but the number of NS/SNR associations appears to be much smaller than that expected from numbers of NSs and SNRs. and most of the SNRs are observed as empty harbors. Among these NSs, some ~ 40 are rotation-powered radio pulsars, with rotation periods of typically 30-100 msec. Other objects are magnetars described in §3.3. The rest are called *Central Compact Objects* (CCOs), which are neither active rotators nor magnetars. Since CCO are grown in number they are expected to provide the clue to the *empty problem*. Figure 3.8 is an X-ray image of the very young SNR Cassiopeia A and the associated CCO, CXOU J232327.9+584842.

Although eleven examples of CCOs are known up to the present, their natures still remain undetermined, and we do not even know whether all the CCOs. Thus, the definition of the CCO is slightly ambiguous. According to the narrower definition generally accepted, their common characteristics are that they are visible only in X-ray band, and show soft thermal spectra with temperature 0.2-0.4 keV and X-ray luminosities around 10^{33-34} erg s^{-1}. They are not accompanied by pulsar wind nebulae. These observational facts imply that CCOs are a kind of isolated cooling NSs with weak surface magnetic fields and located at the centers of the SNR. Recently, the temperature of the CCO in the SNR Cas A has been measured to be decreasing by 4% in 10 years (Heinke & Ho, 2010), which is much faster than that expected by

the standard NS cooling model.

So far, X-ray pulsations have been detected from only three of the CCOs. Their spin-down luminosities ($L_x = 5.3 \times 10^{33}$ erg s^{-1}; J1852+0040; 1.9×10^{32} erg s^{-1} for J1082-4300 ; 6.6×10^{31} erg s^{-1} for 1E 1207.4-5209), which are smaller than their X-ray luminosities, means they are not powered by the rotational energies. However, they are not considered as magnetically-powered either, since their pulse properties indicate that they have quite weak dipole magnetic fields (Gotthelf et al., 2013; Halpern & Gotthelf, 2010), for example; CCO J0822.0-4300 harbored by Pup A has the magnetic field with only $B = 2.0 \times 10^{10}$ G, 1E 1207.4-5209 in G296.5+10.0 with $B = 9.8 \times 10^{10}$ G (Halpern & Gotthelf, 2011), and J1852+0040 in Kes 79 with $B = 3.1 \times 10^{10}$ G

The small values of $\dot{P}$ of the pulse-detected CCOs also imply very long characteristic ages, $P/2\dot{P} \sim$ a few hundreds Myrs. However, these must be largely overestimated, because their host SNRs should last only for 10-100 kyr (§2.1.1). Thus, CCOs can be considered as young, relatively inactive NSs with very low dipole fields, but somehow emitting at relatively high luminosities. Because of the weak magnetic fields and not being rotation-powered, they are sometimes thought to constitute *anti-magnetars* against to the magnetars.

Another interesting aspect of CCOs is the spectral feature plausibly arising from electron cyclotron absorption. The left and right panel of figure 3.9 are pulse shape and phase resolved X-ray spectra of the CCO 1E 1207.4-5209 (Bignami et al., 2003). The spectra show deep absorption features at 0.7, 1.4 and 2.1 keV, which are interpreted as harmonic cyclotron resonance absorptions. Assuming the absorptions due to electron resonances, a weak magnetic field strength $B = 8 \times 10^{10}$ G is indicated. Similarly, the absorption feature implying such a weakly magnetized NS was found in the spectra of another CCO RX J0822-4300 (Gotthelf & Halpern, 2009).

Then, how CCOs are powered ? One attractive hypothesis is that CCOs harbor rather intense internal (toroidal) magnetic fields, even though their global dipole fields are very weak. If so, their X-ray emission could be driven by dissipation of this (internal) magnetic energy, just like in magnetars. In this case, the absorption features, like those in figure 3.9, might be proton cyclotron resonance, in extremely strong ($\sim 10^{15}$ G) multiple fields localized on the NS surface.

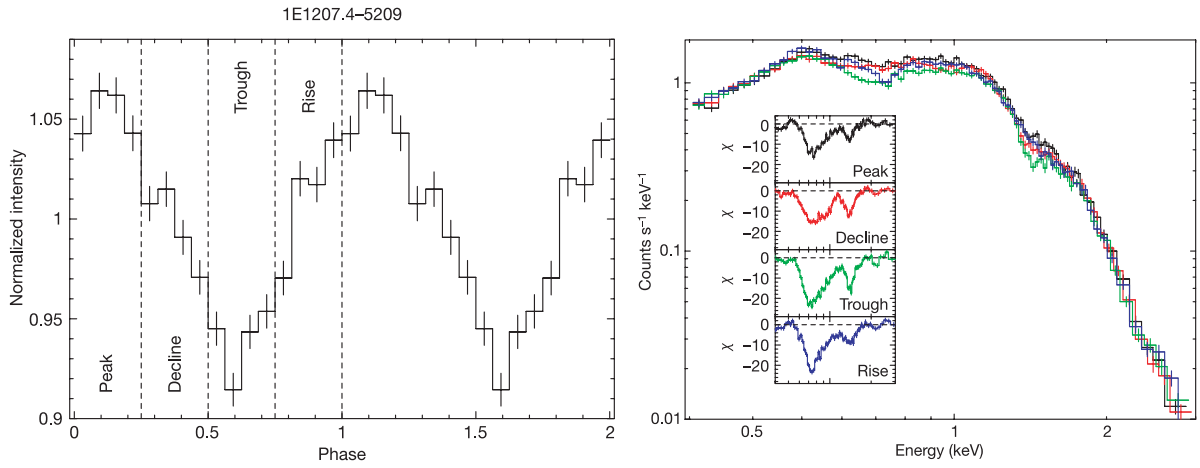

Figure 3.9: The pulse shape and phase resolved spectra of 1E 1207.4-5209, taken from Bignami et al. (2003).

3.4.1 X-ray Dim Isolated Neutron Star (XDINS, The Magnificent Seven)

Another subclass of NSs, composed of seven dim X-ray sources, is called X-ray Dim Isolated NS (XDINS). Discovered by *ROSAT*, they are thought to be nearby ($\leq$ 1 kpc) objects, and a kind of isolated cooling NSs, since their emission essentially has soft thermal X-ray spectra with a temperature of $\sim$ few hundred keV (e.g., Haberl 2005) and a radius of $\sim$ 10 km. They lack radio emission.

While these spectral features are similar to those of CCOs, XDINSs are associated with neither SNRs nor pulsar wind nebulae. Also the pulse properties are different between these two subclasses. Both P and $\dot{P}$ of the XDINS are larger than those of the pulse-detected CCOs: as seen in figure 3.2, XDINS are distributed near the magnetars rather than the pulse-detected CCOs in the P-$\dot{P}$ diagram. Hence, strong surface magnetic fields ($\sim 10^{13}$ G) are expected from their P and $\dot{P}$. For example, RX J1308.6+212708 has a strong magnetic field of $B = 3.4{\times}10^{13}$ G (Schwope et al., 2005) which is close to the quantum limit of 4.4×10^{13} G.

The spectra of RX J1308.6+212708 obtained by *XMM-Newton* show deviations from a blackbody model, which can be fitted with absorbed blackbody model (Haberl et al., 2003) as shown in 3.10. One of plausible interpretations is that it is proton cyclotron absorption corresponding to $B = (2 - 6) \times 10^{13}$ G. These seven XDINSs are sometimes called *the Magnificent Seven*, which is named after the *Kurosawa movie* (remade in US). Like other non-rotation-powered NSs, their spin-down luminosities around 4×10^{30} erg s^{-1} cannot sustain their X-ray luminosities $\sim$ 10^{30}-10^{32} erg s^{-1}. Hence, they are also thought to have another power sources within their bodies, such as thermal or electromagnetic.

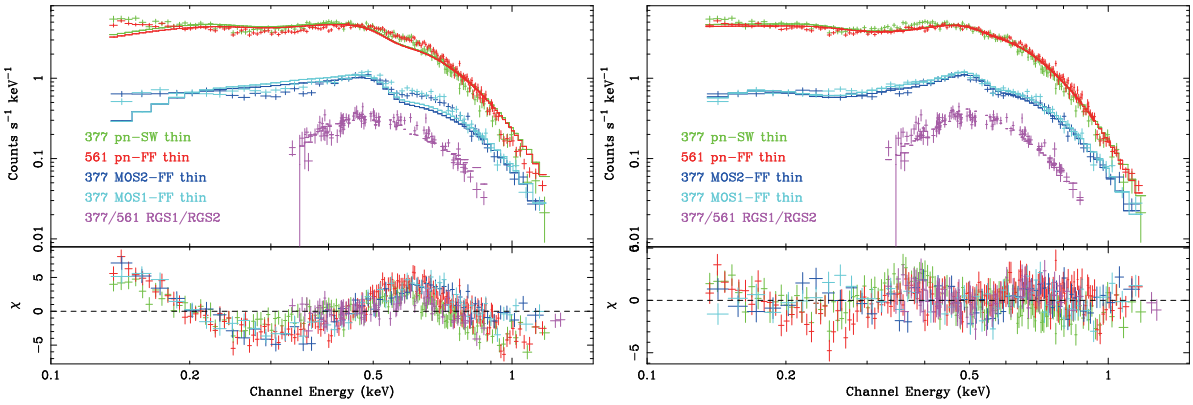

Figure 3.10: The *Xmm-Newton* spectra of RX J1308.6+212708 taken from Haberl et al. (2003). While the left panel shows the spectra fitted with a pure blackbody model, the right panel incorporates a Gaussian absorption line at ~ 0.3 keV.

Chapter 4

The *Suzaku* Satellite

Suzaku (Mitsuda et al., 2007) is the fifth Japanese X-ray observatory, which was launched on July 10. 2005 by M-V rocket from Uchinoura Space Center in Japan. It was successfully put into a near-circular orbit at ~ 570 km altitude with an inclination angle of 31°. Figure 4.1 shows a schematic view of *Suzaku* and its orbit. Four scientific instruments were installed on *Suzaku* , namely the X-ray Telescope (XRT; Serlemitsos et al. 2007), the X-ray Imaging Spectrometer (XIS; Koyama et al. 2007), the Hard X-ray Detector (HXD; Takahashi et al. 2007), and X-ray micro spectrometer (XRS). Because of abrupt loss of liquid helium 1 month after the launch, the XRS had stopped working before actual observation started. Through this paper, we study supernova remnants with this observatory. The properties of these instruments are summarized in table 4.1

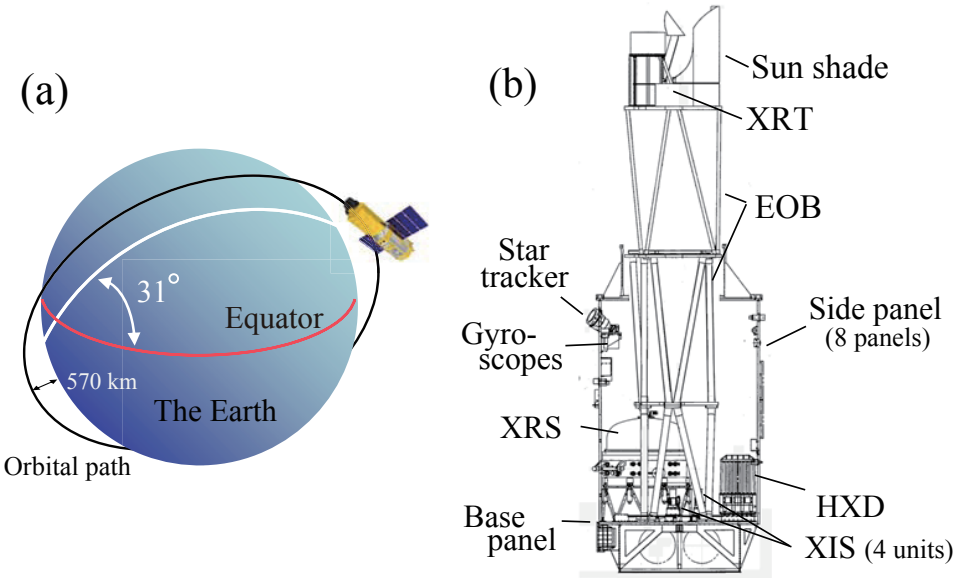

Figure 4.1: (a) A schematic inclination of the orbit of *Suzaku* . (b) A cross-section side view of *Suzaku* (Mitsuda et al., 2007).

Table 4.1: Properties of the instruments onboard *Suzaku* .

Instrument		
XRT	Focal Length	4.75 m
	Weight	19.3 kg
	Filed of View	20' at 1 keV
	Filed of View	14' at 7 keV
	Geometrical Area	873 cm^2
	Effective Area	450 cm^2 at 1.5 keV
	Effective Area	250 cm^2 at 7.0 keV
	Angular Resolution	2'.0 (Half Power Diameter)
XIS	Field of View	17'.8 × 17'.8
	Bandpass	0.2-12 keV
	Number of Pixels	1024 × 1024
	Pixels Size	24 μm × 24 μm
	Energy Resolution	~ 2 % at 6 keV
	Effective Area	340 cm^2 (FI), 390 cm^2 (BI) at 1.5 keV
		150 cm^2 (FI), 100 cm^2 (BI) at 8 keV
	Time Resolution	8 s (Normal mode), 7.8 ms (P-Sum mode)
HXD	Field of View	4°.5 × 4°.5
		34' × 34'
	Bandpass	10-600 keV
		(PN) 10-70 keV
		GSO) 40-600 keV
	Energy Resolution	(PIN) ~ 4 keV (FWHM)
		(GSO) ~ 7.6/ $\sqrt{E_M eV}$ % (FWHM)
	Effective Area	~ 160 cm^2 at 20 keV
	Effective Area	~ 260 cm^2 at 100 keV
	Time Resolution	61 μs

Figure 4.2: A picture of an XRT module, taken from Serlemitsos et al. (2007).

4.0.2 The X-Ray Telescope (XRT)

Figure 4.2 is a picture of one XRT module. Five XRT modules are installed on *Suzaku* . One of them focuses X-rays on XRS, and the others are for four XIS cameras. Each of them works as Wolter type-I grazing-incidence reflective optics as shown in figure 4.3. Incident X-rays are focused on the focal plane by the combination of primary parabolic and secondary hyperbolic mirrors with conical approximation. In order to obtain large effective area, each mirror is composed of a large number of nested thin-foils reflectors. The pre-collimators are placed in front of each module in order to suppress the stray lights from bright sources near the observation target,

Major characteristics of the XRT are given in figure 4.4 (Serlemitsos et al., 2007). Figure 4.4 (a) shows total effective area of the XRT-XIS combination as a function of the incident X-ray energy. Compared with *Chandra* and *Xmm-Newton*, four XRT modules provide effective areas larger than *Chandra* and a comparable *Xmm-Newton* effective area respectively cover a wide energy range of 0.2-12 keV. As shown in figure 4.4 (b), the effective area is decreasing while increasing an off-axis angles, and this behavior is called *vignetting*. These effects are included in the response function of the XIS in the form of Ancillary Response Files (ARFs).

The ARFs are generated by `xissimarfgen` software (Ishisaki et al., 2007).

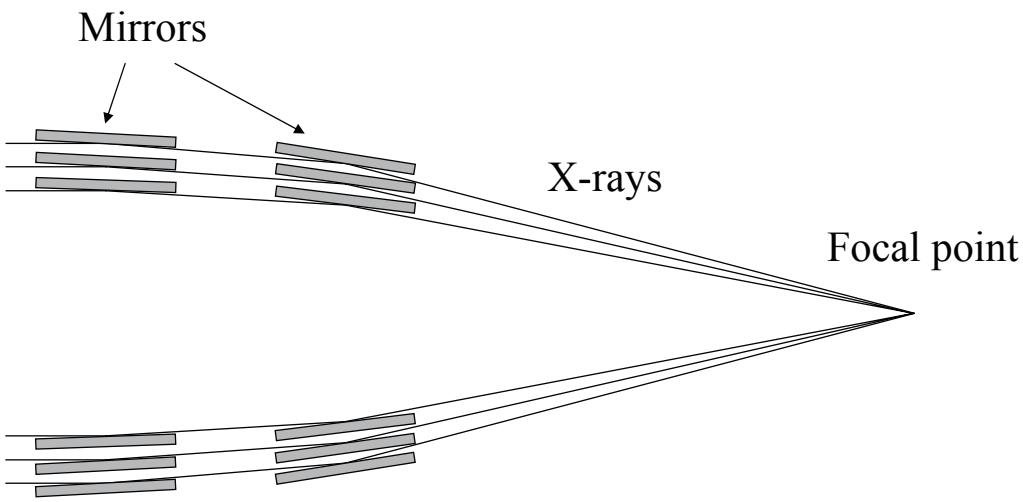

Figure 4.3: A schematic view of Wolter type-1 X-ray optics.

4.0.3 The X-ray Imaging Spectrometer (XIS)

Suzaku XIS consists of four X-ray sensors (XIS 0, 1, 2 and 3), or "cameras", each of which is placed at the focal plane of the corresponding XRT module. Each XIS sensor utilizes a silicon charged coupled device (CCD) chip, to measure the energy and 2-dimensional position of each single X-ray photon reflected by XRT. While three of them (XIS0,2, and 3) use front-illuminated (FI) CCDs, the other (XIS 1) utilizes a back-illuminated (BI) CCD. Figure 4.6 shows quantum efficiency of these two types of CCDs. Compared with the FI CCD, the BI CCD shows a higher efficiency in the lower energy range $\lesssim 4$ keV, but the opposite is the case for harder X-rays. As already listed in table 4.1, each CCD chip installed on the XIS sensor has a format of 1024×1024 pixels, divided into 4 segments (A, B, C and D) as shown in figure 4.7, and covers 17'.8 × 17'.8 area on the sky. Each XIS has ^{55}Fe calibration sources attached to the two corners of the CCD chip, as indicated in figure 4.7.

The XIS has some flexible operation modes. For example, the normal clocking mode provides the whole image of each CCD chip with a read out time of 8 seconds. For a bright source, the time resolution is sometimes not enough because multiple photon can arrive at a single pixel (called pile up), and hampers single-photon spectroscopy. Hence, XIS can be operated in other modes with higher time resolutions. In the 1/4 window-mode, 256×1024 pixels (1/4 area of CCD chip) are read out every 2 sec, and the 1/8 window-mode enables observations with time resolution 1 sec. Since November 2006, XIS 2 has not been working due to malfunction possibly caused by a debris hit. Thus, as of 2014 December, three XIS cameras (XIS 0, 1 and 3) are working.

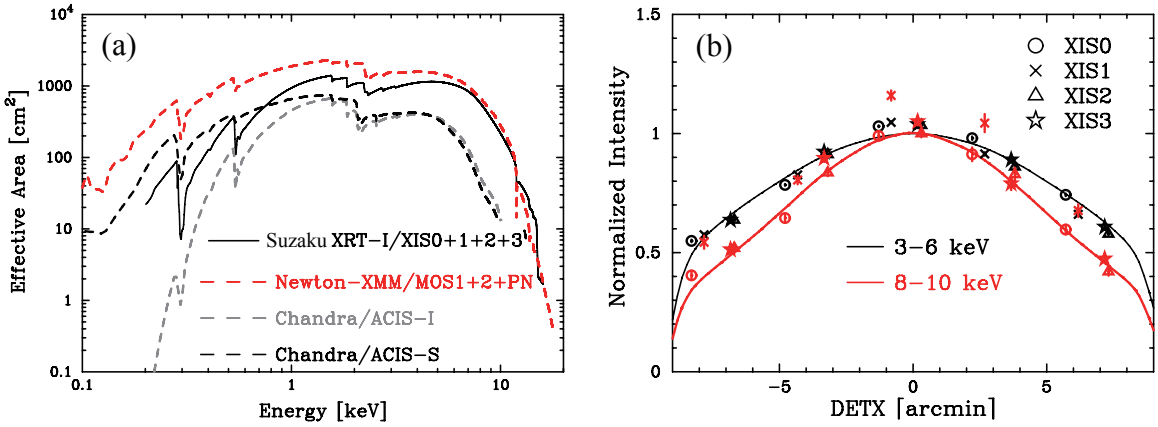

Figure 4.4: Characteristics of the X-ray optics of the XRT, taken from Serlemitsos et al. (2007). (a) The total effective areas of the four XRT modules compared with that of other X-ray observatories. These covered include both the reflectivity's of the optics and the quantum efficiency of the force plane detector (CCD). (b) Vignetting of the XRT. Data points are measurements from actual observation of the Crab Nebula as a standard candle, and curves are calculations from a ray-tracing simulator.

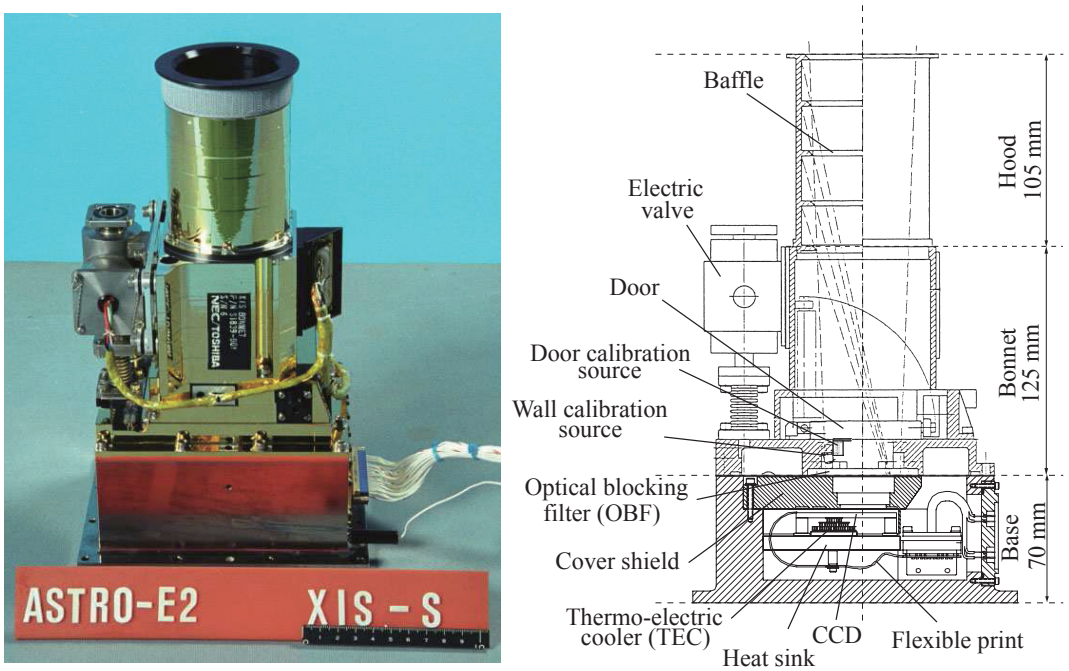

Figure 4.5: A picture (left) and a side view (right) of the *Suzaku* XIS (Koyama et al., 2007).

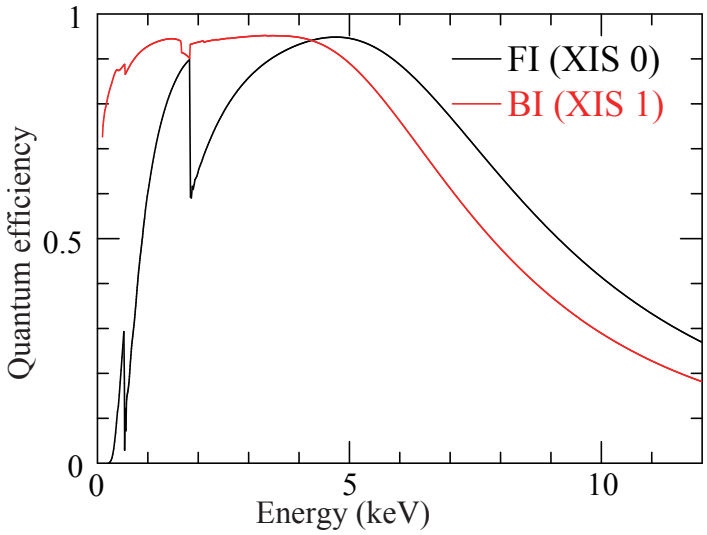

Figure 4.6: Quantum efficiency of the XIS CCDs. Black and red correspond to FI and BI CCDs, respectively.

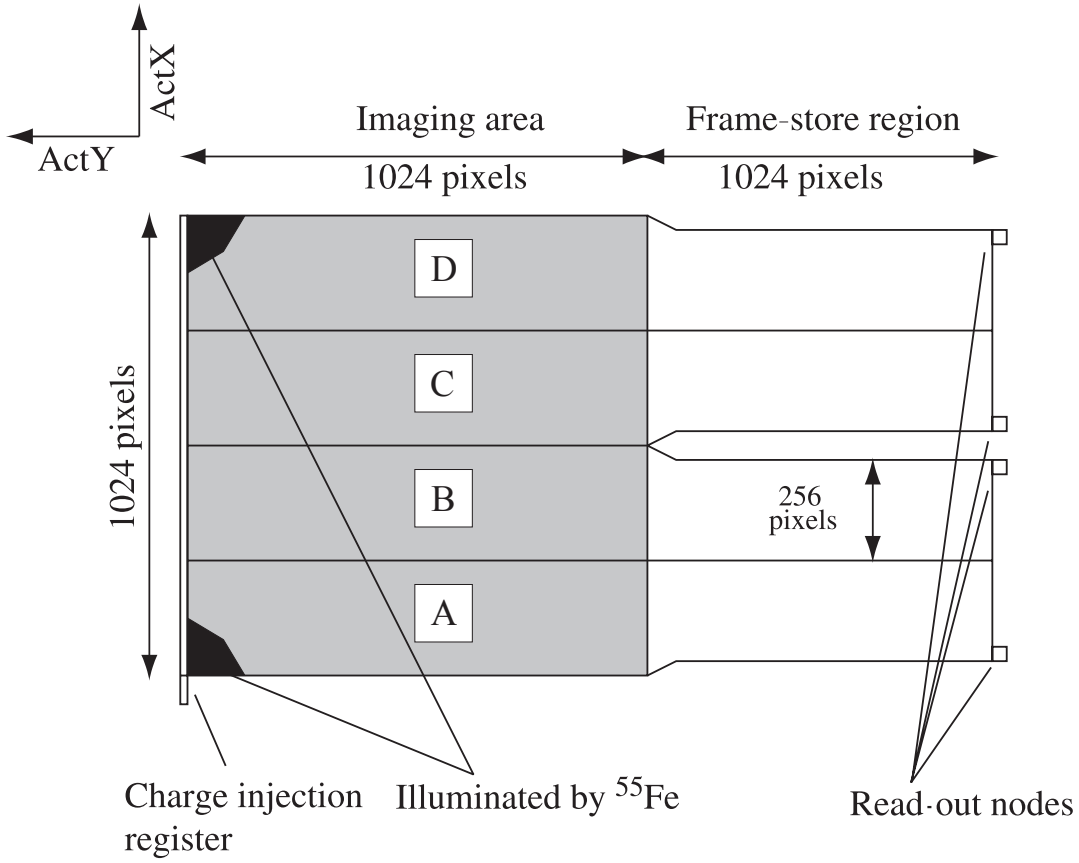

Figure 4.7: A Schematic configuration of one XIS CCD.

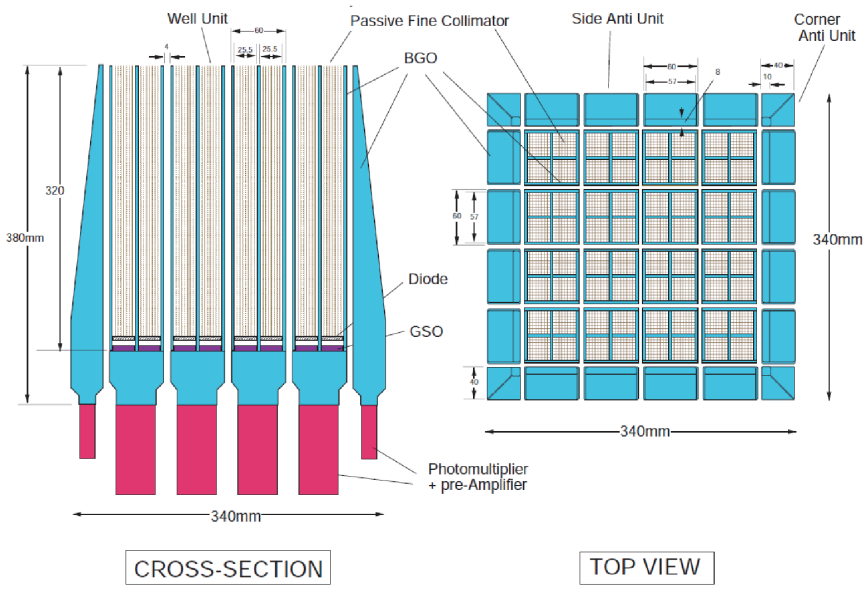

Figure 4.8: Side (left;cross-sectional) and top views of the HXD, taken from Takahashi et al. (2007).

4.1 The Hard X-ray Detector (HXD)

In addition to the soft X-ray (0.2-12 keV) coverage by the XIS, *Suzaku* also covers a broad hard X-ray band (10-600 keV) with the HXD, placed on the side panel, as seen in figure 4.1 (b). As shown in figure 4.8, the HXD sensor consists of an array of 4×4 detector units, and a surrounding active shield made by twenty BGO crystal scintillators . Each unit is a composite, made of GSO/BGO phoswich scintillation and silicon PIN detectors with a thickness 2 mm. The PIN detectors are located inside a well-shaped active shield made of BGO scintillator, and cover 10-70 keV X-ray energies. Harder X-rays penetrating the PIN detectors are detected by GSO scintillation detectors placed beneath the PIN detectors. The GSO detectors are sensitive to 50-600 keV X-rays. The HXD is a non-imaging detector and its filed of view (FOV) is determined by two types of collimators. The well structures made by BGO scintillator collimate hard X-ray to a FOV of $4° \times 4°$, and the fine collimators made by phosphor bronze limit the FOV to $\sim 0.5° \times 0.5°$ in energies below $\sim$ 100 keV X-rays.

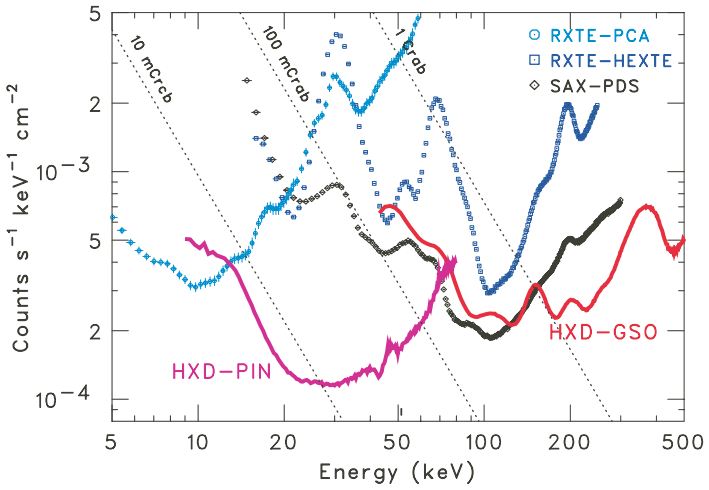

Figure 4.9: Detection sensitivities of various broad-band instruments, including the *Suzaku* HXD, From Takahashi et al. (2007).

Chapter 5

The 1E 2259+586/CTB 109 system

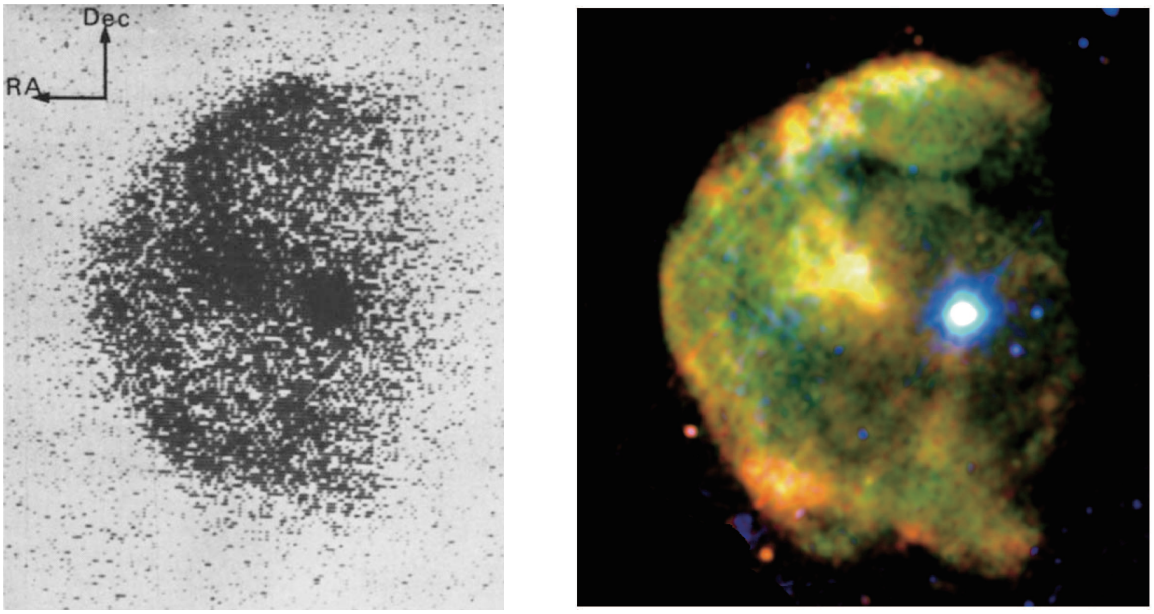

Figure 5.1: Old and new X-ray images of 1E 2259+586 and CTB 109. Left panel is a discovery image taken by Gregory & Fahlman (1980) with *Einstein*. Right panel is a false RGB-color X-ray image taken by *XMM-Newton* (Sasaki et al., 2004).

The system consisting of AXP(Anomalous X-ray Pulsar;) 1E 2259+586 and SNR CTB 109 is one of the typical associations of magnetars and SNRs. In 1980, the association was first discovered at the same time by the *Einstein Observatory* as a compact and a diffuse X-ray sources, respectively (Gregory & Fahlman, 1980). Figure 5.1 shows the discovery image and a recent one of the association. The AXP and SNR are both bright X-ray source, apparently associated with each other, and are thought to have originated from the same SN explosion. The SNR has a peculiar half-moon shape, and the largest radius among known magnetar-associated SNRs. The system has been studied continually, because both the AXP and SNR have many interesting aspects integrally and individually.

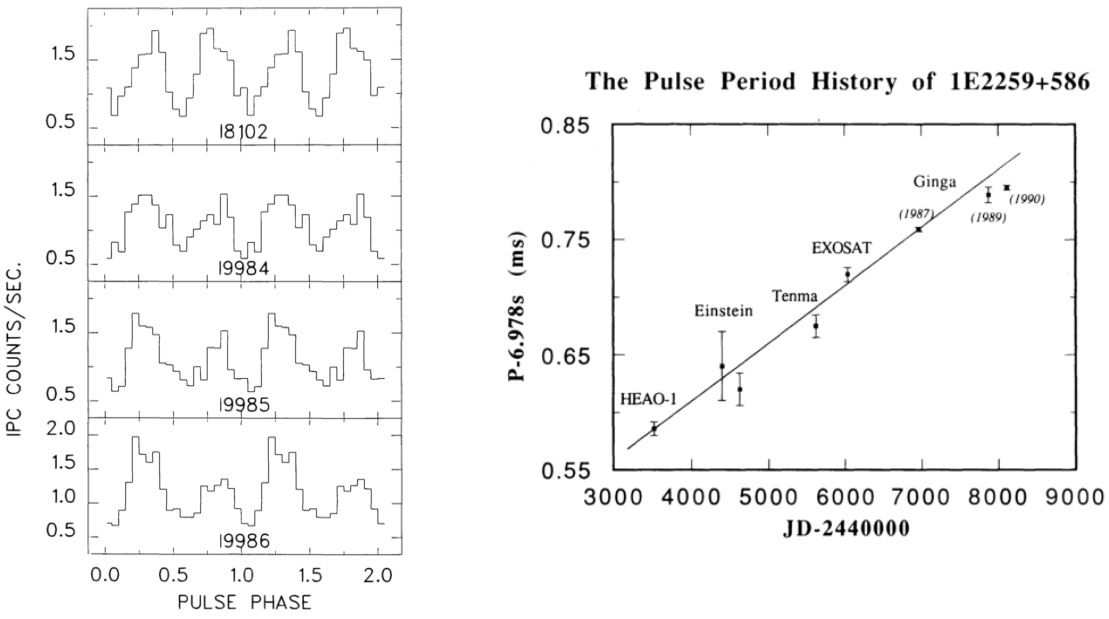

Figure 5.2: The pulse profile and period history of 1E 2259+586. Left panel shows early detection of the pulsation of 1E 2259+586 by Fahlman & Gregory (1983). Top, second, third, and bottom show pulse shapes taken in July/7/1980, January/23/1981, January/24/1981, and January/25/1981, respectively. Right panel shows the history of pulse period of 1E 2259+586 taken from Iwasawa et al. (1992).

5.1 Previous Studies of 1E 2259+586 and CTB 109

5.1.1 1E 2259+586

After the discovery in 1980, 1E 2259+586 was soon identified as an X-ray pulsar. At first, the pulse period was thought to be $P = 3.49$, but this was due to the double-peaked pulse profile, and the fundamental period was soon revised to $P = 6.98$ s (Fahlman & Gregory, 1983). The pulse profiles obtained by Fahlman & Gregory (1983) is shown in the left panel of figure 5.2. Shortly, similar compact X-ray sources having such long pulse periods as $P \sim 2 - 7$ s were discovered, and were classified collectively into AXPs (Anomalous X-ray Pulsars)

The X-ray observations of 1E 2259+586 were continued as a representative of AXPs. As shown in the right panel of figure 5.2, those observations enabled us to measure the spin down rate to be $\dot{P} = 4.8 \times 10^{-13}$ ss^{-1} (Hanson et al., 1988; Iwasawa et al., 1992; Koyama et al., 1987). The results of P and $\dot{P}$ measurements made it clear that the spin-down luminosity (equation 3.6 in §3.1) of 1E 2259+586 (5.6×10^{31} erg s^{-1}) is far insufficient to explain its X-ray luminosity, 1.7×10^{34} erg s^{-1}. Thus, the AXP was thought not to be a rotation-powered neutron star, and is different from radio pulsars.

To explain its X-ray luminosity and long pulse period, 1E 2259+586 was long thought to be an X-ray binary with an orbital period of ~ 2300 s (e.g., Fahlman et al. 1982). A counterpart of 1E 2259+586 was searched with IR, optical and radio observations (e.g., Coe & Jones 1992; Coe et al. 1994; Davies et al. 1989) ; however, no counterpart was found (Hulleman et al., 2000).

Other trials measuring the orbital Doppler modulation in the pulse period were conducted. If the AXP was in a binary system, the photon arrival times would be delayed/advanced by the orbital by the orbital motion as

$$\Delta T = \frac{a_{\rm x} \sin i}{c} \sin\left[2\pi\left(\frac{t}{P_{\rm orb}} - \phi_0\right)\right], \tag{5.1}$$

where $a_{\rm x}$ is semi-major axis, i is the inclination, c is the sped of light, $P_{\rm orb}$ is the orbital period, and ϕ_0 is the phase origin. The trials gave only tight upper limits as $a_x \sin i < 0.8$ light-s (Koyama et al., 1989), $a_x \sin i < 0.6$ light-s (Mereghetti et al., 1998) and $a_x \sin i < 0.028$ light-s (Baykal et al., 1998).

From the late 1980's through 1990's, several attempts were made to explain the pulse properties of AXPs without invoking mass accretion from companion. For example, Carlini & Treves (1989) proposed a precessing neutron star model for 1E 2259+586, Usov (1994) a massive white dwarf model, and Pandey (1996) precessing white dwarf model. Some observational results implying AXPs as isolated objects are gradually accumulated. A strong stability of the pulse period of 1E 2259+586 was revealed by phase-coherent timing solutions from monthly observations with RXTE over 2.6 years (Kaspi et al., 1999). and this result favored non-accretion scenario. Heyl & Hernquist (1999) suggested that spin-down irregularities of AXPs, including 1E 2259+586, are statistically similar to glitches of radio pulsars as isolated neutron stars.

The *magnetar hypothesis* was proposed to explain the sporadic activities of SGRs as magnetically-powered NSs by series of papers of Duncan & Thompson (1992) and Thompson & Duncan (1995), Then, AXPs were generally found to be similar in their behavior to SGRs. Some AXPs, including 1E 2259+586, showed SGR-like X-ray outbursts (Gavriil, 2004; Kaspi et al., 2002; Woods, 2004). Enoto et al. (2010b) found that AXPs and SGRs both obey a common empirical law that holds between their broad-band spectra and characteristic ages. This fact means that both belong to the same class of neutron stars as magnetars. Today, AXPs including 1E 2259+586 are thought to be magnetars as well as SGRs. The strength of the dipole magnetic field of 1E 2259+586 is calculated as 5.9×10^{13} G from its P and $\dot{P}$, which exceeds quantum limit of $B_{\rm QED} = 4.4 \times 10^{13}$ G, but is relatively weak among magnetars.

Recent observations reveal more attractive results on 1E 2259+586. Tendulkar et al. (2013) successfully measured proper motion of 1E 2259+586 and AXP 4U 0142+61. Wu et al. (2013) reported the possible detection of pulsed GeV γ-ray emission from 1E 2259+586 with the Fermi Large Area Telescope. *NuStar* first detected the hard X-ray component from 1E 2259+586 (Vogel et al., 2014), and the result obeys the evolutionary relation derived by Enoto et al. (2010b). Archibald et al. (2013) conducted monitoring of 1E 2259+586 with the *Swift X-ray Telescope* every 2-3 weeks from July 2011, and caught a sudden spin-down, so called anti-glitch in 2012. This spectacular phenomenon have provoked many attractive interpretations (e.q., Quark-nova model;Ouyed et al. 2014, wind braking scenario; Tong 2014).

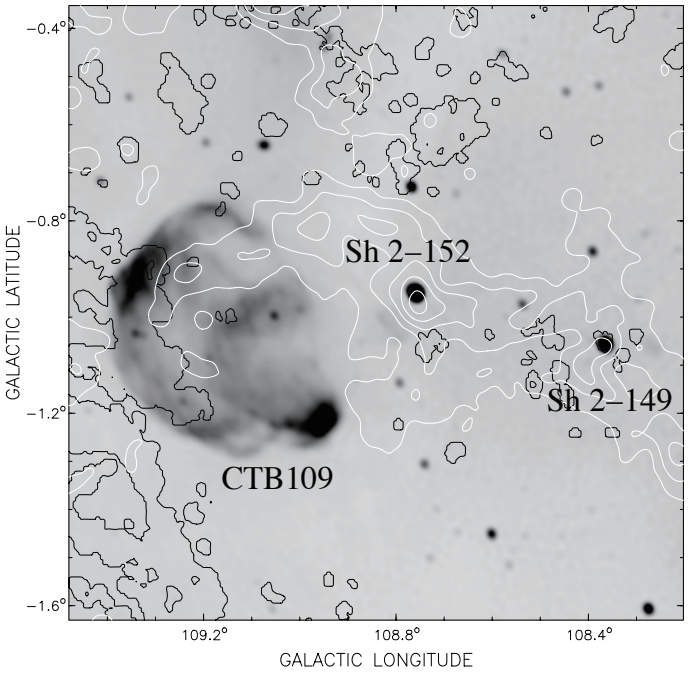

Figure 5.3: A composite image of CTB 109 and its environment compiled by Kothes & Foster (2012). Gray scale shows a radio continuum image at 1420 MHz (originally from Taylor et al. 2003), the white contours are ^{12} CO(1-0) emission from molecular cloud, and the black contours represent H_I self-absorption features by The Canadian Galactic Plane Survey (details in Gibson et al. 2005a,b).

5.1.2 CTB 109

The Galactic diffuse X-ray source CTB 109 is well known as a representative SNR hosting a magnetar 1E 2259+586. This SNR is also famous for its peculiar half-moon shape, as already shown in 5.1. Soon after its X-ray discovery, it was independently identified as a shell-type SNR by radio observations at 610 MHz (Hughes et al., 1981). A 10 GHz radio map taken with the Nobeyama Radio Observatory revealed good positional coincidence between the radio and X-ray shells, while detected no significant enhancement from 1E 2259+586 (Sofue et al., 1983).

Through CO molecular line (C-13)O (J=1-0) observations, Heydari-Malayeri et al. (1981) revealed a physical association between CTB 109 and the complex parts of a giant molecular cloud (GMC) that is located to the western side of the SNR. Tatematsu et al. (1987, 1985, 1990) suggested that the molecular cloud may have disturbed the SNR on the western side. Figure 5.3 shows a radio image of CTB 109 and the GMC, taken from a recent paper by Kothes & Foster (2012), to display environment of the SNR.

The distance to the 1E 2259+586/CTB 109 system has been studied for a long time. In early studies, the $\Sigma - D$ relation was used to obtain a distance estimate of 4.1 kpc (Sofue et al., 1983) and 5.6 kpc (Hughes et al., 1984). Combining analysis of H_I, CO and H_{II}, Kothes et al. (2002) concluded the distance to be 3.0 ± 0.5 kpc. Tian et al. (2010) suggested a new distance

estimate, 4.0 kpc by analyzing 21 cm H_I line and ^{12}CO line spectra of CTB 109 as well as of an H_I region and adjacent molecular cloud complex. Kothes & Foster (2012) gathered evidence that CTB 109 locates within or close to the Perseus arm spiral shock, and conclude a new revised distance of 3.2 ± 0.2 kpc.

Since the discovery by *Einstein*, CTB 109 (as well as 1E 2259+586) had been observed repeatedly by successive X-ray observatories (e.g., Hurford & Fesen 1995; Rho & Petre 1997 for *ROSAT*, Corbet et al. 1995 for *ASCA*, Parmar et al. 1998 for *BeppoSAX* and Patel et al. 2001 *Chandra*). A comprehensive X-ray study was conducted by Sasaki et al. (2004), who synthesized five pointings with *XMM-Newton* and obtained the X-ray image of CTB 109 as already shown in figure 5.1. Assuming a distance of $D = 3.0$ kpc, they estimated the shock velocity, age, and the explosion energy as $v_s = 720 \pm 60$ km s^{-1}, 8.8 kyr, and $(7.4 \pm 2.9) \times 10^{50}$ erg respectively. *Chandra* observation of north eastern parts of CTB 109 was performed by Sasaki et al. (2006). Combining the *Chandra* observation with ^{12}CO and ^{13}CO data, they revealed strong evidence for an interaction between the SNR shock front and the CO cloud. Furthermore, Sasaki et al. (2013) performed spatially resolved spectroscopy with the *Chandra* data, taking advantage of its high angular resolution. They spectroscopically distinguish emission from the ejecta and that from heated-ISM, and refined the age as 14 kyr.

Studies of CTB 109 are advancing further, with the progress of observation techniques. Castro et al. (2012) detected γ-ray emission coincident with CTB 109 from 37 months data of the *Fermi Large Area Telescope*, even though the X-ray spectra of CTB 109 are dominated by thermal emission and no clear evidence of non-thermal component has been detected so far.

5.1.3 Age problem

One of the mysteries in the 1E 2259+586/CTB 109 system is a huge age discrepancy between the age estimate of NS and SNR. While the characteristic age of the 1E 2259+586 is estimated by equation 3.14 in §3.2.3 as 240 kyr, the SNR age is independently estimated as 14 kyr. As seen in figure 5.1, the system shows very good positional coincidence. Furthermore, their X-ray spectra shows similar values of interstellar absorption represented by the hydrogen column densities as $N_H \sim 7 \times 10^{21} \mathrm{cm}^{-2}$. This means that the estimation of distances to 1E 2259+586 and CTB 109 are well consistent with each other. Thus, the association is doubtless, and the huge age discrepancy is an open issue of the system, namely the *age problem*.

5.2 Observation and Data Reduction

The observations of the 1E 2259+585/CTB 109 system were made on two occasions with Suzaku. Table 5.1 provides the log of these observations, while figure 5.4 shows an X-ray mosaic image of 1E 2259+586 and CTB 109 taken by the *Suzaku* XIS in the two observations. The first observation was performed on 2009 May 25 as a part of *the AO4 Key Project on magnetars* (Enoto et al., 2010b). To approximately resolve the pulsation of the magnetar (with

Table 5.1: Log of Suzaku observations of the 1E 2259+586/CTB 109 system.

Name	Observation ID	α	δ	Start Time	Exposure(ks)
AO4	404076010	$23^h\ 01^m\ 04^s.08$	$58°58'15''.6$	2009-05-25 20:00:17	122.6
NW	506037010	$23^h\ 01^m\ 06^s.96$	$59°00'50''.4$	2011-12-13 06:48:41	40.8
SW	506038010	$23^h\ 00^m\ 26^s.88$	$58°44'13''.2$	2011-12-14 04:47:02	41.4
NE	506039010	$23^h\ 03^m\ 06^s.96$	$58°58'51''.6$	2011-12-15 01:57:25	30.4
SE	506040010	$23^h\ 03^m\ 06^s.96$	$58°40'51''.6$	2011-12-15 18:03:52	30.5
BGD*	501100010	$23^h\ 11^m\ 44^s.86$	$61°57'13''.7$	2011-12-15 18:03:52	30.5

∗A Galactic Plane observation (PI:K.Kuntz), close to the 1E 2259+586/CTB 109 system.

P = 6.97 s), all of three XIS cameras were operated in 1/4-window mode which allows a time resolution of 2.0 s (§4.0.3). The intersection of their rectangular ($17' \times 4'.3$) fields of view of XIS1 and XIS0 and 3 was directed toward the magnetar as the principal target. These data were processed and analyzed in the same way as those from the second observation.

We proposed the second observation, four full-window pointings, for a comprehensive study of CTB 109. It was successfully approved in the *Suzaku* AO6 observation cycle, and was performed on 2011 December 13-14 as summarized in table 5.1. As presented in figure 5.4, almost the entire SNR was thus covered successfully. We employed the XIS data which were prepared with version 2.7.16.31 pipeline processing, and used the calibration data updated in January 2013. The data reduction was performed with the HEADS software version 6.16. The response matrix files (RMFs) and ancillary response files (ARFs) were made by using `xisfrmfgen` and `xissimarfgen` (Ishisaki et al., 2007), respectively.

5.2.1 False-RGB Image

Let us again inspect figure 5.4, the mosaic X-ray image of CTB 109 which was made from all the XIS data listed in table 5.1 (except BGD observation). The brightest point source at the center is the magnetar 1E 2259+586. The two blue rectangles indicate the FOVs of the first observation. The four FOVs of the second observation are indicated by white dashed-boxes and named NW, SW, NE and SE as in this figure.

The peculiar semi-half moon shape can be clearly seen in figure 5.4. The NW and SW observations successfully covered the edge of western shell. The brightest parts of the SNR called *lobe* was covered by the NE observation, and was also complemented by the FOV of XIS1 from the first observation. Northern part of the SNR appears to be brightened as well, and this structure runs across the NW and NE FOVs.

Although a reddish region (indicating softer spectra) is seen in the SE FOV, the false RGB-color is relatively uniform over the entire SNR. In particular, we do not find noticeable color changes associated with the half-moon shape. These features are consistent with previous

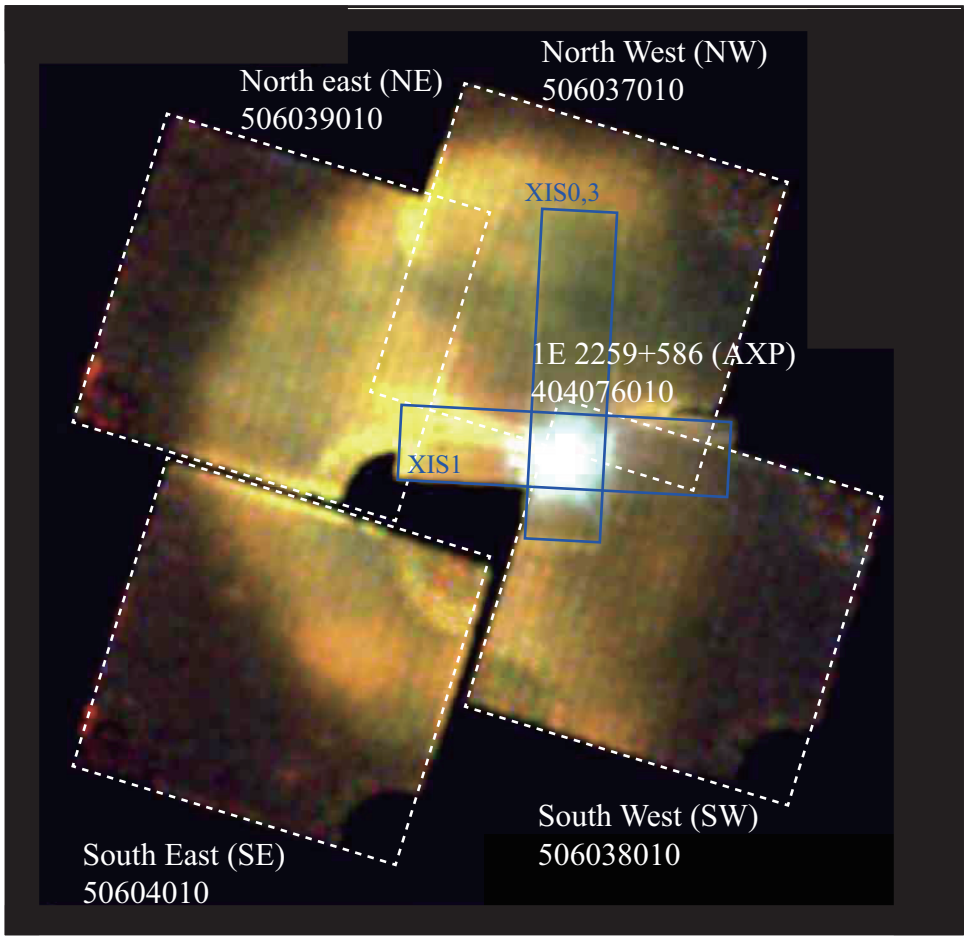

Figure 5.4: Mosaic false-RGB image of CTB 109 taken by the *Suzaku* XIS0,1 and 3. Red, green and blue dots indicate individual X-ray photons with energies of 0.4-0.9 keV, 0.9-1.7 keV and 1.7-4.0 keV, respectively. Non X-ray background was subtracted, and vignetting and exposures were corrected. The first and second observations are indicated by blue rectangles and dashed white squares, respectively.

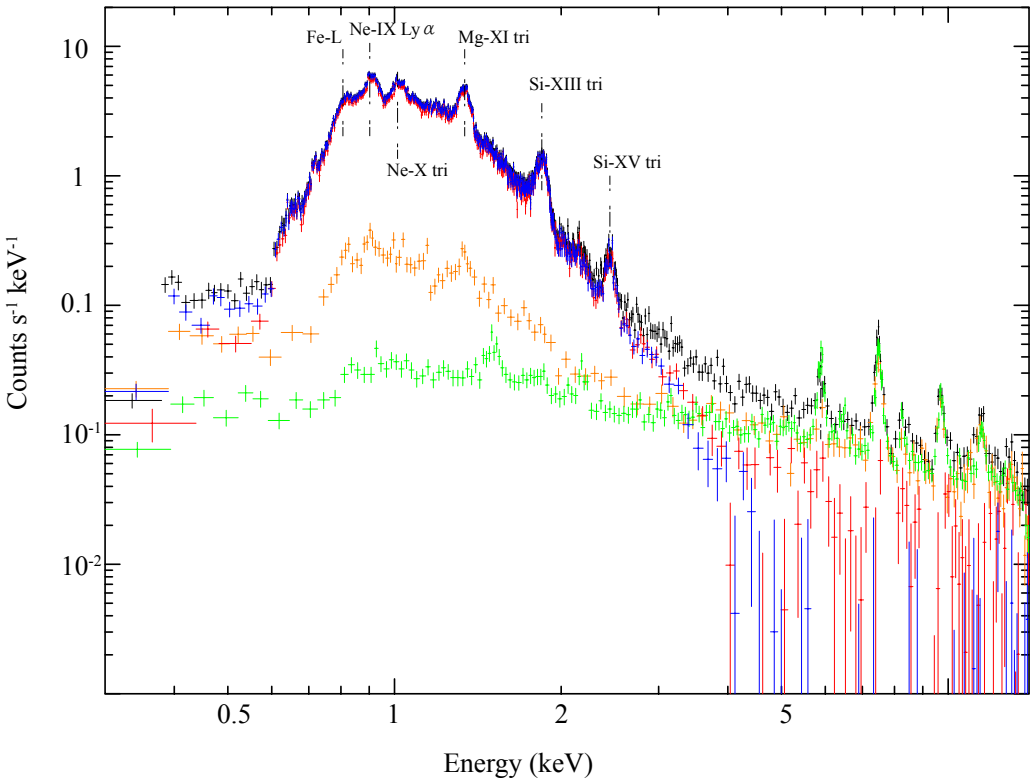

Figure 5.5: Spectra of CTB 109 and the background sky taken with XIS0, to represent all the available XIS cameras. Black is a raw spectrum of CTB 109 extracted from all pointings of the second observation, Orange is a background sky spectrum extracted from a source free region of the second observation, while green is the same but from a Galactic plane observation (ObsID:501100010). Red and blue are spectra obtained by subtracting the orange and green as backgrounds, respectively.

results described in 5.1, such as the *XMM-newton* observation (Sasaki et al., 2004). Unfortunately, a dark area just below the *lobe* was not covered by our observations, because of a limitation in the satellite attitude control.

5.2.2 Background

Before entering upon a detail spatially-resolved spectral analysis, we extracted a spectrum from the entire region of the second observation, and tested two methods of producing a background spectrum. One is using source free regions (SFR) of our second observation, and the other is utilizing a Galactic plane observation (GP) in the archival data of *Suzaku* . Figure 5.5 shows the on-source CTB 109 spectrum, together with the two background spectra. Spectra after subtracting these backgrounds are also added in this figure. Although the spectrum of SFR is different from that of GP in soft energies between 0.6 to 2.5 keV due to leaked emission

Table 5.2: The best-fit parameters and χ^2 values of the whole spectra of CTB109*.

	XIS0	XIS1	XIS3
	E (eV)	E (eV)	E (eV)
Fe complex	806^{+3}_{-2}	244.6^{8}_{-6}	804^{2}_{-3}
Ne-IX triplet	$904.1^{+0.7}_{-0.4}$	914 ± 2	899 ± 1
Ne-X Lyα	$1018.6^{+1.4}_{-2.6}$	1026 ± 2	1012 ± 2
Mg-XI triplet	$1334.5^{+0.8}_{-0.2}$	1343^{1}_{-2}	1333 ± 1
Si-XIII triplet	1851 ± 2	1853 ± 2	1846 ± 2
S-XV triplet	2450^{+5}_{-8}	2446^{8}_{-6}	2436 ± 1

* After applying the gain connections tabulated in table 5.3

form CTB 109, their difference is less than ~3 % of the SNR signal, and does not affect the results. The two background spectra well coincide with each other above ~ 5 keV, and no significant emission remains in either background-subtracted spectra. In the 0.6-4.0 keV band which is most crucial for the SNR spectroscopy, the difference between the two backgrounds is negligible. Avoiding the background ambiguity toward lower energies, below we set an energy region of interest as 0.6-4.0 keV for spectral analysis. Because of higher photon statistics of GP and leaked emission of SFR background, we decided to use the GP background.

5.2.3 Line fitting and self calibration

The background-subtracted spectra in figure 5.5 apparently show features of thin-thermal plasma emission as reviewed in §2.3.3 and §2.3.1, namely, strong characteristic emission lines due to highly ionized ions and exponential continuum from thermal bremsstrahlung. To measure center energies and intensities of these emission lines, we first tried to fit the spectra with a phenomenological model that consists of a continuum and gaussian emission, both subjected to interstellar absorption. We employed multiplicative model called `phabs` (Balucinska-Church & McCammon, 1992) for the absorption.

Figure 5.6 shows results of this model fitting in linear-logarithmic plots. Continuum spectra above ~ 2 keV, almost free from the absorption, indeed show single exponential slope. Although the spectra around 1 keV are more complex due to the emission lines and the absorption, the continuum has a slope significantly different from that in higher energies. This suggests that the spectra consist of at least two plasma components.

The spectra clearly show strong emission lines around 0.9 keV, 1.33 keV, 1.85 keV, and 2.45 keV, which can be identified, based on their energies, with Ne-X Lyα, Mg-XI triplet, Si-XIII triplet and S-XV triplet, respectively. Interestingly, features of Ar-XVII triplet lines are not seen around 3 keV (see table 2.1 in review §2.3.3) in any XIS cameras, while the continua are significant. This suggests that the plasma have rather low Ar abundance. Properties of these

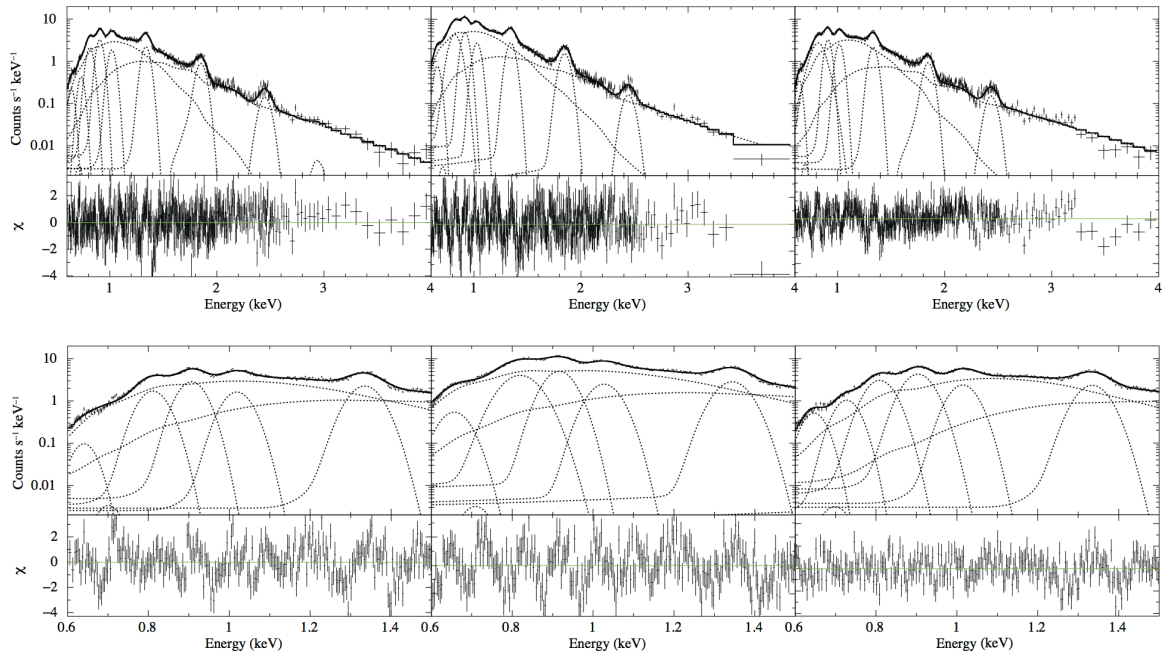

Figure 5.6: Background-subtracted spectra of the whole CTB109 fitted by the phenomenological models. Panel (a),(b) and (c) are made from XI0, 1, and 3, respectively. Lower panels expand soft X-ray range around 1 keV. These spectra include the responses of the XRT and the XIS.

lines are listed in table 5.2. To improve energy calibration accuracy, we trimmed the "gain parameters" of the XIS as a liner function of energy, so that the fitted line-center energies agree better with their theoretical values (§2.1). The determined gain parameters of the XIS cameras are shown in table 5.3. The obtained results agree, within typical XIS calibration uncertainties, with the ideal case of slope= 1.0 and offset= 0.0.

Table 5.3: Sets of the gain parameters.

	XIS0	XIS1	XIS3
slope	1.00536	1.00093	0.988415
offset (keV)	-0.012879	0.000871159	0.00777786

5.2.4 Fitting with plasma emission models

We next fitted the same spectra with plasma-emission codes included in the standard spectral fitting package `xspec`, to perform the plasma diagnostics of CTB 109. Although the existence of two plasma components is suggested by the phenomenological fittings in §5.2.3, we applied a single temperature non-equilibrium ionization model called `NEI` to the spectra. The abundances are first fixed to that of solar values given by Anders & Grevesse (1989); it was apparently far from acceptable. Even if we employed `VNIE` models, which allows individual elements to have

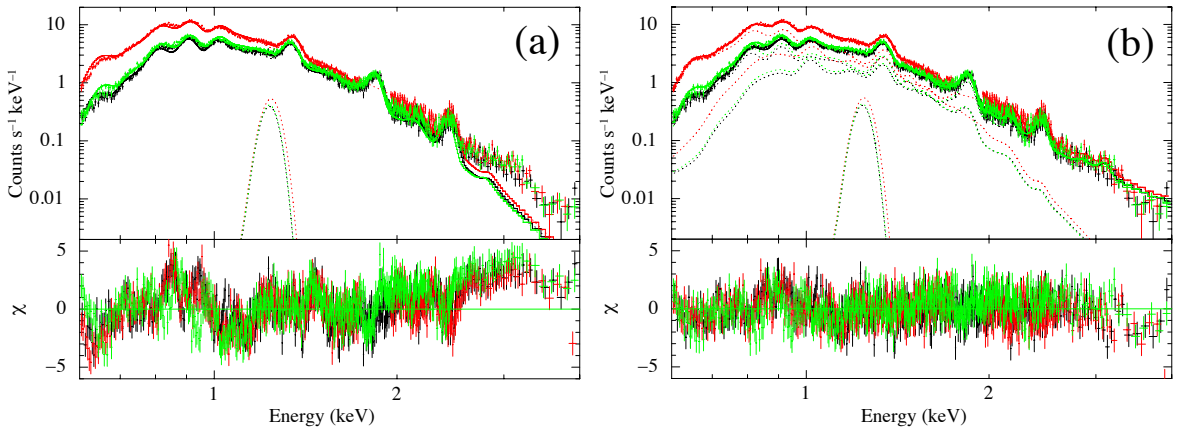

Figure 5.7: The same as figure 5.6, but fitted simultaneously with physical plasma emission models, and shown in log-log format. Panel (a) employs a single-temperature `VNEI` models, while panel (b) two-temperature `VNEI` modeling. Black, red and green represent XIS0, 1 and 3, respectively. Solid lines mean the total model prediction, and dotted lines indicate contributions from individual model components. Lower panels show the fit residuals.

separate abundances, the reduced χ^2 did not become smaller than 2.0. As shown in figure 5.7(a), the model failed to explain the spectra of CTB 109 particularly in < 1 keV and $\gtrsim 2.5$ keV. This fit failure reconfirms the deviation from a single-temperature condition. Indeed, the intensity ratio of He-like and H-like Ne ions (figure 5.6, table 5.2) indicates a single-phase temperature of 0.15-0.3 keV (figure 2.14), which is too low to explain the continuum in > 2.5 keV.

We hence applied two-temperature `NEI` (`VNEI`) model to the spectra. The result is shown in figure 5.7 (b). A gaussian line was added at $\sim$ 1.2 keV to express the Fe-L series, which is not correctly included in the present emission code. Thus, the fit has been much improved from $\chi^2/\nu = 3.88$ to $\chi^2/\nu = 1.42$, and is considered to be acceptable given the background and response uncertainties. The two (hotter and cooler) components are seen to cross over at $\sim$ 1.5 keV. The results of the single and two-temperature models are listed in table 5.4, where errors are quoted at the 90 % confidential level. Thus, the two temperatures have been obtained as $kT_1 \simeq 0.67$ keV and $kT_2 \simeq 0.23$ keV with a factor ~ 3 difference. The metal abundances are approximately ~ 1 Solar, except the very low Ar abundance (< 0.3 Solar) as already noticed in §5.2.3.

5.3 Spatially Resolved Spectral Analysis

5.3.1 Definition of regions

In order to measure how the plasma parameters distribute over the remnant, we defined in total 13 regions as shown in figure 5.8. They were chosen to cover the various structures of the remnant already mentioned in §5.2.1. The bright shell in the northern side of the SNR is covered by Regions 1 and 10, the CO arm by Region 3, the eastern reddish spot by Region 8, and the Lobe Regions by 11 and 12. The southeastern and northeastern areas, with these structures

Table 5.4: Fitting parameters and χ^2 values of the whole-regions spectra of CTB109.

	Model	NEI+VNEI
Absorption	$N_H(10^{22}\mathrm{cm}^{-2})$	0.723 ± 0.002
Surface Brightness	Σ $(10^{-5}\mathrm{erg\ cm}^{-2}\mathrm{sr}^{-1})$	0.183 ± 0.01
	Σ^* (N_H free)	4.86 ± 0.03
Plasma 1		
	kT_1	0.681 ± 0.002
Abundance	Ne	$1.31^{+0.04}_{-0.05}$
(Solar*)	Mg	1.02 ± 0.02
	Si	1.06 ± 0.04
	S	0.76 ± 0.04
	Ar	$0.1(\leq 0.3)$
	Fe and Ni	0.88 ± 0.02
	η_1 $(10^{11}$ s cm$^{-3})$	3.3 ± 0.1
	K_1	$0.98^{+0.01}_{0.02}$
Plasma 2		
	kT_2	$0.240^{+0.001}_{-0.002}$
Abundance	Solar	0.78 ± 0.01
(Solar*)	η_2 $(10^{12}$ s cm$^{-3})$	10(fixed)
	K_2	11.0 ± 0.1
Gaussian		
Center Energy	E	1.244 ± 0.004
Width	σ	< 0.01
Norm	K_G	1.05 ± 0.09
$\chi^2_\nu(d.o.f)$		1.423 (1486)

* The values of solar abundance are given by Anders & Grevesse (1989).
The errors are quoted at the 90 % confidence level.

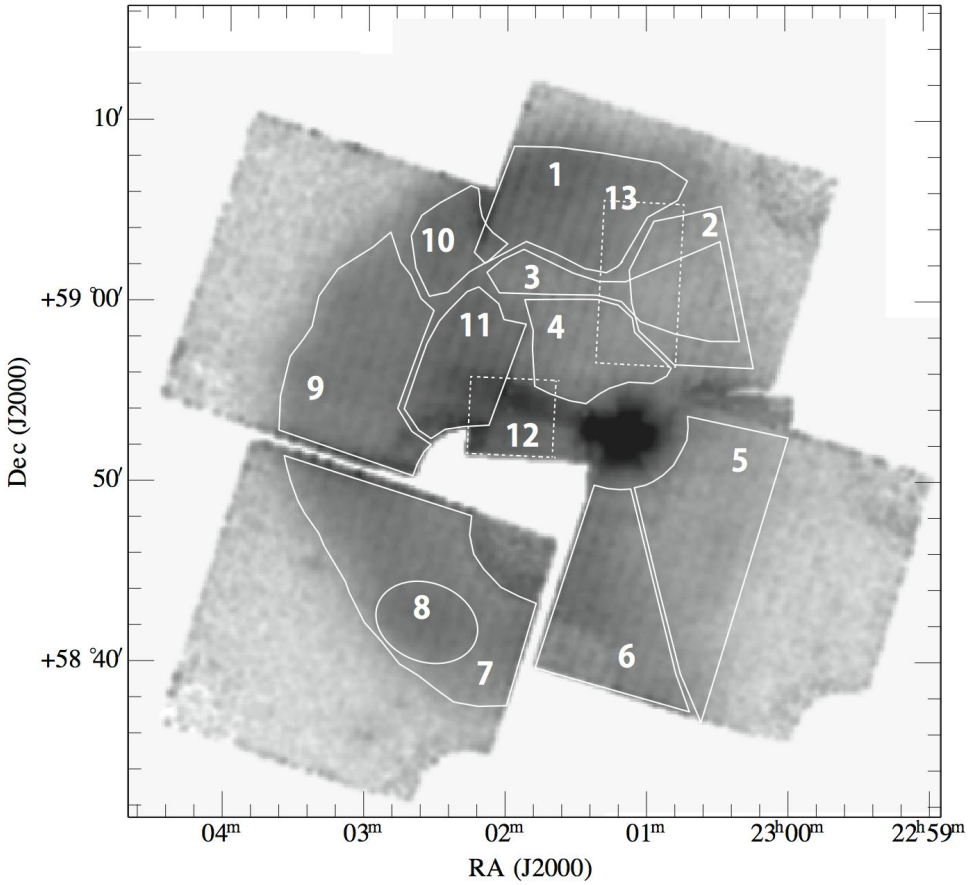

Figure 5.8: The same as figure 5.4, but shown in gray scale to indicate the regions listed in table 5.5. Region 1 through 11, indicated by white solid lines, are from the second observation. The regions enclosed by white doted lines (Regions 12 and 13) indicate the first observation.

.

Table 5.5: The properties of the regions shown in figure 5.8

		Cordinate		Radial Position *	Solid Angle
Regions	FOV	α	δ	θ_r/θ_R	Ω (arcmin^2)
Region 1	NW	$23^h\ 01^m\ 31^s.20$	$58°59'05''.24.0$	0.814	53.64
Region 2	NW	$23^h\ 00^m\ 43^s.20$	$58°59'00''.36.0$	0.622	44.57
Region 3	NW	$23^h\ 01^m\ 04^s.80$	$58°59'00''.36.0$	0.587	34.31
Region 4	NW	$23^h\ 01^m\ 26^s.40$	$58°58'57''.00.0$	0.321	32.04
Region 5	SW	$23^h\ 00^m\ 36^s.00$	$58°58'46''.48.0$	0.584	72.58
Region 6	SW	$23^h\ 01^m\ 16^s.80$	$58°59'42''.36.0$	0.616	58.13
Region 7	SE	$23^h\ 02^m\ 38^s.40$	$58°58'45''.00.0$	0.797	75.96
Region 8	SE	$23^h\ 02^m\ 36^s.00$	$58°58'42''.00.0$	0.855	19.86
Region 9	NE	$23^h\ 03^m\ 04^s.80$	$58°58'56''.24.0$	0.824	70.70
Region 10	NE	$23^h\ 02^m\ 24^s.00$	$58°59'03''.00.0$	0.818	18.70
Region 11	NE	$23^h\ 02^m\ 19^s.20$	$58°58'56''.24.0$	0.504	33.75
Region 12†	AO4	$23^h\ 01^m\ 58^s.44$	$58°58'53''.24.2$	0.272	22.49
Region 13‡	AO4	$23^h\ 01^m\ 04^s.80$	$58°59'01''.12.0$	0.565	39.86

* Angular separation from the SNR center at ($23^h\ 01^m\ 26^s.71$, $58°58'52''.32.1$) united by the semi-diameter of the SNR $\theta_R = 16$ arcmin.

† From the first observation, and only XIS1 was used because of limitated FOV.

‡ From the first observation, and only XIS0 and 3 were used.

excluded are covered by Regions 7 and 9, respectively. Regions 2, 5 and 13 handle the dimmer areas in the western parts of the remnant, where we expect to obtain some clues to the half-moon shape. Regions 4 and 12 are northern and eastern neighbors of 1E 2259+586, respectively. The properties of the regions are summarized in table 5.5. We extracted spectra from these regions and fitted them individually, in the same manner as in §5.2.4. All the extracted spectra were binned to ensure minimum of 50 counts per bin..

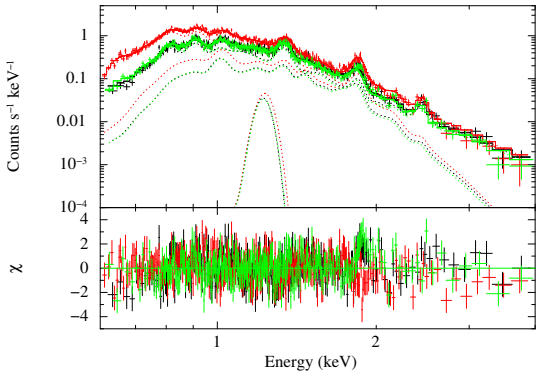

Region 1 (NW)

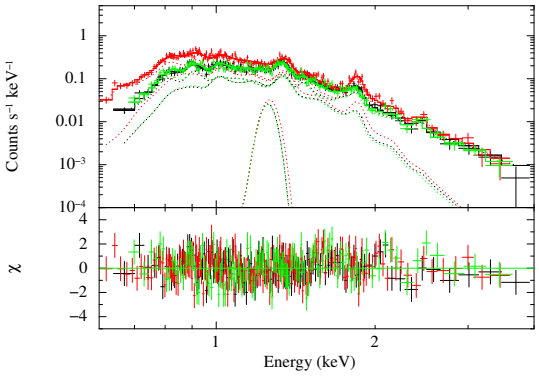

Region 2 (NW)

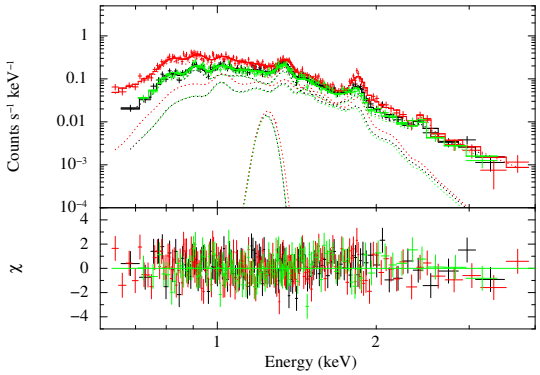

Region 3 (NW)

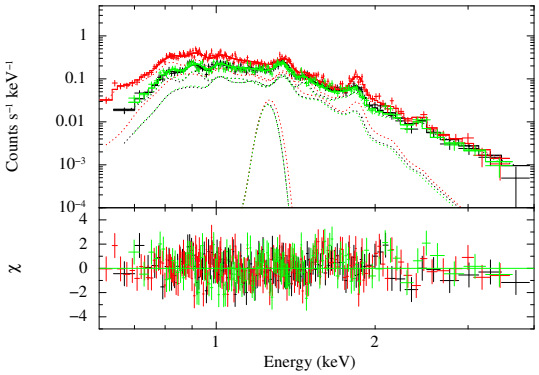

Region 4 (NW)

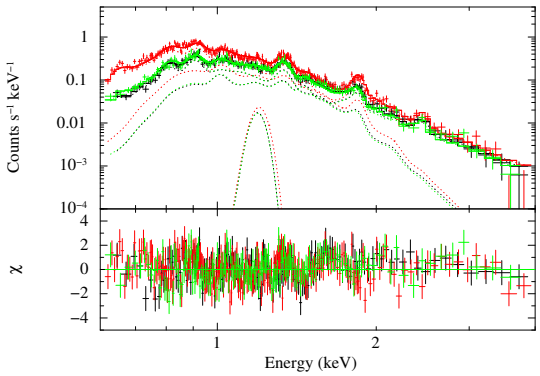

Region 5 (SW)

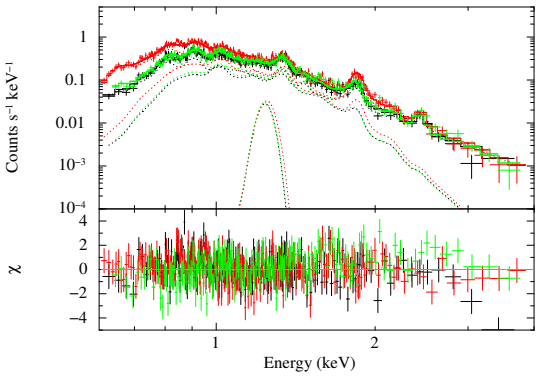

Region 6 (SW)

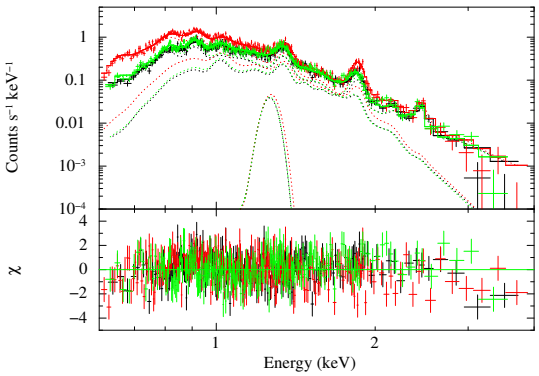

Region 7

Figure 5.9: Spatially resolved spectra

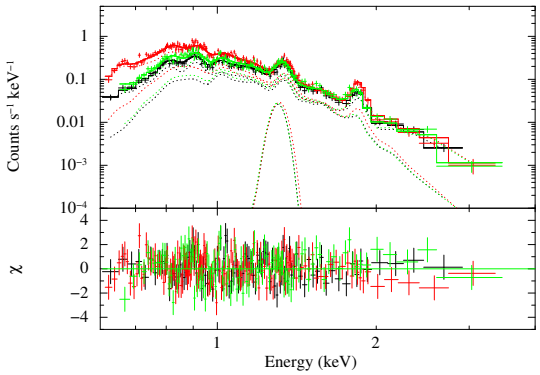

Region 8 (SE)

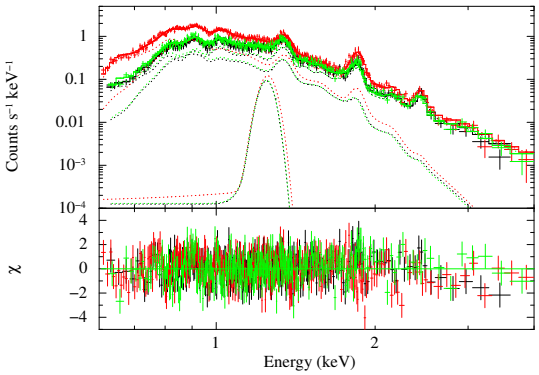

Region 9 (SE)

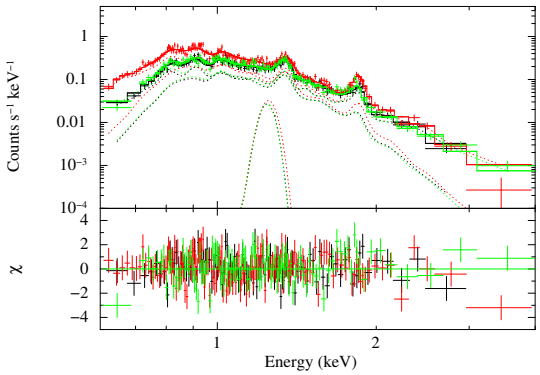

Region 10 (NE)

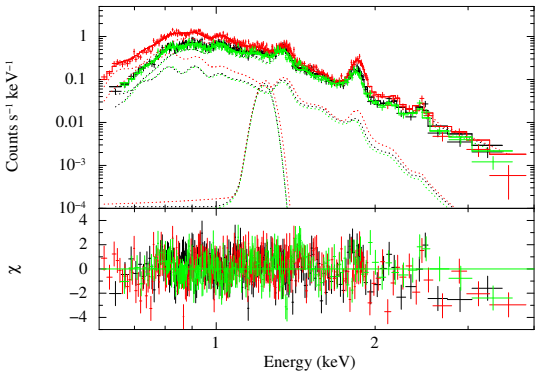

Region 11 (NE)

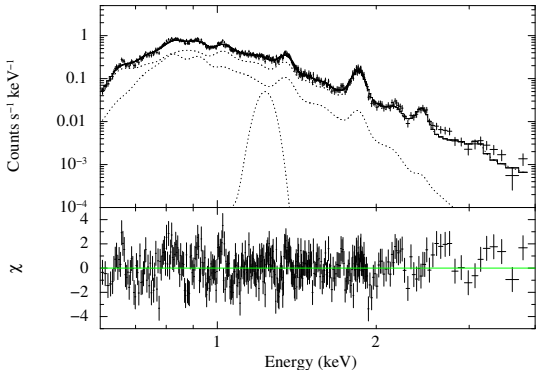

Region 12 (AO4) XIS 1

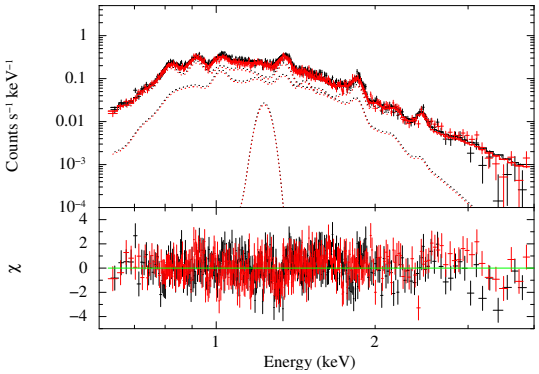

Region 13 (AO4) XIS0 and 3

Figure 5.10: Spatially resolved spectra

Table 5.6: Fitting parameters obtained via the spatially resolved spectroscopy*.

		Plasma 1								Plasma 2			
		$N_{\rm H}$	kT_1	Ne	Mg	Si	S	$n_e t$	K_1†	kT_2†	K_2		
Regions	FOV	(10^{21}cm^{-2})	(keV)	(Solar)	(Solar)	(Solar)	(Solar)	(10^{11}s cm^{-3})	-	(keV)	-	K_1/K_2	$\chi^2_\nu(d.o.f)$
1	NW	$8.1^{+0.1}_{-0.2}$	$0.68^{+0.02}_{-0.03}$	4 ± 1	$1.2^{+0.2}_{-0.1}$	$1.0^{+0.3}_{-0.1}$	$1.01^{+0.26}_{-0.15}$	6^{+2}_{-1}	0.08 ± 0.01	$0.247^{+0.007}_{-0.004}$	$2.1^{+0.2}_{-0.4}$	0.04	1.24(843)
2	NW	8.8 ± 0.02	$0.65^{+0.02}_{-0.01}$	$2.3^{-0.3}_{0.4}$	1.3 ± 0.1	0.7 ± 0.1	0.5 ± 0.2	$16^{+\infty}_{-6}$	0.05 ± 0.01	0.234 ± 0.005	$0.62^{+0.08}_{-0.06}$	0.08	1.03(406)
3	NW	9.4 ± 0.3	$0.68^{+0.07}_{-0.04}$	4 ± 2	$1.5^{+0.4}_{-0.3}$	$1.2^{+0.4}_{-0.3}$	$1.0^{+0.4}_{-0.2}$	Full-EQ	$0.04^{+0.02}_{-0.01}$	0.23 ± 0.01	$0.96^{+0.02}_{-0.04}$	0.036	1.01(361)
4	NW	$7.5^{+0.2}_{-0.3}$	$0.65^{+0.03}_{-0.01}$	$3.5^{+0.8}_{-0.7}$	1.5 ± 0.2	$1.0 \pm s0.1$	$1.0^{+0.3}_{-0.2}$	$18^{+\infty}_{-0.6}$	$0.045^{+0.009}_{-0.006}$	0.23 ± 0.01	0.45 ± 0.01	0.1	1.33(450)
5	SW	$7.6^{+0.2}_{-0.1}$	$0.71^{+0.07}_{-0.03}$	$3.6^{+1.0}_{-0.8}$	1.2 ± 0.2	1.0 ± 0.1	$0.8^{+0.3}_{-0.2}$	$15^{+\infty}_{-5}$	$0.035^{+0.004}_{-0.008}$	$0.223^{+0.004}_{-0.003}$	$0.91^{+0.2}_{-0.1}$	0.04	1.14(522)
6	SW	$7.1^{+0.6}_{-0.5}$	$0.72^{+0.04}_{-0.06}$	2^{+4}_{-1}	0.9 ± 0.1	$0.94^{+0.40}_{-0.15}$	$0.9^{+0.6}_{-0.2}$	$5^{+\infty}_{-2}$	$0.054^{+0.0010}_{-0.016}$	$0.234^{+0.005}_{-0.006}$	0.87 ± 0.03	0.06	1.25(590)
7	SE	$7.4^{+0.2}_{-0.3}$	$0.69^{+0.05}_{-0.01}$	$1.6^{+0.4}_{-0.2}$	1.0 ± 0.1	$1.3^{+0.3}_{-0.2}$	$1.3_{\pm}0.3$	2.2 ± 0.5	$0.08^{+0.01}_{-0.02}$	0.231 ± 0.005	2.05 ± 0.05	0.04	1.27(679)
8	SE	$6.2^{+0.3}_{-0.4}$	$0.62^{+0.06}_{-0.05}$	0.8 ± 0.2	$0.67^{+0.26}_{-0.20}$	$0.96^{+0.28}_{-0.20}$	$0.9^{+0.6}_{-0.5}$	$1.6^{+1.4}_{-0.9}$	$0.038^{+0.008}_{-0.010}$	$0.23^{+0.02}_{-0.01}$	0.5 ± 0.2	0.06	1.23(328)
9	NE	$7.3^{+0.3}_{-0.4}$	0.68 ± 0.01	$0.97^{+0.14}_{-0.10}$	$0.98^{0.07}_{-0.04}$	$0.87^{+0.09}_{-0.06}$	0.8 ± 0.1	2.0 ± 0.2	$0.14^{+0.02}_{-0.01}$	$0.234^{+0.003}_{-0.008}$	$1.1^{+0.1}_{-0.2}$	0.13	1.12(805)
10	NE	$7.3^{+0.4}_{-0.5}$	$0.66^{+0.05}_{-0.03}$	$1.0^{+0.4}_{-0.3}$	1.1 ± 0.2	$0.88^{+0.18}_{-0.14}$	0.5 ± 0.3	$2.7^{+1.0}_{-0.7}$	0.07 ± 0.01	0.25 ± 0.01	0.63 ± 0.02	0.11	1.16(342)
11	NE	5.4 ± 0.2	0.68 ± 0.01	$0.94^{+0.07}_{-0.09}$	$0.92^{+0.07}_{-0.01}$	$0.95^{+0.06}_{-0.07}$	0.6 ± 0.1	$2.1^{+0.3}_{-0.2}$	0.14 ± 0.01	$0.26^{+0.01}_{-0.02}$	$0.28^{+0.02}_{-0.01}$	0.48	1.28(626)
12	AO4	5.9 ± 0.2	$0.65^{+0.02}_{-0.01}$	$0.98^{+0.1}_{-0.2}$	$0.84^{+0.14}_{-0.07}$	$0.99^{+0.05}_{-0.10}$	1.1 ± 0.2	2.5 ± 0.6	0.10 ± 0.01	0.25 ± 0.01	0.43 ± 0.01	0.24	1.45(341)
13	AO4	$9.2^{+0.1}_{-0.2}$	$0.65^{+0.03}_{-0.01}$	$3.6^{+0.5}_{-0.9}$	$1.2^{+0.1}_{-0.2}$	$1.01^{+0.1}_{-0.2}$	0.7 ± 0.1	Full-EQ	$0.053^{+0.009}_{-0.004}$	$0.245^{+0.007}_{-0.008}$	0.9 ± 0.1	0.06	1.16(644)
Whole SNR		7.23 ± 0.02	0.681 ± 0.02	$1.31^{+0.04}_{-0.05}$	1.02 ± 0.02	1.06 ± 0.04	0.76 ± 0.04	3.3 ± 0.1	$0.98^{0.02}_{0.01}$	$0.240^{+0.002}_{-0.001}$	11.0 ± 0.1	0.09	1.423(1486)

* All the errors are quoted at the 90 % confidential level here.

† $\frac{10^{-14}}{4\pi D^2} \int n_e n_{\rm H} dV \times 10^{-1}$

In the same way as §5.2.4, all the spectra were fitted with the two-component model, employing the `NEI + VNEI` modeling. These spectra are shown in figure 5.10, together with the respective best-fit models. In order to reduce the number of free parameters, we decided to fix the abundances of Ar and Fe of Plasma 1 to the values in table 5.4 as determined with the whole-SNR spectra, as well as the abundance of Plasma 2. The additional gaussian was constrained to have a constant K_G/K_1 ratio. All the spectra, including the shell, brighter and dimmer regions, were successfully explained by the model, except Region 12. The fit to Region 12 was improved and made acceptable by the Ar abundance to vary freely.Table 5.6 summarizes the best-fit spectral parameters obtained in this way. Thus, the parameters are rather uniform over all the 13 regions. In particular, the values of $kT_1 \simeq 0.68$ keV (Plasma 1) and $kT_2 \simeq 0.24$ keV (Plasma 2) are both consistent with being the same over all regions.

5.3.2 Eastern shell spectra

The eastern part of the remnant has a smooth round shape, which indicates that the shock wave consisting of a spherical shell has been expanding radially and coherently toward east, and that the density of the surrounding environment is also rather uniform as contrasted by the western side. The spectra of Regions 7 and 9 resemble each other in appearance, and their fitting parameters indeed overlap considerably. The parameters are also close to those of the whole-region spectra listed in table 5.4. Thus, the spectra of Regions 7 and 9 are expected to provide typical plasma diagnostics of the remnant. Including these two regions, Plasma 1 of all spectra extracted from eastern FOV (Regions 7 to 12) show weak non-equilibrium feature as $n_e t \sim 2 \times 10^{11}$ s cm^{-3} ($t \sim 6300\ n_e$ year). This ionization age suggests that the remnant is several thousands years old.

5.3.3 The Lobe and the reddish spot spectra

We found that the lobe spectra extracted from Regions 11 and 12 have two significantly different from those of the eastern shell and the whole-region spectra. These spectra are absorbed by hydrogen column densities of $N_H = 5.4 \times 10^{21}$ cm^{-2} and $N_H = 5.9 \times 10^{21}$ cm^{-2}, which are significantly (by $\sim 2 \times 10^{21}$ cm^2) smaller than those in the other regions. Furthermore, the lobe spectra have larger fractions of the hotter plasma with $kT_1 \sim 0.7$ keV (Plasma 1). While the K_1/K_2 ratios are smaller than $\sim 1/10$ for most regions, the lobe spectra have larger ratios such as $K_1/K_2 \sim 1/4$ to 1/2. The smaller absorption and higher contribution from Plasma 1 are characteristics of the lobe spectra, in addition to their higher brightness.

The spectrum from the reddish spot (Region 8) also has a smaller absorption as $N_H = 6.2 \times 10^{21}$ cm^{-2}. This is the reason why that part appears redder than the other regions in figure 5.1 and 5.4. Having a low ionization age as $n_e t = 1.6 \times 10^{11}$ s cm^{-3}, the plasma in this spot is also considered to be still ionizing. This spectrum does not show any enhancement of the hotter component, in contrast to the lobe spectra.

5.3.4 The NW observation

Compared with the eastern side, the western coasts of CTB 109 that are responsible for the half-moon shape are much more complicated, because of the molecular cloud (figure 5.3). The most important conclusion from table 5.6 is that these regions do not exhibit any enhancement in N_H except CO arm

(Region 3), beyond a typical upper limit of $\sim 1 \times 10^{22}$ cm^{-2} which is far too low to affect the X-ray brightness in ≥ 1 keV. Therefore, the lack of X-ray emission on the eastern half is unlikely to be caused by excess absorption alone; further studies continue in §5.6.1. Interestingly, plasma in all the northeastern regions, including Regions 1, 2, 3 and 4, are totally or nearly in full equilibrium ionizations ($n_e t \geq 10^{12}$s cm^{-3}). Although the ionization age becomes insensitive when a plasma is approaching equilibrium, it is clear that these regions have larger ionization ages than the eastern side of the remnant, and hence relatively higher densities.

North pole of the remnant (Region 1) is brightened like the lobe, but it shows a higher column density than the other. Even though the *Suzaku* XIS has an insufficient angular resolution, we extracted the spectra from the region overlapping with the CO arm (Region 3) like in the series of papers by Sasaki et al. (2006, 2013, 2004), and successfully reconfirmed the prominent enhancement of the absorption therein. Regions 2 and 13 also show considerably absorbed spectra. In contrast, the spectra of Region 4 does not show noticeable deviation from the whole-SNR properties, except larger $n_e t$. Therefore, the SNR in this region is considered to have been freely expanding (along the line of sight), like the lateral expansion of the eastern half.

5.3.5 The SW observation

The southeastern part of the remnant has a stepwise structure running from northeast to southwest. The brightness changes rather abruptly across the structure (see figure 5.1 and 5.4). Thus, we divided this FOV into two Regions, 5 and 6, as already shown in figure 5.8. Region 5 is the right side of the structure and dimmer, while region 6 to the left is brighter or typical. Surprisingly, they yielded parameters that are very similar to each other, except an obvious difference of the surface brightness. In particular, neither of them exhibit any enhancement in $N_{\rm H}$. Therefore, we need to explain the lack of western half and the stepwise brightness change in the SW FOV, both without invoking simple X-ray absorption by the ambient molecular clouds. The discussion becomes a central subject in §5.6.1.

5.4 Plasma Densities

Through the X-ray spectroscopy of CTB 109, we identified two plasma components and determined their parameters. Using these parameters, let us estimate the densities of the two components which are directly connected to their total masses. Based on the reviews in §5.1, we express the distance to CTB109 as $D = 3.2\ d_{3.2}$ kpc, where $d_{3.2}$ is a scaling factor. The fiducial value of 3.2 kpc is considered reasonable, because the average interstellar medium density is obtained as $N_{\rm H}/d = 0.7 \times 10^{21}$ cm^{-2} when combined with the column density $N_{\rm H} \sim 0.7 \times 10^{22}$ cm^{-2} derived in §5.2.4 (table 5.4). Then, we assume that the SNR has an incomplete sphere with a semi-diameter $\theta_R = 16' \pm 1'$, corresponding to the actual radius $R = (15 \pm 1)\ d_{3.2}$ pc $= (4.6 \pm 0.3) \times 10^{19}\ d_{3.2}$ cm, and its center is located at $(\alpha, \delta)_{\rm J2000} = (23^{\rm h}\ 01^{\rm m}\ 26^{\rm s}.71, 58°58'52''.32.1)$.

The swept-up mass, if estimated from the size of the remnant and the ambient density n_0 (~ 1cm^{-3}) as $(4\pi/3) n_0 m_{\rm H} R^3 = (280\text{–}410)\ d_{3.2}^3 n_0\ M_\odot$, is evidently far larger than the expected ejecta mass. The SNR is hence considered to be in the Sedov-Taylor phase, or entering into more mature phases (§2.1.4), and the swept-up matter forms a relatively thin shell at the outermost radii of the SNR. According to figure

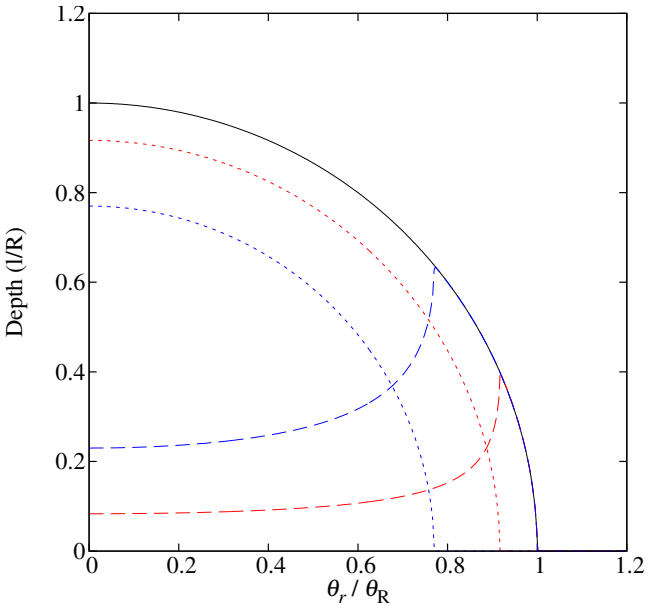

Figure 5.11: An example of the depth calculations with equation (5.3), (5.4) and (5.5). Black solid line is the outer radius of an SNR. Dotted lines are radii of the ejecta sphere (equation 5.4) and dashed lines are projected depth of the SNR shell (swept-up matter; equation 5.5), where red indicates a calculation for $R' = 1/12$ ($f_{\rm ej} j = 0.97$) and blue for $\Delta R = 0.75$ ($f_{\rm ej} = 0.75$).

2.7, we then expect that the reverse shock had already reached the center of the remnant. Therefore, the SNR is considered to be totally filled by X-ray visible plasmas, derived from the spectral fitting as Plasma 1 and 2.

The spectrum fitting of a region gives us so-called emission measure K_1 and K_2, which are defined as

$$K_{1,2} \equiv \frac{10^{-14}}{4\pi D^2} \int n_{\rm e} n_{\rm p}\, dV = \frac{10^{-14}}{4\pi D^2} \int^{l_{1,2}} n_{\rm e} n_{\rm p}\, D^2 \Omega\, dl. \tag{5.2}$$

where $n_{\rm e}$ and $n_{\rm p}$ are the number densities of electrons and protons, respectively, and Ω and $l_{1,2}$ are the solid angles and depths of the region being analyzed. If the plasma were single-phase, we would simply assume a plausible values for l, and employ $n_{\rm e} \simeq 1.2 n_{\rm p}$. However, how to calculate l_1 and l_2 (or equivalently, the respective emission volume) is not trivial if the plasma consists of two phases, like in the present case. We tried to solve this issue with two different ways.

5.4.1 Assuming an outer shell and an inner sphere

As shown in figure 2.2 and 2.6 in §2.1.4, the shell made from swept-up matter is thought to be isolated from the ejecta by a contact discontinuity, and either of Plasma 1 and 2 is responsible for the former and the other for the later. One of the simplest ways to determine $l_{1,2}$ is to specify the thickness ΔR of the shell based on some assumptions. As illustrated in figure 5.11, the depth l through a part of the remnant is described as

$$l = 2R \sin\left\{\cos^{-1}\left(\frac{r}{R}\right)\right\} = D\theta_R \sin\left\{\cos^{-1}\left(\frac{\theta_r}{\theta_R}\right)\right\}, \tag{5.3}$$

where θ_r is angular separation from the center of the SNR, and $r = D\theta_r$ is the actual separation. Similarly, employing a radius of the ejecta sphere $R' = (R - \Delta R)$, a partial depth of the ejecta becomes

$$l_{\rm ej} = 2R' \sin\left\{\cos^{-1}\left(\frac{r}{R'}\right)\right\} = d\theta_R \sin\left\{\cos^{-1}\left(\frac{\theta_r}{\theta_{R'}}\right)\right\} . \tag{5.4}$$

Then, the projected shell depth of the shell is given as

$$\begin{aligned} l_{\rm sh} &= l - l_{\rm ej} \\ &= 2D\theta_R \left[\sin\left\{\cos^{-1}\left(\frac{\theta_r}{\theta_R}\right)\right\} - \sin\left\{\cos^{-1}\left(\frac{\theta_r}{\theta R'}\right)\right\}\right] . \end{aligned} \tag{5.5}$$

From these, the projected volumes of the ejecta and the shell, for a small region with a solid angle $\Delta\Omega$, are calculated as

$$\Delta V_{\rm ej,sh} = D^2 \Delta\Omega \, l_{\rm ej,sh} . \tag{5.6}$$

Integrating these $\Delta V_{\rm ej,sh}$ with respect to $\Delta\Omega$ over the interesting regions, we obtain the emission volumes of the two components, $V_{\rm ej}$ and $V_{\rm sh}$, projected onto them.

Table 5.7 gives the emission volumes and the plasma densities of the regions listed in table 5.5, calculated via equation 5.6 with assumptions of $\Delta R = 1/12$ and $\Delta R = 0.23$. The assumption of $\Delta R = R/12 = 0.08R$, hereinafter called DR008, is obtained by equating the shell mass with the swept-up matter as $(4\pi/3) m_{\rm p} n_0 R^3 = 4\pi m_{\rm p} n_{\rm sh} R^2 \Delta R$, where n_0 and $n_{\rm sh}$ are the number densities of the pre-shock ambient matter and of the shocked gas constituting the SNR shell, respectively, and we employ the Rankine-Hugoniot relation under the strong shock assumption (§2.31) as $n_{\rm sh} = 4n_0$. However, according to figure 2.6, ΔR is considered to be thicker than this rough approximation. We therefore calculated with another assumption of $\Delta R = 0.23$ for a more realistic case (named as R023) and show the results also in table 5.7. Here, we tentatively assumed that Plasma 1 is responsible for the ejecta component and Plasma 2 for the shell, according to Sasaki et al. (2013). As seen in table 5.7, DR008 gives $\sqrt{0.23/0.08} \simeq 1.7$ times larger values of $n_{\rm ej}$ than DR023, because it implies a shell volume which is $0.08/0.23 \simeq 0.35$ times that of DR023 (i.e., $K \propto n^2 V$ is the same).

5.4.2 Assuming pressure equilibrium

Another way to estimate the emission volumes is to assume a pressure equilibrium (PEQ) between Plasma 1 and Plasma 2. The method was used for some systems consisting of thin-thermal plasmas with multiple phases; Ikebe et al. (1999) for intracluster medium with *ASCA* and *ROSAT*, Bocchino et al. (1999) for the Vela SNR with *ROSAT*, and Sasaki et al. (2013) for northeastern side of CTB 109 with *Chandra* .

We first introduce volume filling factors f_i for Plasma i ($i = 1, 2$), considering that Plasma i occupies a fraction f_i of the emitting volume. Either of them is associated with the ejecta component and the other with swept-up matter. Because the reverse shock is considered to have already reached the SNR center as discussed, these f_1 and f_2 should satisfy

$$f_1 + f_2 = 1 . \tag{5.7}$$

Assuming PEQ between Plasma 1 and 2 as

$$n_1 T_1 = n_2 T_2, \tag{5.8}$$

Table 5.7: Emission volumes and densities of the two plasma components, calculated assuming an outer shell of thickness ΔR and an inner sphere.

		$\Delta R = R/12$				$\Delta R = 0.23R$			
	V (10^{57}cm^3)	V_{ej} (10^{57}cm^3)	V_{sh} (10^{57}cm^3)	n_{ej} (cm^{-3})	n_{sh} (cm^{-3})	V_{ej} (10^{57}cm^3)	V_{sh} (10^{57}cm^3)	n_{ej} (cm^{-3})	n_{sh} (cm^{-3})
Region 1	22	14.31	7.65	0.26	1.85	4.24	17.72	0.48	1.21
Region 2	26	21.83	3.91	0.17	1.39	13.46	12.28	0.22	0.79
Region 3	21	18.01	2.77	0.15	2.06	12.40	8.37	0.18	1.19
Region 4	23	20.60	2.15	0.16	1.60	16.73	6.02	0.18	0.96
Region 5	43	36.11	6.40	0.11	1.32	24.26	18.26	0.13	0.78
Region 6	33	26.96	5.64	0.16	1.37	16.24	16.37	0.20	0.80
Region 7	30	20.45	9.88	0.22	1.59	8.50	21.83	0.34	1.07
Region 8	7.5	4.27	3.19	0.39	1.82	(0.40)*	7.06	(1.29)*	(1.23)*
Region 9	25	15.89	9.09	0.33	1.22	4.83	20.15	0.60	0.82
Region 10	7.9	5.19	2.71	0.40	1.69	0.99	6.91	0.91	1.06
Region 11	22	19.33	2.52	0.29	1.17	14.56	7.29	0.34	0.69
Region 12	16	14.75	1.48	0.29	1.89	12.11	4.13	0.32	1.13
Region 13	24	20.77	3.32	0.18	1.74	13.63	10.46	0.22	0.98
Region 13	24	20.77	3.32	0.18	1.74	13.63	10.46	0.22	0.98
Average	–	–	–	0.24 ± 0.17	1.6 ± 0.4	–	–	0.3 ± 0.2*	1.0 ± 0.3*

* The average density of n_{ej} does not include the value from Region 8. The V_{ej} is too small and obviously invalid due to the edge of the SNR.

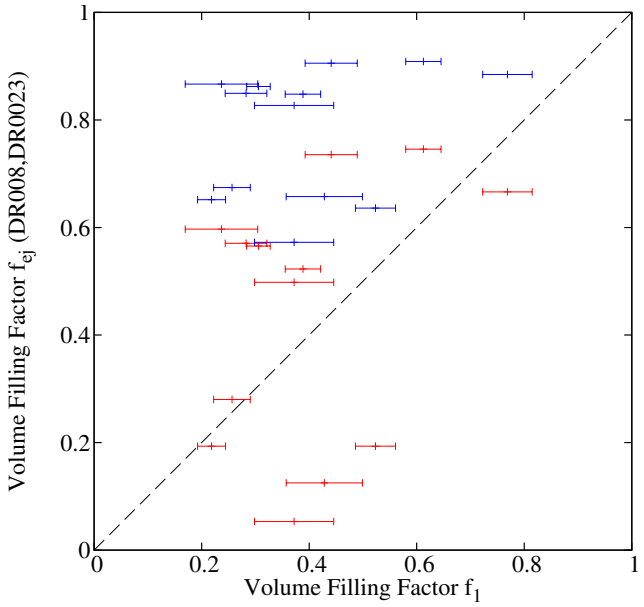

Figure 5.12: Comparisons of f_1 from PEQ(table 5.8), with f_{ej} (also 5.8) calculated with DR008 (blue), or DR023 (red).

where n_i and T_i are the particle density and temperature of Plasma i, these filling factors can be described as

$$f_2 = \left[1 + \left(\frac{n_1 T_1}{n_2 T_2}\right)^2\right]^{-1} \quad \Rightarrow \quad f_1 = 1 - f_2 \,. \tag{5.9}$$

By substituting K_i of equation 5.2 for n_i, equation 5.9 can be re-written as

$$f_2 = \left[1 + \frac{K_1}{K_2}\left(\frac{T_1}{T_2}\right)^2\right]^{-1} \,. \tag{5.10}$$

Since T_1/T_2 is rather constant, f_1 and f_2 are mostly determined by the K_1/K_2 ratio. The emission volume of Plasma i is then obtained with equation 5.3 and f_i as

$$\begin{aligned} \Delta V_i &= f_i \Delta V = f_i \cdot D^2 l \Delta\Omega \\ &= f_i \, d\theta_R \, \sin\left\{\cos^{-1}\left(\frac{\theta_r}{\theta_R}\right)\right\} \, D^2 \Delta\Omega \,. \end{aligned} \tag{5.11}$$

Then, integrating ΔV numerically with respect to $\Delta\Omega$ for each region, we can obtain the emission volumes for Plasma 1 and 2 as $f_1 V$ and $f_2 V$, and estimate the densities of the regions by equation (5.2) as

$$n_{\mathrm{e_i}} = \sqrt{\frac{4\pi D^2 K}{f_i V}} \times 10^7 \,. \tag{5.12}$$

We calculated $f_i V$ and n_i of the individual regions in this way and summarize them in table 5.8. Thus, we generally find $f_1 = 0.3 - 0.4$ and $f_2 = 0.6 - 0.7$, except in Regions 11 and 12 where f_2 becomes rather small. As already understood from equation 5.10, this is a direct result of the higher K_1/K_2 ratios in those regions.

5.4.3 Examination of the results

So far, we have estimated the emission volumes and densities of Plasma 1 and 2 for every region with the different ways (models of DR008, DR023 and PEQ). Let us examine the obtained results, which are already given in tables 5.7 and 5.8. To compare results from the two methods, we calculated the ejecta's filling factor implied by DR008 and DR023 (table 5.7) as $f_{\mathrm{ej}} \equiv V_{\mathrm{ej}}/V$, and show the results on the right two columns of table 5.8. Figure 5.12 compares this f_{ej} with f_1 from the PEQ method. If adopting DR008, the implied values of f_{ej} becomes much larger than f_1, just because of the shell of DR008 is too thin to simultaneously explain K_1 and K_2. To compensate for the small shell volume, it requires relatively high values n_{sh}, so that the pressure are significantly deviated from the equilibrium as $n_{\mathrm{sh}} T_{sh}/n_{\mathrm{ej}} T_{\mathrm{ej}} \simeq 2.6$ (even though the values of $\left\langle n_{\mathrm{ej}} \right\rangle \simeq 0.24$ cm^{-3} and $\langle n_{\mathrm{sh}} \rangle \simeq 1.6$ cm^{-3} are not unusual). On the other hand, the data points of DR023 are equally distributed around slant line meaning $f_1 = f_{\mathrm{ej}}$. The results are similar to those of PEQ. It has the mean densities $< n_{\mathrm{ej}} >= 0.42$ cm^{-3} and $< n_{\mathrm{sh}} >= 1.0$ cm^{-3}, and $n_{\mathrm{ej}} T_{\mathrm{ej}}/n_{\mathrm{sh}} T_{\mathrm{sh}} = 1.2 \pm 0.7$ which is consistent with the pressure equilibrium.

Identification of the two plasma components

With figure 5.12, we found that f_{ej} is made a quantitative estimated with f_1, and hence negatively with f_2. Therefore, as we already assumed tentatively, Plasma 1 (the hotter) is likely to be identified with

Table 5.8: The same as table 5.7, but assuming pressure equilibrium between the two plasma components.

Regions	f_1	f_2	$f_1 V$ (10^{57}cm^3)	$f_2 V$ (10^{57}cm^3)	n_1 (cm^{-3})	n_2 (cm^{-3})	nkT	($\Delta R008$) f_{ej}*	($\Delta R023$) f_{ej}*
Region 1	0.22	0.78	4.80	17.16	0.41	1.13	0.31	0.65	0.19
Region 2	0.39	0.61	9.99	15.75	0.23	0.63	0.16	0.85	0.52
Region 3	0.24	0.76	4.92	15.86	0.27	0.79	0.20	0.87	0.60
Region 4	0.44	0.56	10.03	12.72	0.22	0.60	0.15	0.91	0.74
Region 5	0.28	0.72	12.01	30.50	0.17	0.55	0.13	0.85	0.57
Region 6	0.37	0.63	12.13	20.47	0.21	0.66	0.17	0.83	0.50
Region 7	0.26	0.74	7.78	22.55	0.32	0.96	0.24	0.67	0.28
Region 8	0.37	0.63	2.77	4.68	0.45	1.37	0.35	0.57	(0.05)
Region 9	0.52	0.48	13.09	11.89	0.33	0.97	0.25	0.64	0.19
Region 10	0.43	0.57	3.38	4.52	0.45	1.19	0.32	0.66	0.13
Region 11	0.77	0.23	16.79	5.05	0.29	0.76	0.21	0.88	0.67
Region 12	0.61	0.39	9.94	6.29	0.33	0.84	0.23	0.91	0.75
Region 13	0.31	0.69	7.36	16.73	0.27	0.71	0.19	0.86	0.57
Whole SNR	0.42	0.58	93	129	0.33	0.9	0.26		

* Filling factor calculated as V_{ej}/V from table 5.7.

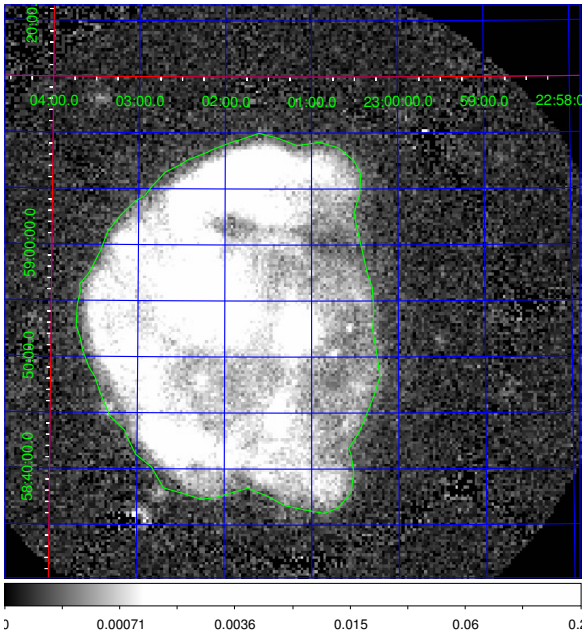

Figure 5.13: The 0.2-1.5 keV image of CTB 109 obtained with ROSAT, used to calculate the actual emission volume estimate V_{CTB}.

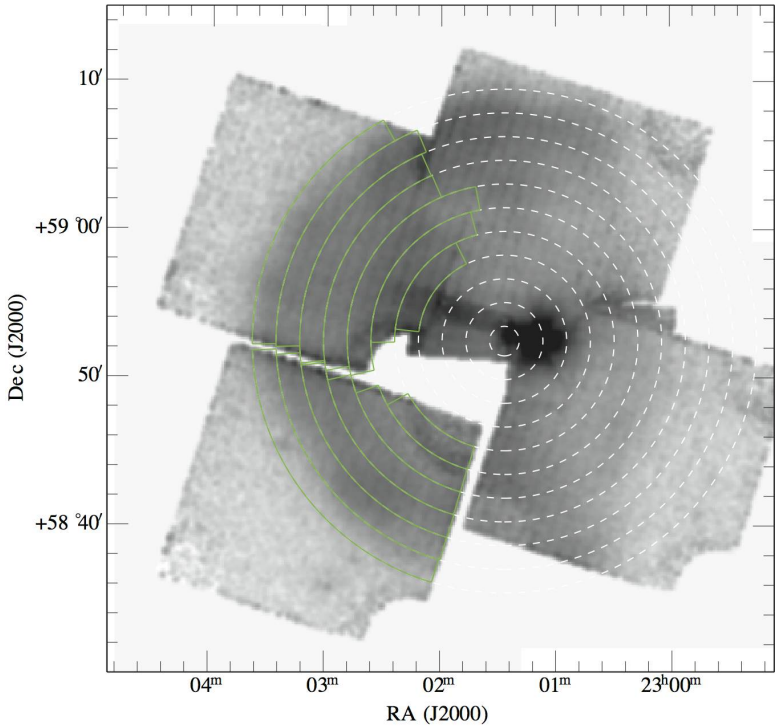

Figure 5.14: Definition of 9 concentric annular regions, used to study radial changes of the spectrum.

the ejecta component. Similarly, Region 1, 7, 8, 9, and 10, which sample relatively outer parts, have an average $f_1 \sim 0.36$, while Region 3, 4, 11, and 12. located closer to the center, have an average $f_1 \sim 0.52$. This also supports the identification of Plasma 1 with ejecta.

To determine the radial dependence of f_1 and f_2 more systematically and unaffected by the azimuthal relations, we newly defined 8 concentric annular regions, as defined in figure 5.14. Since the eastern side of the remnant represent the typical plasma diagnostics, spectra were extracted from the eastern sectors, and fitted with the same model as above. Since we confirmed uniformity of the temperatures of both Plasma 1 and Plasma 2 (5.6), most of the model parameters were fixed to the best-fit parameters of Region 7 and 9, except that K_1, K_2 and $n_{\rm H}$ were allowed to vary. We derived K_1 and K_2 from each annulus, converted them to f_1 and f_2 via equation 5.10, and show the results in figure 5.15 (left) as a function of the projected radius. Clearly, the fraction of Plasma 1 is decreasing with the radius, and that of Plasma 2 by definition has the opposite behavior. Figure 5.15(right) shows line-of-sight depths ($\propto$ column densities) of the two components, obtained by multiplying the depth l of equation 5.3 to f_1 and f_2. These curves nicely make a reproduction of figure 5.11 and reveals the structure of the remnant. The plasma with higher temperature called Plasma 1 fills inner regions of the remnant and corresponds to the ejecta component, while Plasma 2 encloses Plasma 1 and consists of the swept-up matter. We have thus confirmed the identification of Plasma 1 and 2.

The filling factors estimated by assuming PEQ tend to follow those derived by DR023 in most of the regions (figure 5.14). Their differences are consider to be local structures which be dealt with simple spherical shell model as DR023. Considering all these, we concluded that the filling factor of ejecta over the remnant is $f_1 = f_{\rm ej} = 0.43 \pm 0.03$, and its density is $n_1 = n_{\rm ej} = (0.33 \pm 0.04)\, d_{3.2}^{-1/2}$ cm^{-3}. The density of the shell is estimated as $n_2 = n_{\rm sh} = (0.9 \pm 0.2)\, d_{3.2}^{-1/2}$cm^{-3}. We use these values for below discussion.

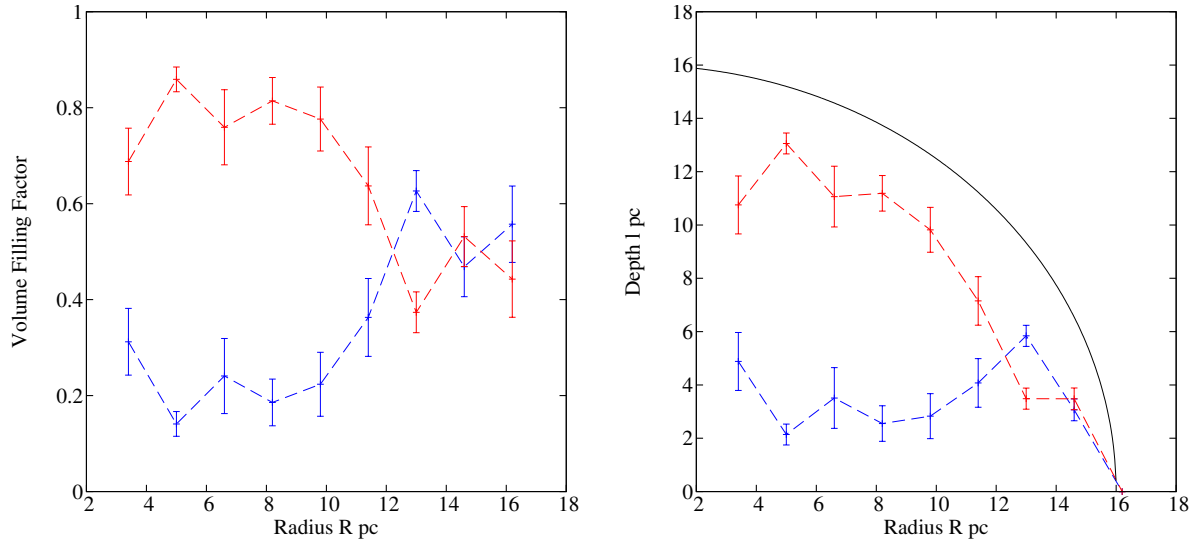

Figure 5.15: The volume filling factors (panel left) and the depths (panel right) of the two plasma components, as functions of the radius R from the SNR center. Red indicates Plasma 1, and blue Plasma 2.

Estimating the total masses of the two plasmas

We can estimate the total masses of Plasmas 1 and 2 from the densities derived above. For simplicity, if we assume an ideal sphere of the SNR, its volume is calculated as $V_R \equiv 4/3\pi\, R^3 d_{3.2}^3 = 4.1\times10^{59} d_{3.2}^3 \mathrm{cm}^3$. Then, the total masses of Plasmas 1 and 2 are estimated using $f_{1,2}$ and $n_{1,2}$ as

$$M_1 = V_R m_\mathrm{H} f_1 n_1 = 43 \pm 8\ M_\odot \tag{5.13}$$

$$M_2 = V_R m_\mathrm{H} f_2 n_2 = 160 \pm 30\ M_\odot\ . \tag{5.14}$$

These estimates are thought to be upper limits, since V_R is based on a spherical assumption and ignores the fact that the Western half is missing.

In order to obtain more realistic volume estimates, we numerically computed the total volume of X-ray visible plasma in CTB 109 in the same manner as §5.4.2. Then, the total volume of X-ray visible plasma has been revised as $V_\mathrm{CTB} = 3.3\times10^{59}$ cm^3. Since this V_CTB is 25 % times smaller than the more conventional V_R, we introduce a new scaling factor $\eta_\mathrm{x} \equiv V_\mathrm{CTB}/V_R = 1/1.25 = 0.8 < 1.0$. The mass estimates, then, decrease by $\sim$ 12 % (because $M \propto nV \propto V\sqrt{K/V} \propto V^{1/2}$), as

$$M_1 = m_\mathrm{H} V_\mathrm{CTB} f_1 n_1 = 39 \pm 7 \quad \left(\frac{\eta_\mathrm{x}}{0.8}\right) d_{3.2}^{5/2}\ M_\odot \tag{5.15}$$

and

$$M_2 = m_\mathrm{H} V_\mathrm{CTB} f_2 n_2 = 140 \pm 30 \quad \left(\frac{\eta_\mathrm{x}}{0.8}\right) d_{3.2}^{5/2}\ M_\odot\ . \tag{5.16}$$

The value of M_1 estimated in this way points to a rather massive progenitor. Further discussion on this subject continues in §6.1.1

The pre-shock ambient density can be estimated using the Rankine-Hugoniot relation, under the strong shock assumption (equation 2.31) as

$$n_0 = \frac{n_\mathrm{sh}}{4} = (0.23 \pm 0.05)\ d_{3.2}^{-1/2}\ \mathrm{cm}^{-3}\ .$$

Assuming uniform ambient density (except western side), the amount of the matter displaced by the remnant is roughly estimated as $M_0 \simeq V_\mathrm{CTB} \simeq 62 \pm 13 M_\odot$ Although M_0 and M_2 are expected to become comparable with each other, M_2 is about twice larger than M_0. This may imply that the ambient density was slightly inhomogeneous. Instead of this, we can estimate n_0 from M_2 as

$$n_0 = M_2/V_\mathrm{CTB} = 0.5 \pm 0.1\ d_{3.2}^{-1/2}\ \mathrm{cm}^{-3}\ . \tag{5.17}$$

This value is thought to be more reliable or realistic for studying the SNR evolution and explosion energy. The mass ratio $M_2/M_1 = f_2 n_2/f_1 n1 = K_2 T_2/K_1 T_1 \sim 4$ does not depend on $d_{3.2}$, and confirms the total mass of the SNR shell is significantly larger than that of the ejecta.

To utilize this information, figure 2.7 is reproduced as figure 5.16, where the horizontal red line indicates the radius (normalized to the epoch of $M_\mathrm{sh} = M_\mathrm{ej}$), calculated as $R = (M_2/M_1)^{1/3} \simeq 1.6$. The specified time (again normalized to the epoch of $M_\mathrm{sh} = M_\mathrm{ej}$) is larger than 1, and the expansion index β (equation 2.1) is sufficiently close to the canonical Sedov-phase value of 2/5. Furthermore, the reverse shock is inferred to have just reached the center. This confirms that CTB 109 is the Sedov phase and justifies our assumptions made in §5.4.

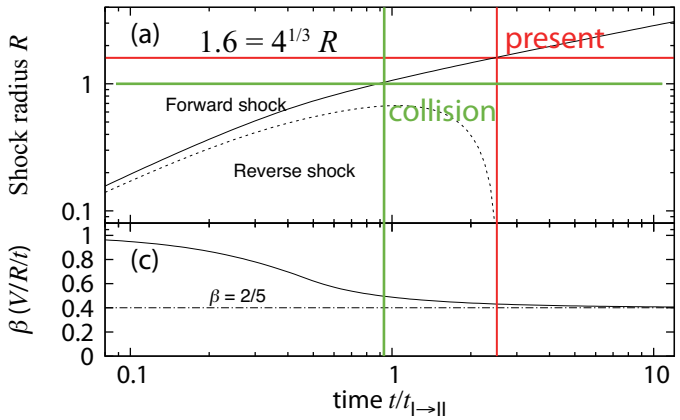

Figure 5.16: The same as figure 2.7, but the evolutionary phase of CTB 109 implied by the present results are shown in red.

5.5 Explosion Dynamics and Evolution of CTB 109

5.5.1 Energy distribution

The obtained temperatures, densities and masses of the two plasma components enable us to study the SN explosion that produced 1E 2259+586 and CTB 109. The total thermal energy included in the (present) remnant is calculated as

$$E_{\mathrm{Th}} = V_{\mathrm{CTB}} \left(f_1 \frac{3}{2} \bar{n}_1 k T_1 + f_2 \frac{3}{2} \bar{n}_2 k T_2 \right) , \tag{5.18}$$

where $\bar{n}_i = \bar{n}_i + 1.2 n_i = 2.2\ n_i$ are the mean number densities of free particles. Assuming the pressure equilibrium again (equation 5.8), it becomes simply

$$E_{\mathrm{Th}} = V_{\mathrm{CTB}} \frac{3}{2} nkT = (4.6 \pm 1.8) \left(\frac{\eta_{\mathrm{x}}}{0.8} \right) d_{3.2}^{5/2} \times 10^{50}\ \ \mathrm{erg} , \tag{5.19}$$

where we employed $nkT = 0.25 \pm 0.10$ keV cm^{-3} for the pressure term. The total luminosity of the thermal radiation is derived from the surface brightness Σ^* in table 5.4 as

$$L_{\mathrm{Th}} = 4\pi R^2\, \eta_{\mathrm{x}}^{2/3}\, \Sigma^* = (1.3 \pm 0.2) \times 10^{36}\, \eta_{\mathrm{x}}^{2/3} d_{3.2}^2\ \mathrm{erg\ s^{-1}} .$$

The SNR has evolved almost adiabatically over its life, because $E_{\mathrm{Th}}/L_{\mathrm{Th}} \sim 300$ million yeas is far longer than the expected age of the system. In combination with the consideration in §5.4.3, it is therefore confirmed that the SNR has not yet entered the radiative cooling phase, but stays in the Sedov-Taylor phase, as reviewed in §2.1.4 and §2.1.5.

The forward shock velocity can be calculated by equation 2.33 as $v_{\mathrm{sh}} = \sqrt{(16 k T_{\mathrm{p}})/(3\mu m_{\mathrm{p}})}$. Substituting $T_{\mathrm{p}} = \epsilon T_2$ in this equation, where $\epsilon \geq$ is the proton-to-electron temperature ratio, we obtain

$$v_{\mathrm{sh}} = \sqrt{\frac{16}{3} \frac{\epsilon k T_2}{\mu m_{\mathrm{p}}}} = (450 \pm 10)\ \epsilon^{1/2}\ \ \mathrm{km\ s^{-1}} . \tag{5.20}$$

Here, we employed $kT_2 = 0.24 \pm 0.01$ keV and $\mu = 0.61$. Then, combining v_{sh} and M_2 (equation 5.16), we can estimate the kinematic energy of the expanding shell as

$$E_{\mathrm{sh}} = \frac{1}{2} M_2 v_{\mathrm{sh}}^2 = (5.4 \pm 1.2) \times 10^{50}\, \eta_{\mathrm{x}} d_{3.2}^{5/2}\ \ \mathrm{erg} . \tag{5.21}$$

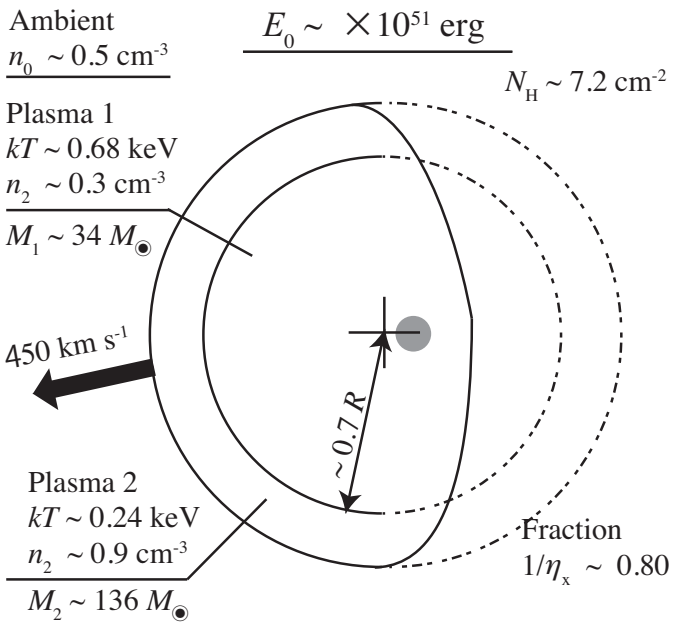

Figure 5.17: A schematic view of CTB 109.

The explosion energy E_0 is estimated in a canonical manner with the Sedov model as described by equation 2.10. This estimate is important, when we compare the explosion energy of an SNR with that of others, since those of most of SNRs are estimated in this manner. The explosion energy of the SN that produced the magnetar 1E 2259+586 and its host remnant CTB 109 is estimated as

$$E_0 = \left(\frac{5}{2}\right)^2 1.15^5 m_{\rm p} n_2 R^3 v^2 = (7.2 \pm 1.6) \times 10^{50}\ \epsilon \eta_x^{-1} d_{3.2}^{5/2}\ {\rm erg}. \tag{5.22}$$

This value is typical for a core-collapse SN explosions.

5.5.2 Age estimates

The age of the remnant $\tau_{\rm snr}$ is calculated using equation 2.7 and 2.8. As indicated by figure 5.16, the present expansion index β of CTB 109 is close enough to 2/5. Hence, employing this value, we obtain an age estimate as

$$\tau_{\rm Sed} = \beta \frac{R}{v_{\rm sh}} = (13 \pm 1)\ \epsilon^{-1/2} d_{3.2}\ {\rm ky}\ , \tag{5.23}$$

which hereafter we call Sedov age. This is consistent with the estimate by Sasaki et al. (2013) mentioned in §5.1.2.

We have another way to estimate the age of CTB 109, namely, using the ionization age $n_e t$. Employing $n_e t = (3.5 \pm 1.0) \times 10^{11} {\rm cm}^3 {\rm s}^{-1}$ of Plasma 1 from table 5.2 and 5.6 (excluding the values of $n_e t > 10^{12} {\rm cm}^3 {\rm s}^{-1}$ obtained from some regions in table 5.6), and $n_{\rm e} = \mu n_1 = 1.2 \times (0.33 \pm 0.04)\ {\rm cm}^{-3}$, the actual age can be computed as

$$\tau_{\rm nei} = (24 \pm 6)\ d_{3.2}^{1/2}\ {\rm ky}. \tag{5.24}$$

Although this is somewhat larger than $\tau_{\rm Sed}$, the time dependence of n_1 is not considered here, and in the past it should have been larger than the present value. Therefore, the actual value of $\tau_{\rm nei}$ would be smaller than this. To see this effect, let us evaluate the expansion effect analytically,

As seen in the spectra in figure 5.5, most of the emission lines of CTB 109 are composed of those from He-like and H-like ions because of the high temperature. If we focus on the interchange between these two ionization state only, equation 2.47 can be approximated as

$$\frac{1}{n_e}\frac{dF}{dt} = \alpha_1 (1 - F) - \alpha_2 = \alpha_1 - \alpha F \tag{5.25}$$

$$\alpha \equiv \alpha_1 + \alpha_2 \,, \tag{5.26}$$

where F is the number fraction of an ionization state which we focus on, and α_1 and α_2 are reaction rates. If rewritten as

$$\frac{dF}{dt} = n_e \alpha (F_\infty - F) \,, \tag{5.27}$$

it can be readily integrated as

$$F(t) = F_\infty \left[1 - \exp\left(-\frac{t - C_1}{\tau}\right)\right] \quad ; \tau \equiv 1/n_{\rm e}\alpha \,, \tag{5.28}$$

where F_∞ means the fraction achieved in full ionization equilibrium as $t \to \infty$, which is determined by the plasma temperature employing Saha's equation (equation 2.46 in §2.4.2), and C_1 is a constant. Then, solving equation 5.28 for t and multiplying by $n_{\rm e}$, the ionization age can be related with the observed value of $F = F_{\rm obs}$ as

$$n_{\rm e} t = n_{\rm e} C_1 - \alpha^{-1} \ln\left[\left(1 - \frac{F_{\rm obs}}{F_\infty}\right)\right] . \tag{5.29}$$

If the plasma is not ionized and totally neutral ($F = 0$) and $C_1 = 0$at $t = 0$, namely, $\tau_{\rm nei} = 0$ at the beginning, the present ionization age is given as

$$\tau_{\rm nei} \sim -\alpha^{-1} \ln\left[\left(1 - \frac{F_{\rm obs}}{F_\infty}\right)\right] . \tag{5.30}$$

When analyzing an X-ray spectrum, we can measure the electron temperature from the thermal-bremsstrahlung continuum, and hence calculate the expected $F_{\rm obs}$. At the same time, the current value $F_{\rm obs}$ can be determined from the observed line rations. These two can be fed to equation 5.30, to determine the ionization age. (Of course, it is usually determined automatically by fitting the spectrum with a plasma emission code.)

If we consider the volume expansion of Plasma 1, its density is described as

$$n_1(t) = \frac{M_1}{f_1 \cdot V_R(t)} = \frac{M_1}{f_1 \frac{4}{3}\pi R(t)^3} = \widetilde{n}_1 \left(\frac{t}{t_0}\right)^{-3\beta'} = \widetilde{n}_1 \tau^{-3\beta'}$$

$$\tau \equiv \frac{t}{t_0} \,, \tag{5.31}$$

where $\widetilde{n}_1$ is the density at a reference time t_0, and β' is the expansion index of the radius R' enclosing Plasma 1 (so-called contact discontinuity). Then, equation 5.27 is rewritten as

$$\frac{dF}{dt} = \widetilde{n}_1 \alpha (F_\infty - F) \tau^{-3\beta'} = (F_\infty - F) \frac{\tau^{-3\beta'}}{\widetilde{\tau}}$$

$$\widetilde{\tau} \equiv 1/\widetilde{n}_1 \alpha \,. \tag{5.32}$$

Integrating equation 5.32 by separating variables, we can obtain a solution as

$$F(\tau) = F_\infty \left[1 - \exp\left\{-\left(\frac{\tau^{1-3\beta'} - C_2}{1-3\beta'}\right)\left(\frac{t_0}{\tau}\right)\right\}\right], \tag{5.33}$$

where C_2 is a constant. When $\beta' = 0$, equation 5.33 reduces to equation 5.28.

The top panel of figure 5.18 shows examples of the evolution tracks of F as a function of t/t_0, calculated with equation 5.33. When the contact discontinuity of an SNR is expanding with keeping the R'/R ratio constant, its expansion index coincides with that of the outer radius. Then, an SNR in the Sedov phase is expected to have $\beta' \simeq \beta = 2/5$. Compared with a plasma in a constant volume bath, the ionization process is thus delayed in an expanding systems. If a system has a smaller expansion index as $\beta' < 1/3$, the delay become smaller as seen in the bottom of figure 5.18, and it will catch up in a finite time. Furthermore, the $F(t,0)/F(t,\beta')$ ratio has a certain lower limit as long as $\beta' > 1/3$, so that the deviations from the non-expanding case must be limited in a certain range. On the other hand, when $\beta' \geq 1/3$, F converge to a value lower than F_∞ as

$$\lim_{\tau\to\infty} F(\tau;\beta';C_2) = F_\infty \left[1 - \exp\left\{-\frac{C_2}{3-\beta'}\left(\frac{t_0}{\tau}\right)\right\}\right] \simeq F_\infty \left(\frac{C_2}{3-\beta'}\right)\left(\frac{t_0}{\tau}\right) . \tag{5.34}$$

Since an expansion with the Sedov model has a large $\beta'(= 2/5 > 1/3)$, an equilibrium point of F may becomes smaller than F_∞ and the SNR will never achieve a full equilibrium until it proceeds to the next phase (i.e., the pressure dominant radiative cooling phase is the next phase with $\beta' = 2/7 < 1/3$; §2.1.1 and 2.1.5). Interestingly that both $\beta' = 2/5$ and $2/7$ is close to the critical value of $1/3$ but former is $> 1/3$ while the latter is $< 1/3$, so the system crosses the boundary during its evolution. Furthermore, $\beta' = 1.0$ is an extreme case which represents free expansion phase (§2.1.2). In such a case (though unrealistic), the SNR would remain in a much lower ionization condition than a non-expanding system of the same temperature.

When $\tau_{\rm nei} \simeq 10^{12}$ s cm^3 (derived by spectral fitting with `XSPEC`), we usually understand that a plasma is usually considered to be in a full equilibrium. Hence, we simply substitute this timescale of $\tau = 10^{12}$ s cm^3 in equation 5.28. Then, a comparison of the theoretical F_∞ against the observed $F_{\rm obs}$ will yield an age estimate via equation 5.28. Since it is easier to obtain, $\tau_{\rm nei}$ directly from the data than deriving $F_{\rm obs}$, we may utilize equation 5.30 inversely to estimate $F_{\rm obs}$. The result can be fed into equation 5.33, to estimate the actual age $\tau_{\rm r}$ that would give the same value of $F = F_{\rm obs}$ when the expansion is considered.

$$F_{\rm obs}/F_\infty \sim \exp\left(-\frac{3.5\times10^{11}}{10^{12}}\right) = 0.40. \tag{5.35}$$

For a practical ease, we may express the true age $\tau'_{\rm nei} = g_{\rm nei}\tau_{\rm nei}$, using a correction factor $g_{\rm nei}$. Then from equation 5.30 it is expressed as

$$\text{CorrectionFactor } g_{\rm nei} \equiv \frac{\ln\left[\left(1 - \dfrac{F(t,\beta)}{F(t,0)|_{\rm obs}}\right)^{-1}\right]}{\ln\left[\left(1 - \dfrac{F_{\rm obs}}{F_\infty}\right)^{-1}\right]} . \tag{5.36}$$

If we employ the smallest value of $F(t,\beta)/F(t,0) \sim 0.7$, we can correct the simple-minded age estimate in equation 5.24, to obtain

$$\tau'_{\rm nei} = g_{\rm nei}\tau_{\rm nei} \equiv \frac{\ln\left[(1-0.4\times0.7)^{-1}\right]}{\ln\left[(1-0.4)^{-1}\right]} = 0.64\ \tau_{\rm nei} = (15\pm4)\ d_{3.2}^{1/2}\ \text{kyr} . \tag{5.37}$$

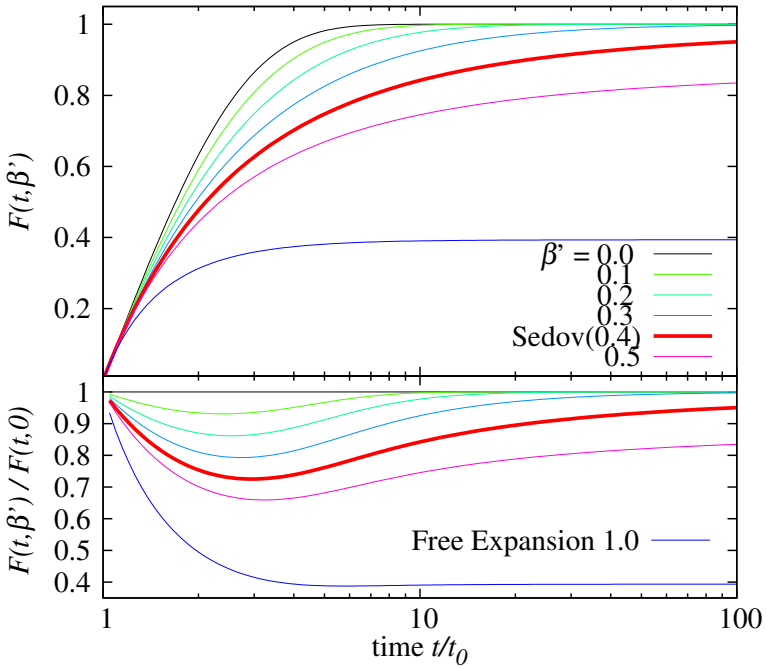

Figure 5.18: The evolution tracks of the ionization fraction F for various β', calculated with equation 5.33. Black line is $\beta' = 0$ which means that the volume and density are constant with time. Red line indicates $\beta' = 2/5$ and means that a contact discontinuity expands with a Sedov expansion. The others change with a step $\beta' = 0.1$. For simplicity, $t_0/\widetilde{\tau} = 1$ and $C_2 = 1$ are employed here. The bottom panel shows the ratios to the case with $\beta' = 0$ (i.e., no expansion).

This corrected value is well consistent with the Sedov age of $\tau_{\rm sed}$ = 13 ky (equation 5.23).

5.6 Interactions between Molecular Clouds

So far, the basic properties of CTB 109 have been clarified to a much deeper extent than before. The remaining issue is how to explain the peculiar half-moon shape of this SNR. Although the GMC (giant molecular clouds in §5.1.2) are considered to be responsible, we need to reconcile the lack of western half with absence of increased absorption (confirmed in §5.6.2)

5.6.1 Collision between the giant molecular clouds

The ionization state of the western side of CTB 109 has been nearly achieved equilibrium compared with the eastern side. This suggests that the SNR is physically colliding with the GMC as illustrated in figure 5.19, rather than the SNR is partially hidden behind the GMC.

Suppose that the SNR expanded to the western edge, at a projected distance $R_{\rm w}$ from the center, by the time $t_{\rm w}$, at which the blast wave hit the GMC. Because $R_{\rm w} is \simeq 30$ % of R measured on the eastern edge (figure 5.13), we can utilize the expansion history of figure 5.16 that $t_{\rm w}$ is ~ 40 % of the SNR age, namely $t_{\rm w} \sim 5$ kyr.

Soon after the collision, the strong reverse shock was formed and was propagating from the west to east. The reverse shock propagating from the western side is considered to have been generated in advance of that from the eastern side, and expected to be stronger, because of the heavy wall made by the GMC. As a result, the volume expansion was decelerated on the western side, and the resultant decrease in β' is considered to enhance the ionization, according to figure 5.18. Therefore, the lager ionization age observed from the western region can be explained at least qualitatively.

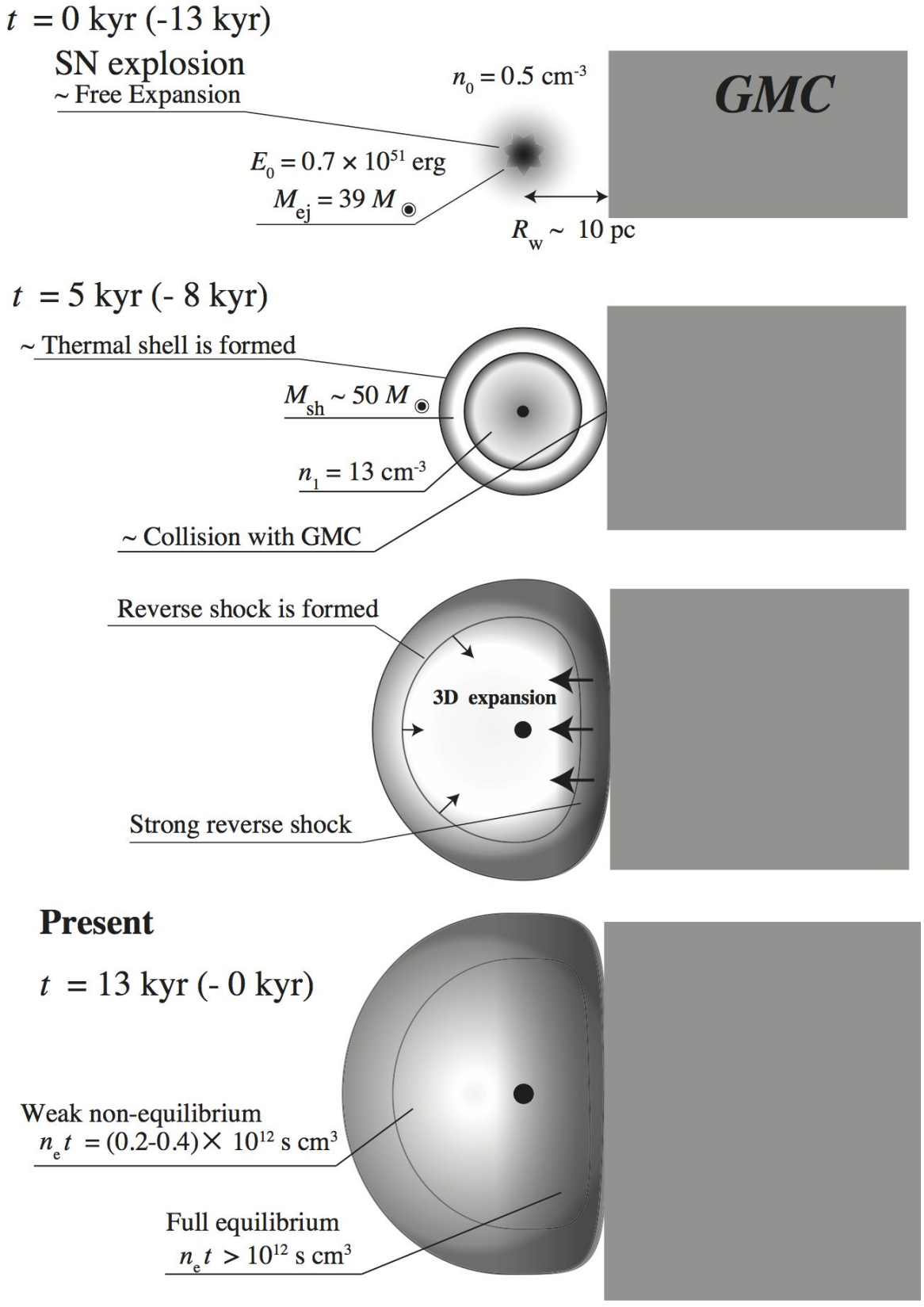

Figure 5.19: A schematic view of the evolution of CTB 109

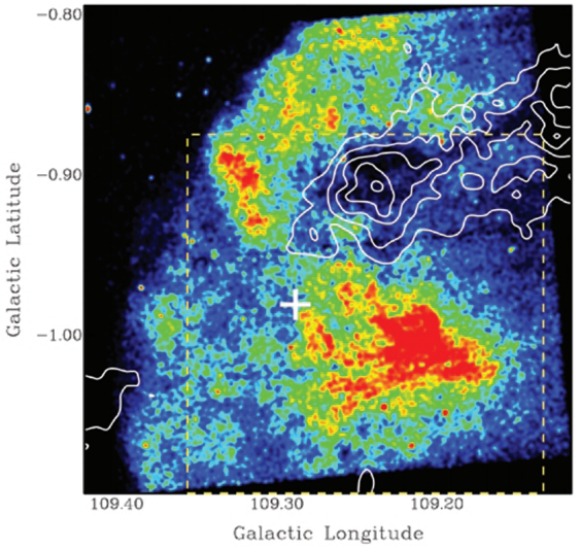

Figure 5.20: A composite image of the part CTB 109 around Regions 3, 9, 10 and 11 in figure 5.8, taken from Sasaki et al. (2006). Color is intensity map obtained by *Chandra* , and white contours are ^{12}CO (1-0) emission of molecular clouds observed by the Five College Radio Astronomy Observatory (FCRAO) 14 m antenna.

5.6.2 Possible geometry at present

We are beginning to understand the past collision of CTB 109 with the giant molecular cloud through the evolutionary calculation of the expansion and the differences of the ionization levels between the western and eastern sides of the remnant. Figure 5.19 assumes a simple flat wall of the GMC and the direction of the line of sight is not considered, which illustrates the line of sight as parallel with the contact plane between the SNR and the GMC. Here, let us consider in a more realistic way the current structure of the western edge, and positional relations between the SNR and the GMC.

CO arm

As already mentioned briefly in §5.3.4, the spectra extracted from Region 3 is absorbed by a hydrogen column density $N_{\rm H} = 9.4 \times 10^{21}$ cm^{-2}, which is larger than those of the other spectra by $\Delta N_{\rm H} \sim 2 \times 10^{21}$ cm^{-2}. This excess absorption is considered as due to the CO arm stretching from the GMC. The amount of the absorbing matter covering Region 3 is estimated as $400 - 500\ M_\odot$, by integrting $\Delta N_{\rm H}$ over Region 3 (with an area of $\sim$ pc^2). $(N_{\rm H,3} - < N_{\rm H} >)\ \Omega_3 \sim 400 - 500\ M_\odot$. This result is consistent with the previous estimate by Sasaki et al. (2006) and Sasaki et al. (2013). Although we do not know the depth of the CO arm, the hydrogen density of the CO arm is inferred as $200 - 1300$ cm^{-3} by a depth assumptions $(3 - 9) \times 10^{18}$ cm (1-3 pc). Thus, we reconfirm that the CO arm is stretching from the body of the GMC in front of the SNR, and partially cover it to produce the highly absorbed spectra around Region 3. There are other small molecular clouds around the CO arm. As seen in figure 5.20, an anti-correlation between the X-ray and ^{12} CO (1-0) surface brightness has been found by Sasaki et al. (2006), who utilized the superior angular resolution of the *Chandra* X-ray observatory.

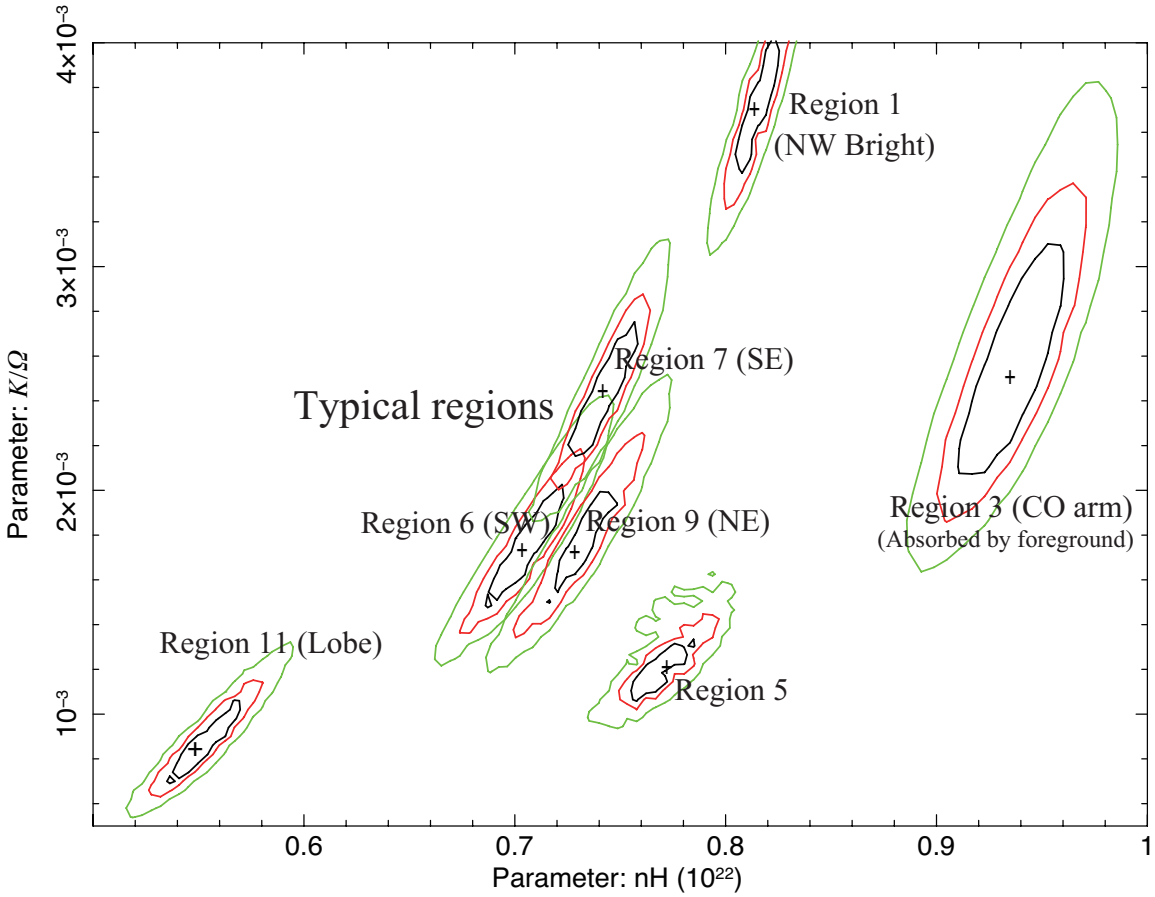

Figure 5.21: The confidence levels on the parameter space of the $N_{\rm H}$ and K_2/Ω. Black lines indicate confidential level of $\Delta\chi^2 = 2.3$, red 4.61, and green 9.21.

Global collision geometry

Taking the advantage of the higher sensitivity of *Suzaku* , which is suited for largely extended X-ray emission, we can study the global interaction geometry between the SNR and the main body of the GMC. As seen in figure 5.4 and 5.3, the SNR totally disappears just west of Region 5, presumably due to the GMC. Although the spectrum from Region 3 showed the excess absorption due to CO arm, that from Region 5 shows no such an excess absorption (table 5.6). In order to confirm that the $N_{\rm H}$ determination was not affected by some couplings among the parameters of the two-components (Plasma 1 and Plasma 2) model, we calculated confidence contours between $N_{\rm H}$ and K_1/Ω of Plasma 2 as shown in figure 5.21. It can be confirmed that Region 5 does not have excess absorption but small K_2/Ω.

Furthermore, in order to avoid a risk of missing fine spectral structures that may not be taken into account by the fitting models, in figure 5.22, we directly compared differences in the spectra between Regions 5 and 6. Compared with the spectrum of Region 1, that of Region 3 is indeed more absorbed towards softer energies. which demonstrates the effect of the foreground absorption. On the other hand, the spectra of Region 5 and 6 show no significant difference between each other except their surface brightness. Crossing the border from Region 6 to 5, the surface brightness thus decreased by half, without involving any change in foreground absorption. Thus, the faintness in Region 5 remains puzzling and cannot be explained by simple foreground absorption. The image further reveals three important

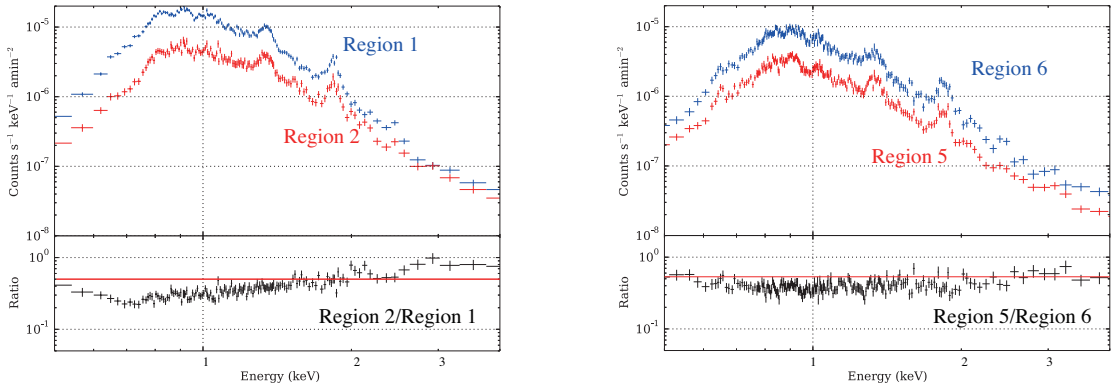

Figure 5.22: Direct comparison of two spectra. (left) The spectra of Region 1(blue) and 3(red), and their ratio (black) corrected for the emission area. and the bottom one is the ratio between them, where the difference in effective ares is corrected before dividing. (right) The same as the left one, but the spectra are chosen from Region 5 (red) and 6 (blue).

features.

1. The eastern rim of the GMC coincides with the stepwise brightness change in X-rays noticed in §5.3.5.

2. At the western edge of the X-ray emission, the IR surface brightness shows no peculiar feature.

3. Between (A) and (C), the X-ray and IR emissions co-exist.

To obtain more detail structure of the GMC, we employed the infrared (IR) data (by courtesy of Prof. H.Kaneda of Nagoya University) obtained by the *AKARI* observatory which is a Japanese IR satellite (Matsuhara et al., 2005). Figure 5.23 is the IR image, which cleanly visualize the interaction between CTB 109 and the GMC. To investigate the details, one-dimensional X-ray and IR profiles were derived from the 3 stripes labeled in figure 5.23 as (a), (b) and (c), and are shown in figure 5.24. The profile clearly reconfirm the above 3 features.

Considered all results, a possible geometry is that the collision is occurring at the western backside of the remnant as shown in figure 5.25. The reason why the absorption is not changing across the stepwise structure is that the GMC shove into the remnant and completely absorb all the X-ray emitted from the farther side of the SNR. Then, around line of sight (C), we can observe only the front side of the SNR which is not covered by the GMC. On the other hand, both forward and backward shell can be seen along the line of sight (A). For reference, Region 3 shows fewer number of X-ray photons due to the absorption, but a relatively high emission measure K (figure 5.21), possibly due to the interaction with the CO arm.

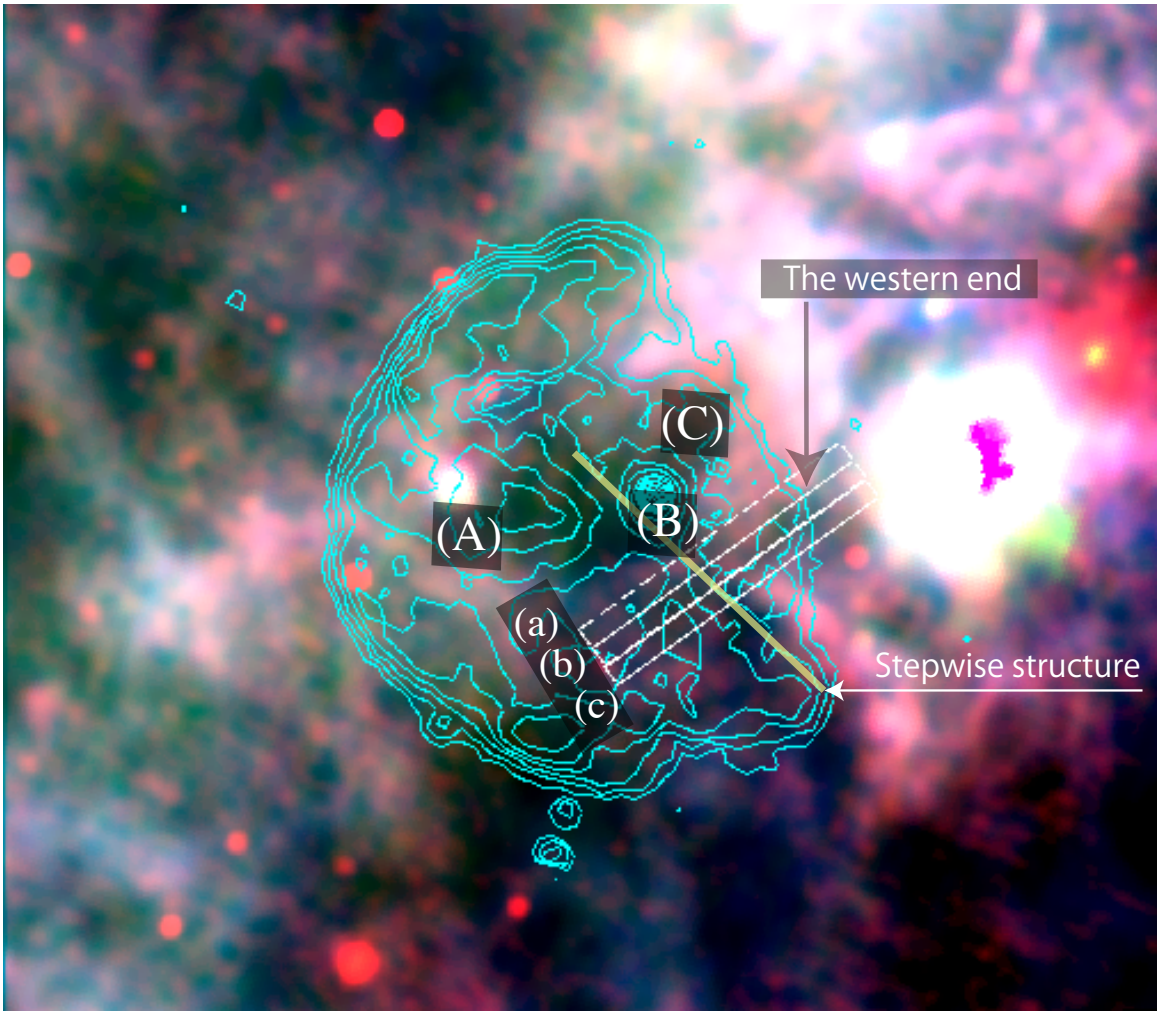

Figure 5.23: A composite false-RGB image of CTB 109 and its environment taken by *AKARI*. Red indicates the IR emission with wavelength 18 μm, green 90 μm, and blue 140 μm. Light blur contours indicate the X-ray surface brightness of CTB 109 taken by *ROSAT* . Three white rectangle boxes denoted as (a), (b) and (c) are the regions where the cross-sectional profile in figure 5.24 are extracted.

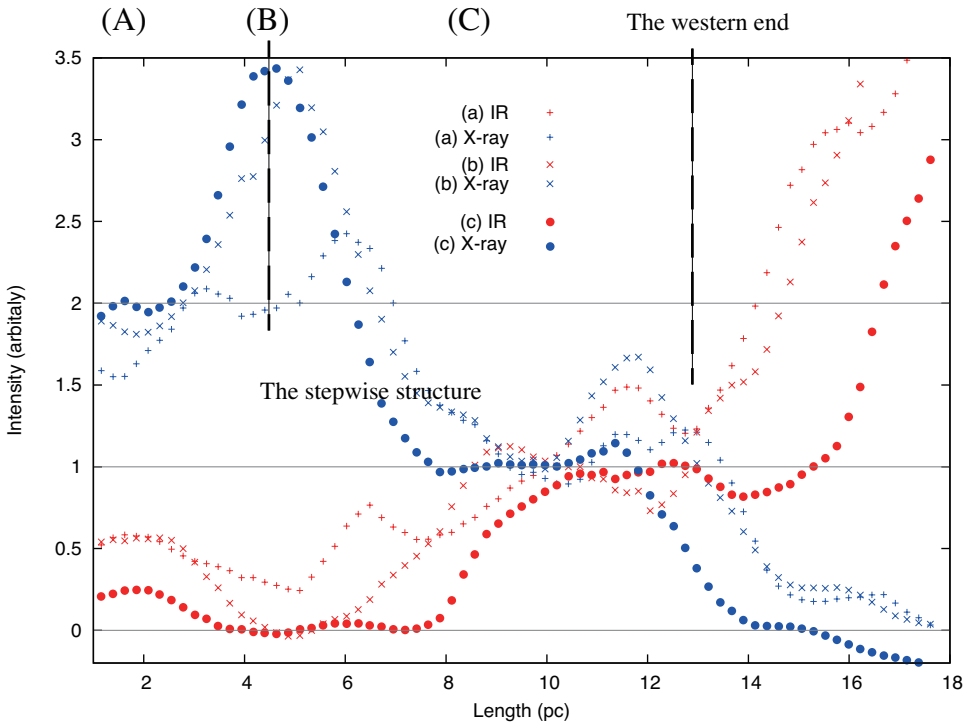

Figure 5.24: Cross-sectional profiles of the 0.2-1.5 keV X-ray emission (blue) and the 140 μm IR (red). The stripes used to derive these profiles are labeled as (a), (b) and (c) in figure 5.23. The profiles are also normalized to 1 around the cross over regions.

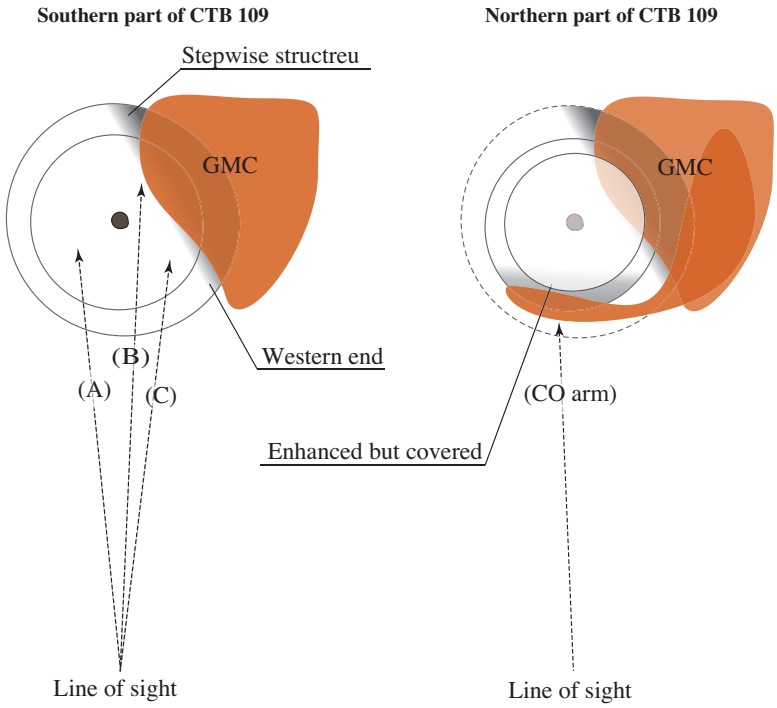

Figure 5.25: A schematic view of the geometrical relation of CTB 109 and the GMC, seen from north of the SNR. The left is a cut along the plane (east-west) while the right is a simple projection. The arrows labeled as (A), (B) and (C) describe the line of sight towards the three locations indicated in figure 5.23 and 5.24.

Chapter 6

Discussion

So far, we have studied the SNR CTB 109 hosting the magnetar 1E 2259+586. The SNR study revealed the existence of the two plasma components, and provided valuable information on their plasma condition, such as temperatures, ionization states, emission measures, and abundances of elements. These observables in turn allowed us to estimate basic quantities such as densities and total masses of the two plasmas, and the explosion energy. Now, it is time to construct a comprehensive view of the SN explosion which produced CTB 109 and 1E 2259+586, and to discuss possible formation scenario of magnetars. What does the SNR tell us about the formation of the magnetar ?

6.1 Estimation of the Progenitor Mass

One of our primary motivations has been to utilize X-ray observation of SNRs, to constrain progenitors and SN-explosions that produced non-rotation-powered NSs, especially magnetars representing them. The initial mass of a star is considered to play a major role of determining its fate and types of the compact remnant (a BH or an NS). Another quantity expected to affect the types of compact object, especially important for the types of NSs, is the initial rotation of the collapsing core. The faster the rotation, the larger mass can be sustained because of centrifugal force. Then, a rapidly rotating progenitor (even if it is very massive) is likely to leave an NS rather than a BH, and an NS produced under such a condition can be a magnetar due to an efficient dynamo provoked by rotation. The combination of such strong magnetic fields and rapid rotation is expected to make the SN explosion more energetic than ordinary cases. In this section, we examine our result against these views.

6.1.1 Results of the mass estimates

In Chapter 5, we arrived at a concrete view of the configuration and conditions of the two plasmas composing CTB 109 (figure 5.16): as shown in figure 5.17, the shell of the cooler plasma with a temperature of 0.24 keV (Plasma 2 = the heated ISM) encloses the hotter plasma (Plasma 1= the ejecta) with a temperature of 0.59 keV. From the obtained parameters including the emission measures (K_1 and K_2), we obtained our best estimate of the progenitor mass as $M_1 = 39 \pm 7\ (\eta_{\rm x}/0.8)\, d_{3.2}^{5/2}\ M_\odot$ (equation 5.15). This mass is apparently too large for the progenitor mass just prior to its final explosion; the core would then collapse into a BH. However, this is considered to represent the progenitors *initial* mass, because the

SNR is considered to have mostly caught up with, and taken over, the stellar winds from the progenitor which must have carried away a considerable fraction of the initial mass. This is because the stellar winds would not be able to flow farther than the GMC on the western side. Furthermore, if the stellar winds already escaped in the eastern half where the GMC are absent, we would have observed in table 5.6 much smaller emission measure in the eastern half than in the opposite side.

Then, how reliable is our mass estimate? To see this, we list up below various factors that can affect the results

1. Given parameters
   (a) distance: $D = 3.2 \pm 0.2\ d_{3.2}$ kpc
   (b) Angular Radius : $R = \theta_{\rm R} D$
2. X-ray spectral parameters (fittings)
   (a) temperatures: $kT_1 \sim 0.59$ keV and $kT_2 \sim 0.24$ keV
   (b) emission measure: K_1 and K_2
3. Secondary-derived parameters
   (a) Volume filling factors : f_1 and f_2
   (b) Averaged densities : n_1 and n_2
4. Assumptions
   (a) Plasma identification :
   Plasma 1 is the ejecta, and Plasma 2 is the swept-up matter
   (b) Volume calculation : $V_{\rm CTB} = 4/3\pi R^3 d_{3.2}^3 f_1 \eta_x$
   Spherical shell (partially broken)
   All the plasmas are X-ray visible (reverse shock reaching the center)
   (c) Pressure equilibrium : $n_1 kT_1 = n_2 kT_2$
   (d) Temperature equilibrium between heavy ions and electrons : $kT_{\rm e}/kT_{\rm P} = \epsilon \sim 1$
   (not included in mass estimation but related to age and energy estimations)
   (e) Solar abundances: $n_e/n_H = 1.2$

Among these possible sources of systematic errors, the most critical one is considered to be the distance uncertainty, because of the $d^{5/2}$ dependence. As reviewed in 5.17, the distance to CTB 109 has frequently been updated. While we have adopted the newest value of 3.2 kpc, the second newest estimate was 4.0 kpc by Tian et al. 2010. If we employed this, the mass estimate becomes considerably larger, $M_1 = 68 M_\odot$. Even though the impact is large, our conclusion on a massive progenitor is not changed.

Compared to this, the other uncertainties are considered less crucial, and some of them has already taken into account by the scaling factors of ϵ and η_x, like the $d_{3:2}$ renormalization. The uncertainty of the proton temperature, item (4.c), is indeed a difficult problem, especially in young SNRs with high

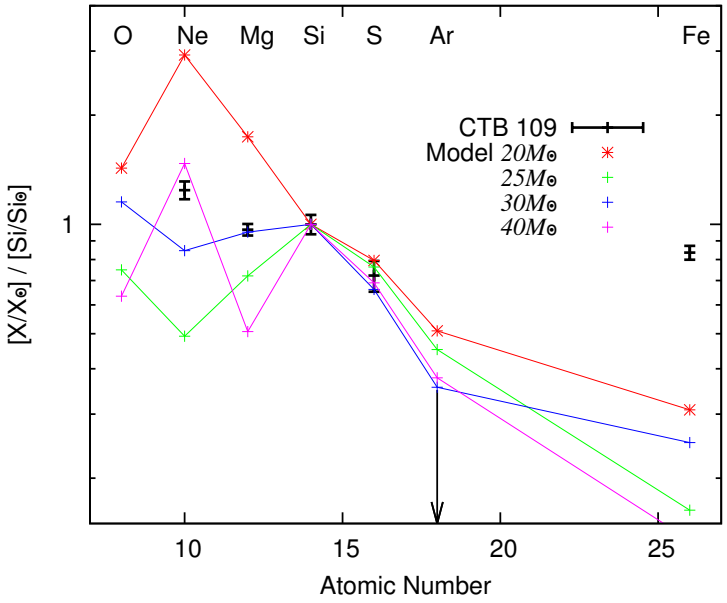

Figure 6.1: The measured abundance profile of CTB109 (black), compared with the theoretical predictions by Nomoto et al. (2006), calculated for a mass of 20 $M_\odot$ (red), 25 $M_\odot$ (green), 30 $M_\odot$ (blue), and 40 $M_\odot$ (magenta).

shock velocities as $>$ 1000 km s^{-1}. However, the ion and electron temperatures are considered to be rather close to each other, when the shock velocity is $<$ 500 km s^{-1} Ghavamian et al. (2007), which is fortunately the case with CTB 109. Thanks to the high quality data of the *Suzaku* XIS, the fitting errors are quite small, compared with the other uncertainties.

6.1.2 Elemental abundances

The amount of heavy elements synthesized in an SN explosion has been calculated by many theoreticians as a function of the progenitor mass. Figure 6.1 compares the abundance pattern of CTB 109 we measured, with a theoretical model calculation by Nomoto et al. (2006). Here, the measured pattern refers to the VNEI fit results, which measured the abundances of Plasma 1 to be identified with the ejecta. The measurements thus agree best with the case of M = 30 $M_\odot$ to 40 $M_\odot$. It is important that the most sensitive elements, Ne and Mg, were resolved clearly in our spectra (figure 5.6), thanks to the good energy resolution of the XIS. This comparison independently supports our conclusion that the magnetar 1E 2259+586 was produced by an SN explosion of a very massive star with $M \sim 39\ M_\odot$.

6.1.3 Comparison with previous work

Accumulating pieces of evidence suggest that magnetars are formed by rather massive progenitors. For example, Gaensler et al. (2005) argue that the magnetar AXP 1E 1048.1−5937 is possibly associated with a stellar wind bubble GSH 288.3-0.5-28, which was probably formed by the massive progenitor with 30–40 $M_\odot$. The most active magnetar SGR 1806-20 is associated with a young massive cluster with an age of 3.0-4.5 Myr, which may constrain the initial mass of the progenitor of this magnetar as $>$ 50 $M_\odot$ (Figer et al., 2005). Similarly, the magnetar CXO J164710.2−455216, located in a young massive star

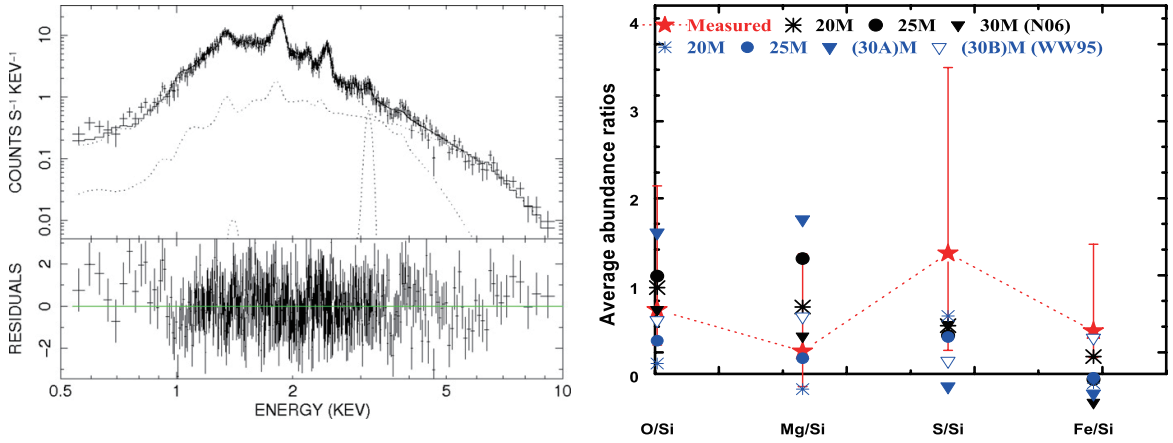

Figure 6.2: The spectrum and abundance profile of SNR Kes73 taken by *Xmm-Newton* (Kumar et al., 2014).

cluster Westerlund 1, is considered to have originated from a progenitor with a mass $> 40\ M_\odot$ (Muno et al., 2006). On the other hand, Davies et al. (2009) estimated the age of the star cluster Cl 1900+14, associated with the magnetar SGR 1900+14, and argued that its progenitor was less massive than the progenitors of $17 \pm 2\ M_\odot$.

Compared to the above quoted rather indirect methods, the mass estimates using the host SNRs, like ours, are considered to be more direct. For example, Kumar et al. (2014) conducted X-ray spectroscopic study of the SNR Kes 73 associated the magnetar 1E 1841−045. As shown in figure 6.2, they compared the measured abundance pattern of Kes 73 with some theoretical model calculation, and suggested that the progenitor of 1E 1841−045 was rather massive. However, their mass constraint remained rather poor. Our results, both from dynamics and abundances, are evaluated to be more constraining.

As already reviewed in §5.1.2, Sasaki et al. (2006, 2013, 2004) conducted a series of X-ray observations of CTB 109, using *XMM-Newton* and *Chandra*. From these observations, the progenitor of 1E 2259+586 was suggested to be $\sim 20\ M_\odot$. However, the *XMM-Newton* spectra of CTB 109 were explained by a single plasma component, and were unable to separate the ejecta emission. Although the Chandra observation distinguished the two plasma components, its FOV covered only a NW region of CTB 109. Compared to these, our results are considered to be considerably improving, because we covered the entire remnant, and the *Suzaku* XIS has a significantly better energy resolution than the similar instruments onboard *XMM-Newton* and *Chandra*.

6.1.4 Energetics of the SN explosion

Estimates of the progenitor mass, as carried out above, immediately enable us to calculate the explosion energies of the SNe, which are another important quantity when trying to understand the magnetar formation. This is because rapid rotation of the progenitor, invoked in the magnetar production (§6.1, Duncan & Thompson (1996)), is expected to make the explosion more energetic than other more typical NSs. In fact, if a newborn NS has a very short period as $P_0 = 3$ ms and an extremely strong initial field

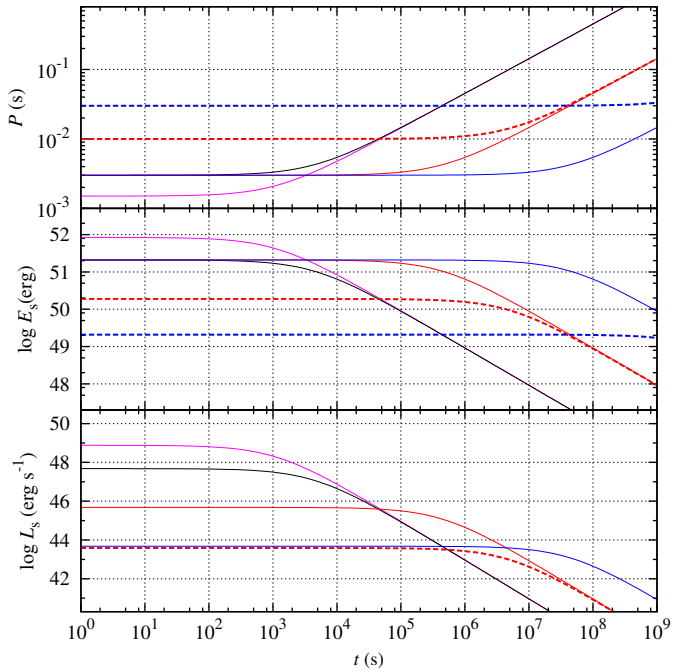

Figure 6.3: Examples of spin-down evolution of NSs with various conditions. The top panel shows the evolution of the period P, the second panel that of rotational energy $E_{\rm s}$, and the bottom panel spin-down luminosity $L_{\rm s}$. Black lines indicate an NS with dipole magnetic filed $B = 10^{15}$ G and initial spin period $P_0 = 3$ ms. Purple lines indicate the most energetic case as $B = 10^{15}$ and $P_0 = 1.5$ ms. Red and blue lines correspond to $B = 10^{14}$ G and $B = 10^{13}$ G, respectively, where solid and dotted lines means the initial spin period $P = 10$ ms and $P = 30$ ms. respectively.

as $B_0 = 10^{15}$ G, equation 3.6 predicts a huge magnetic spin-down luminosity as

$$\dot{E}(B, P) = \frac{B^2 R^6 \omega^4}{6c^3} = 5.3 \times 10^{47} \text{ ergs}^{-1} \, . \tag{6.1}$$

Since this value exceeds a typical observed luminosity of an SN (10^{41-45} erg s^{-1}), the remnant would be driven to become more energetic than other SNRs. More specifically, figure 6.3 shows spin-down evolution of NSs calculated simply by equation 6.1. Thus, such an NS is expected to release most of its rotational energy of 10^{51-52} erg in a very short time (a few hour a day) just after its birth. In other words, if magnetars originate from such rapidly rotating NSs, the associated SNRs would have considerably larger energies than other typical SNRs. The above idea was tested observationally by Vink & Kuiper (2006) and Vink (2008). However, they found no evidence for such excess energies in magnetar-hosting SNRs.

In §5.5.1, we estimated the explosion energy CTB 109 as $\sim 10^{51}$ erg. This is typical for a CC SNe, rather than unusually high. While this is consistent with Vink and Kuiper (2006) and Vink (2008), it is apparently inconsistent with the very high progenitor mass we derived. How can we reconcile these two results? In reality, we do not know details of the energy deposits from such radiations to ejecta or ambient medium. Normally, the initial magnetic dipole radiation has a very low frequency (e.g., 0.3 kHz if $P_0 = 3$ ms), which is lower than a typical plasma frequency in the ISM ($\sim$ 10 kHz), so that it would be unable to propagate, and apply outward force to accelerate the remnant. However, the exact interactions of such a low-frequency electromagnetic wave with the gaseous media is not well understood, because the radiation must have a huge electric field of which any perturbative treatment would be invalid. Hence, it is still an open issue how the postulated rapid initial spin down of a magnetar affects the SNR dynamics. Furthermore, the initial energization scenario assumes that the magnetic fields were much strong from the beginning. If magnetic field was instead generated by efficient dynamo as the NS gradually spin down, figure 6.3 would no longer be valid: the initial rotational energy would be released on a much longer time scale, and hence $\dot{E}$ of equation 6.1 would become lower.

6.2 Age Problem and Evolution of the Magnetic Field

Through the X-ray study of CTB 109, we successfully traced its evolution back to the beginning of the 1E 2259+586/CTB 109 system. As a result, the evolutionally history of CTB 109 has been described as shown in figure 5.19. The remaining issue is the evolution of the magnetar, especially solving the *Age problem*. As already mentioned in §5.1.3, the 1E 2259+586/CTB 109 system shows huge discrepancy in their age estimates. The characteristic age of 1E 2259+586 is given by equation 3.14 as

$$\tau_c = \frac{P}{(n-1)\dot{P}} = \frac{6.98 \text{ s}}{2 \times 4.84 \times 10^{-13} \text{ ss}^{-1}} = 230 \text{ kyr} \, , \tag{6.2}$$

where $n = 3$ is again the spin down index of dipole radiation (equation 3.6 and 3.10), while P and $\dot{P}$ are the spin period of NS and its derivative, respectively. This disagrees, by a factor of $\sim$ 18, with the host remnant age calculated in §5.5.2. Since this magnetar is located at the very center of the SNR, it is highly certain (as we have so far assumed) that the two objects were produced in the same SN explosion, instead of overlapping by chance. Then, the age discrepancy by a factor of $\sim$ 18 means that either of the two estimates, $\tau_{\rm snr}$ or τ_c, is wrong or highly biased. Since an SNR would not be able to shine for longer

than a few tens of kyr, the value of τ_c in equation 6.2 is more doubtful. Below, we assume that the true system age is close to τ_{snr}, and try to understand how τ_c has come to overestimate the true system age by this large amount.

6.2.1 Case with a Constant Magnetic Field

To solve the issue of the suggested overestimate of τ_c after Colpi et al. (2000) and DallOsso et al. (2012), let us begin with reviewing the meaning of τ_c. In general, the spin evolution of a pulsar with dipole surface magnetic field B is expressed empirically as

$$\frac{d\omega}{dt} = -bB^2\omega^n \tag{6.3}$$

with $b \equiv 32\pi^3 R_{psr}^6/3I\mu_0 c^3$ and the braking index of $n = 3$, where $R_{psr} = 10$ km is the pulsar's radius, $I = 9.5 \times 10^{44}$ g cm^2 its momentum of inertia, μ_0 vacuum permeability and c the light velocity. This is simply a re-writing of equation 3.10. If we use the pulse period $P = 2\pi/\omega$ and its derivative $\dot{P}$ instead of ω and $\dot{\omega}$, equation 6.3 becomes

$$B = \sqrt{\frac{P\dot{P}}{b}} \simeq 3.2 \times 10^{19} \sqrt{P\dot{P}}\ \mathrm{G}. \tag{6.4}$$

If B does not depend on time t, equation (6.3) can be integrated as

$$t = -\frac{1}{n-1}\left(\frac{\omega}{\dot{\omega}}\right)\left[1 - \left(\frac{\omega}{\omega_0}\right)^{n-1}\right] = \tau_c\left[1 - \left(\frac{\omega}{\omega_0}\right)^{n-1}\right] \tag{6.5}$$

where ω and $\dot{\omega}$ both refer to the present values, while ω_0 is the angular frequency at $t = 0$ (i.e. the birth). Assuming that $(\omega/\omega_0)^{n-1}$ can be neglected, the characteristic age is defined as

$$\tau_c \equiv \frac{\dot{\omega}}{(n-1)\,\omega} \equiv \frac{P}{(n-1)\,\dot{P}}. \tag{6.6}$$

These equations are generally used for pulsars.

More generally, from equation 6.5, the true age of the pulsar, denoted by t_0, can be compared with its τ_c as

$$\frac{\tau_c}{t_0} = \frac{1}{1 - \left(\frac{\omega}{\omega_0}\right)^{n-1}} = \frac{1}{1 - \left(\frac{P_0}{P}\right)^{n-1}} \simeq 1 + \left(\frac{P_0}{P}\right)^{n-1}, \tag{6.7}$$

where $P_0 = 2\pi/\omega_0$, and the last expression is the first-order approximation in $(P_0/P)^{n-1}$. Thus, τ_c becomes somewhat larger than t_0 if $(P_0/P)^{n-1}$ cannot be neglected. Conversely, if we somehow have an independent estimate of t_0, its comparison with τ_c can be used to infer P_0 as

$$P_0 = P\left(-\frac{t_0}{\tau_c} + 1\right)^{1/(n-1)}. \tag{6.8}$$

For example, the Crab pulsar (Staelin & Reifenstein, 1968), with $P = 33$ ms, $\dot{P} = 2.42 \times 10^{-13}$ ss^{-1} and $n = 2.509$ (Lyne et al., 1993), has $\tau_c = 1241$ yr. Comparing this with its true age of 960 yr (as of 2014), equation (6.8) yields $P_0 = 18$ ms if assuming $n = 2.509$ as observed, or $P_0 = 15.7$ ms if $n = 3.0$ (for ideal magnetic dipole radiation). Thus, regardless of the employed value of n, the small difference

between τ_c and t_0 of the Crab pulsar can be understood to imply that it has so far lost $\sim 3/4$ of its initial rotational energy in ~ 1 kyr.

In contrast to the above case of young active pulsars, we would need to invoke $P_0 = P \times 0.97 = 6.76$ s, if equation 6.8 with $n = 3$ were used to explain the large discrepancy, $\tau_c/t_0 \sim \tau_c/\tau_{snr} \sim 18$, found in the CTB/1E2259+586 system. This would lead to a view that 1E 2259+586 was born some 13 kyr ago as a slow rotator of which the spin period is much longer than those (0.2 s to 2 s) of the majority of *currently* observed (hence relatively old) radio pulsars, and has so far lost only a tiny fraction of its rotational energy in 13 kyr. However, such a view is opposite to a general consensus that new-born magnetars must be rotating rapidly, even faster than ordinary pulsars, in order for them to acquire the strong magnetic fields (Duncan & Thompson 1996). Furthermore, an NS with $P_0 = 6.67$ s, has an angular momentum of only $\sim 10^{-5}$ of those of typical new-born pulsars with $P_0 \sim 10$ ms including the Crab pulsar, and hence would require an extreme fine tuning in the progenitor-to-NS angular momentum transfer during the explosion. We therefore conclude that the age problem of 1E2259+586 cannot be solved as long as its magnetic field is assumed to have been constant since its birth.

6.2.2 Effect of the magnetic filed decay

Given the above result, we may next examine the case where B decays with time. In fact, the X-ray emission of magnetar is thought to arise when their magnetic energies are consumed (Thompson & Duncan, 1995). Then, the calculations presented in section 6.2.1 would be no longer valid, and we need to integrate equation 6.3 considering the time evolution of B. We assume a simple magnetic filed decay model employed by Colpi et al. (2000), namely

$$\frac{dB}{dt} = -aB^{1+\alpha}, \tag{6.9}$$

where $\alpha \geq 0$ is a parameter called *decay index*, and a is another positive constant. This equation can be solved as

$$B(t) = \begin{cases} \dfrac{B_0}{\left(1 + \dfrac{\alpha t}{\tau_d}\right)^{1/\alpha}} & (\alpha \neq 0) \\ \\ B_0 \exp\left(\dfrac{-t}{\tau_d}\right) & (\alpha = 0) \end{cases} \tag{6.10}$$

where B_0 represents the initial value of B, and $\tau_d = \left(1/aB_0^{\alpha}\right)$, an arbitrary constant, means a typical lead time till the power-law like decay of B begins.

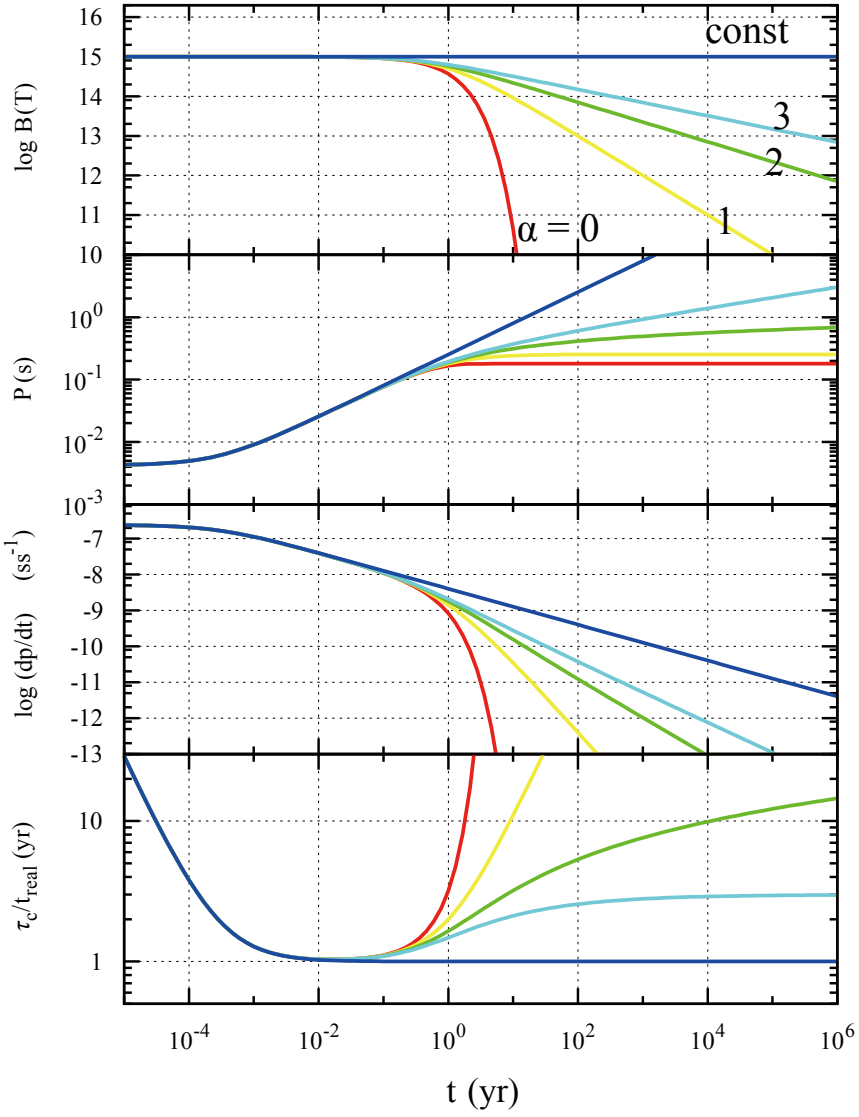

Figure 6.4: Some representative loci of spin and magnetic field evolutions assuming the field decay of equation 6.10. (Top) Examples of evolution tracks of magnetic fields. (Middle two panels) Evolution of of the pulse periods P and their derivatives $\dot{P}$. (Bottom) The overestimation factor of the characteristic age. The index α is chosen to be 3.0 (light-blue), 2.0 (green), 1.0 (yellow) and 0.0 (red). Non-decay model is represented by blue lines. In all cases τ_d is fixed to 1 yr.

Substituting equation 6.10 into equation 3.6, we can derive P as a function of t as

$$P(t)^{n-1} = P_0^{n-1} + bB_0^2 (n-1) (2\pi)^{n-1} \begin{cases} \dfrac{\tau_{\rm d}}{(2-\alpha)} \left[1 - \left(1 + \dfrac{\alpha t}{\tau_{\rm d}} \right)^{1-2/\alpha} \right] & (\alpha \neq 0, 2) \\ \dfrac{\tau_{\rm d}}{2} \left[1 - \exp\left(-\dfrac{t}{\tau_{\rm d}} \right) \right] & (\alpha = 0) \\ \dfrac{\tau_{\rm d}}{2} \ln\left(1 + \dfrac{2t}{\tau_{\rm d}} \right) & (\alpha = 2) \\ t & (B = \text{constant}) \, . \end{cases} \tag{6.11}$$

$\dot{P}$ is also derived as

$$\dot{P}(t, P) = bB_0^2 (n-1) (2\pi)^{n-1} P^{-(n-1)} \begin{cases} \left[1 + \dfrac{\alpha t}{\tau_{\rm d}} \right]^{-2/\alpha} & (\alpha \neq 0) \\ \exp\left(-\dfrac{2t}{\tau_{\rm d}} \right) & (\alpha = 0) \\ 1 & (B = \text{constant}) \, . \end{cases} \tag{6.12}$$

Then, as already given by DallOsso et al. (2012), $\tau_{\rm c}$ can be expressed as a function of t, P_0 , α and $\tau_{\rm d}$ as

$$\tau_{\rm c} = \begin{cases} \dfrac{\tau_{\rm d}}{2-\alpha} \left[\left\{ 1 + (2-\alpha) \dfrac{\tau_0}{\tau_{\rm d}} \right\} \left(1 + \dfrac{\alpha t}{\tau_{\rm d}} \right)^{2/\alpha} - \left(1 + \dfrac{\alpha t}{\tau_{\rm d}} \right) \right] & (\alpha \neq 0, 2) \\ \dfrac{\tau_{\rm d}}{2} \left[\left(1 + \dfrac{2\tau_0}{\tau_{\tau_{\rm d}}} \right) \exp\left(\dfrac{2t}{\tau_{\rm d}} \right) - 1 \right] & (\alpha = 0) \\ \left(1 + \dfrac{2t}{\tau_{\rm d}} \right) \left[\tau_0 + \dfrac{\tau_{\rm d}}{2} \ln\left(1 + \dfrac{2t}{\tau_{\rm d}} \right) \right] & (\alpha = 2) \end{cases} \tag{6.13}$$

where $\tau_0 \equiv P_0 / 2\dot{P}_0$ is the initial value of $\tau_{\rm c}$. The first form of equation 6.13 reduces to equation (3.14) for $\alpha \to \infty$ or $\tau_{\rm d} \to \infty$, i.e., the case of a constant B. Figure 6.4 illustrates the spin-down evolutions and the magnetic field decays with various α. Thus, we clearly confirm that $\tau_{\rm c}$, calculated in a simple minded way via equation 6.6, indeed become much larger than the true age. In other words, the object was spinning down in the past, when B was stronger, with a much higher rate than expected by a simple extrapolation from the present. Therefore, it took the object much shorter time to spin down from the initial P_0 to the present slow rotation.

When α is small as $\alpha < 1.0$, the filed is rapidly decaying, which causes extremely large overestimation, and $\tau_{\rm c}$ is growing with time. The critical point is $\alpha = 2.0$, and if α is smaller than it, P finally converges to a certain constant, in agreement with the fact that magnetars have a very clustered period, 2-11 sec. This means that $\dot{P}$ becomes progressively smaller and smaller, leading to a divergence of $\tau_{\rm c}$.

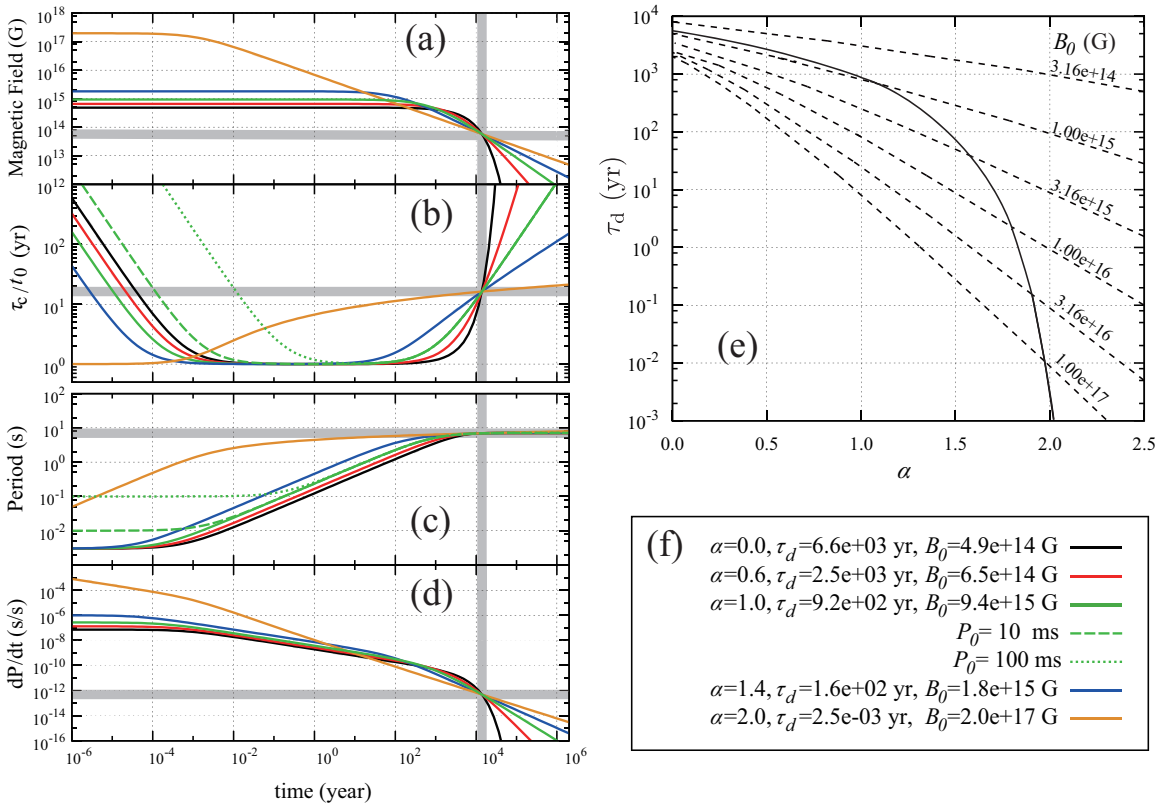

Figure 6.5: Possible evolution tracks of 1E 2259+586 assuming equation 6.3 and equation 6.9. Panels (a)-(d) represent the behavior of the magnetic field B, the over-estimation factor of the characteristic age (i.e., τ_c/t_0), the pulse period P, and its time derivative $\dot{P}$, respectively. The six representative tracks are all constrained to reproduce the presently measured P and $\dot{P}$ at t = 13 kyr. The dashed and dotted ones assume P_0 = 10 ms and 100 ms, respectively, while the other five all P_0 = 3 ms. Panel (e) shows the trajectory of solutions that can explain the present-day (t = 13 kyr) 1E 2259+586. Dashed lines indicate the initial filed value B_0. Panel (f) summarize the parameter sets of the trajectories.

6.2.3 Magnetic Field Evolution of 1E 2259+586

We have introduced the magnetic field decay model which can quantatively explain the characteristic age which becomes much longer than the actual age. Our next task is to examine whether the observed values of P and $\dot{P}$ of 1E 2259+586 can be explained with this picture. Equation 6.13 involves four free parameters, namely α, B_0 , τ_d and P_0, whereas we have only two observables, P and $\dot{P}$ at $t = t_0 \simeq$ 13 kyr. In §6.2.1, we showed that the effect of P_0 can be neglected, when the current P is long enough. Therefore, we chose to fix P_0 at 3 ms where strong dynamo works efficiently (e.g., Duncan & Thompson 1996).

With this presentation, let us search for a pair (B_0, τ_d) that can simultaneously explain P and $\dot{P}$ of 1E 2259+586 at present. Such solutions do exist, and figure 6.5 shows the behavior of such a family of solutions to equation 6.13. To visualize effects of P_0, solutions with $P_0 = 10, 100$ ms and $\alpha = 1.2$ are also shown in figure 6.5 [panels (b), (c), and (d)]. Thus, the effects of P_0 are limited to very early ($\ll 1$ s) stages of the evolution, and its value does not affect our discussion as long as it is much shorter than ~ 6.7 s. Is is nearly the same as figure 6.4, but the free parameters have been adjusted to reproduce the present P and $\dot{P}$ of 1E 2259+586, rather than specific at $t \rightarrow 0$ Below, we try to constrain the values of α (hence of B_0 and τ_d), assuming that α is not specific to 1E 2259+586 but relatively common among magnetars. This is because the broad-band X-ray spectra of magnetars are determined rather uniquely by τ_c (Enoto et al., 2010b), so that τ_c is considered to be tightly related to t_0 even if these two are unlikely to be identical: object-to-object scatter in α would cause a scatter in the τ_c/t_0 ratio, and would make the relation of Enoto et al. (2010b) difficult to interpret.

When α is small ($0 \leq \alpha < 0.5$), the field would decay, as seen in equation 6.13, either exponentially (if $\alpha = 0$) on a time scale of τ_d, or if $\alpha \neq 0$, with a relatively steep power-law after a long lead time $\tau_d \sim t_0$. The required initial field, $B_0 \sim 10^{15}$ G, is reasonable. However, the implied view would be rather ad-hoc: 1E 2259+586 had been relatively inactive until recently, when it suddenly started to release its magnetic energy with a high rate. Furthermore, if such a small value of α were common to magnetars, their age differences would make, as in figure 6.5 (a), their present-day field distribution scatter much more widely than is observed. Hence we regard these small values of α unlikely.

As α increases towards 2.0, the power-law field decay becomes milder, with shorter values of τ_d and stronger initial fields B_0. The implication is that the object started releasing its magnetic energy rather soon after the birth, and had already dumped away a large fraction of its rotational energy at a very early stage when the field was still very strong. As seen in figure 6.5 (c), the spin period has almost converged to its terminal value (see also DallOsso et al. 2012). Therefore, as touched on in §6.2.2, this case can explain the observed narrow scatter in P of magnetars, assuming that they share relatively similar values of α and B_0. However, the cases with $\alpha \sim 2.0$ or larger would require too strong initial fields, e.g., $B_0 \sim 10^{17}$ G, which would be much higher than the strongest dipole field observed from magnetars, $B = 2.4 \times 10^{15}$ G of SGR 1806−20 (Nakagawa et al. 2009). Therefore, such large-α solutions are unlikely, too.

To summarize these examinations, figure 6.5(e) shows the locus of the allowed solutions on the (α, τ_d) plane, where the values of B_0 are also indicated. We thus reconfirm the above considerations, that the range of $1 \lesssim \alpha < 2$ is appropriate, in agreement with the suggestion by DallOsso et al. (2012). In §6.3.1, we try further constraining α by considering other magnetar/SNR pairs.

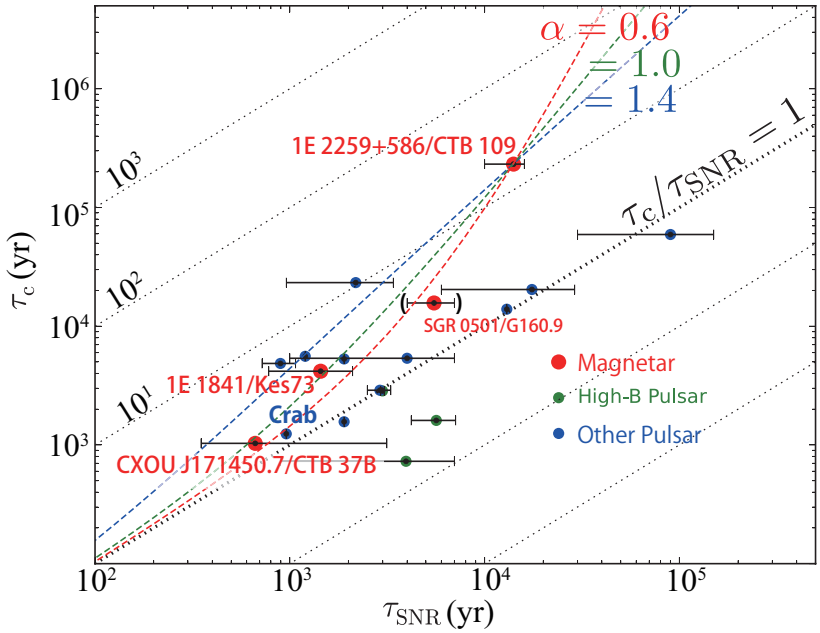

Figure 6.6: Relations between τ_{snr} and τ_c of single NSs associated with SNRs. Red, magenta and blue represent magnetars, high-B pulsars and rotation powered pulsars, respectively. Parameters are listed in table 6.1. The SGR 0501+4516/G160.9+2.6 pair is parenthesized, because the association is rather doubtful, and this SNR might be associated to another pulsar PSR B0458+46 (e.g., Leahy & Roger 1991). The red, green, and blue dashed curves indicate solutions to equation 6.13, with $(\alpha, \tau_d, B_0) = (0.6, 2.5 \times 10^3$ yr, 6.5×10^{14} G), (1.0, 9.2×10^2 yr, 9.4×10^{15} G) and (1.4, 1.6×10^2 yr, 1.8×10^{15} G), respectively. They all assume $P_0 = 3$ ms, and B_0 which is specified by figure 6.5 (e).

6.3 The Magnetar in Comparison with Other NSs

We reconfirmed the age problem of 1E 2259+586 and CTB 109 in §5, and presented a way to solve it with a simple magnetic field decay model. The result agrees with the basic concept of magnetar hypothesis which implies that the energies stored by their magnetic fields should be consumed to supply their X-ray luminosities exceeding those available with their spin down. The amount of released field energies can be reflected in the overestimations of the characteristic ages. Our final step is to examine whether the concept magnetic field decay applies more generally to magnetars, or even more widely to magnetars, or even more widely to other population of NSs. This examination will allow us to evaluate to thaw range own results have an impact in the understanding of NSs as whole.

6.3.1 Comparison with other NSs

To compare our results with other NS/SNR associations including magnetar/SNR systems, figure 6.6 shows relations between τ_c of such single pulsars and the ages of their host SNRs. Data points of rotation-powered pulsars are distributed around the line representing $\tau_c/\tau_{SNR} = 1$ with a few exceptions (e.g., Torii et al. 1999 for J1811−1925/G11.2−0.3). Therefore, rotation-powered pulsars, including the particular case of the Crab pulsar, are considered to be free from the age problem.

This further implies that the magnetic fields of $B \sim 10^{12}$ G NSs may not decay significantly, in agreement with the same conclusion derived by Makishima et al. (1999) from accreting binary X-ray pulsars having $B \sim 10^{12}$ G. In addition to the ordinary pulsars, figure 6.6 shows a few other magnetar/SNR associations. The magnetar CXOU J171405.7-381031 has a very small characteristic age of 0.96 kyr (Sato et al., 2010), which is consistent, within rather large errors, with the age ($0.65^{+2.5}_{-0.3}$ kyr; Nakamura et al. 2009) of the associated SNR, CTB 37B. Another magnetar/SNR association, 1E 1841-045/Kes73, is located in figure 6.6 between J171405.7-381031/CTB 37B and 1E 2259+586/CTB 109. The age of Kes73 was estimated by Kumar et al. (2014), as $0.75 - 2.1$ kyr (table 6.1). Combining this with $\tau_c = 4.7$ kyr of 1E 1841-045 (table 6.1), the age discrepancy of this pair becomes $\tau_c/\tau_{SNR} = 2.7-8$. Thus, the three magnetar/SNR associations (including 1E 2259+586/CTB 109) suggest that the age overestimation factor, τ_c/τ_{SNR}, increases towards older objects. This agrees, at least qualitatively, with the theoretical behavior seen in figure 6.5 (c), assuming P_0 is negligible.

We hence tried to explain the data points of these three magnetar/SNR associations with a common set of parameters, and derive a plausible range of α. For this purpose, three evolution tracks representing the solutions to equation 6.13 for 1E 12259+586/CTB 109 are additionally plotted on figure 6.6. Each parameter set is the same as that of figure 6.5 (f). If α is smaller than 0.6 (dashed red line), the CXOU J171405.7-381031/CTB 37B association cannot be explained. On the other hand, large value of $\alpha(> 1.5)$ fail to explain the 1E 1841-045/Kes73 association.

Thus, the three magnetar/SNR pairs in figure 6.6 can be explained in a unified way if they have a common value of α (and also of τ_d) that may be in the range of $0.6 < \alpha < 1.4$. Although the constraint on α is somewhat loose, the magnetar hypothesis requires the fields decays of NSs to explain their X-ray luminosity. Therefore, the systematic overestimation of the characteristic ages of magnetars is inherent to their interpretation as magnetically-driven objects.

6.3.2 On the P-$\dot{P}$ diagram

The evolution tracks of P and $\dot{P}$ in figure 6.5 can be interpreted in the P-$\dot{P}$ diagram. Figure 6.7 reproduces figure 3.2, where superposed is the evolution tracks with $\alpha = 1$. When α is smaller than 2, P described in equation 6.11 thus converges to a constant value in a finite time. Employing $n = 3$, the converged value of P_∞ is given as

$$P_\infty = 2\pi \sqrt{\frac{2b}{a\,(2-\alpha)}}\, B_0^{1-\frac{\alpha}{2}} \,. \tag{6.14}$$

As seen in figure 6.7, this P_∞ well explains the fact that P of all known magnetars are distributed in 2-12 s, and no magnetar with $P > 12$ s is found.

Recently, three low-B magnetars, including SGR 0418+5729 (Rea et al., 2013), Swift J1822.31606 (Rea et al. 2012) and 3XMM J185246.6+003317 (Zhou et al., 2014), have been discovered. They show sporadic outbursts like other magnetars, while their dipole magnetic field are weaker than the quantum limit of $B_{qed} = 4.4 \times 10^{13}$ G (§3.3) as seen in figure 6.7. The low-B magnetars are considered to be formed with $B_0 \sim 10^{15}$ G and to have already consumed most of the field energies. Thus, they will no longer spin down by the dipole magnetic braking, but may exhibit activities possibly using their internal magnetic fields (Tiengo et al., 2013).

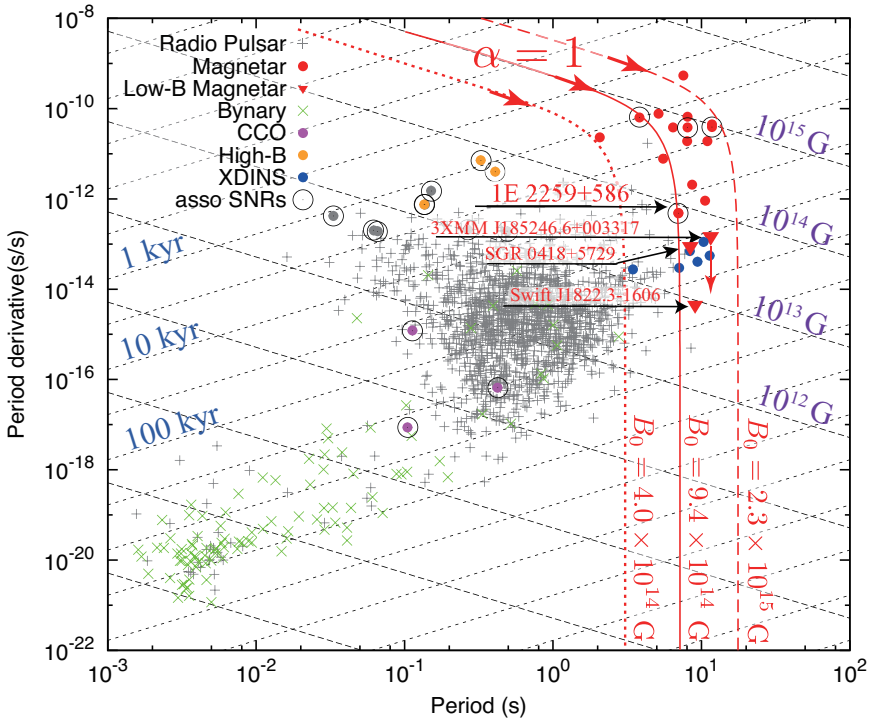

Figure 6.7: The same as figure 3.2 (P-$\dot{P}$ diagram), but the evolution tracks of P and $\dot{P}$ with $\alpha = 1$ are shown. Solid red line is a solution for 1E 2259+586 and CTB 109. Dashed and dotted red lines show different B_0.

6.3.3 Spatial distributions of magnetars and other NSs

The scenario so far developed implies that magnetars form a population that is much younger than previously thought. Is this conclusion supported by any other independent evidence ? Figure 6.8 shows a spatial distribution of NSs including magnetars. It can provides another way to compare magnetars with other NSs on much longer time scales than figure 6.6. Because of steady motions after kick velocities are given by explosions, older pulsars with larger τ_c are thus distributed up to farther distances from the Galactic plane, as seen in the panel (a) in figure 6.8. In contrast, magnetars are much more concentrated to the plane for their nominal characteristic ages, as better seen in figure 6.8 (b) which is a projection of figure 6.8 (a) along the direction perpendicular to the Galactic plane.

The difference in figure 6.8 implies two possible scenarios; magnetars are much younger than indicated by their τ_c, or their kick velocities are systematically lower than those of other NSs. Recently, proper motions of four magnetars (SGR 1806−20, SGR 1900+14, 1E 2259+586 and 4U 0142+61) were successfully measured by Tendulkar et al. (2012, 2013). They calculated the mean and standard deviation of their ejection velocities as 200 km s^{-1} and 90 km s^{-1}, respectively. They also conclude that the weighted average velocity of magnetars is in good agreement with the tangential velocities of the pulsar population (Hobbs et al., 2005). Therefore, we are left with the former of the two possibilities. In other words, magnetars should be systematically younger than ordinary pulsars that have similar τ_c. This notion gives us a chance to reconsider the population of NSs. Magnetars already occupy the most of younger NS population as seen in figure 6.8 (c) which is a projection of figure 6.8 (a) along the direction parallel to the Galactic plane.

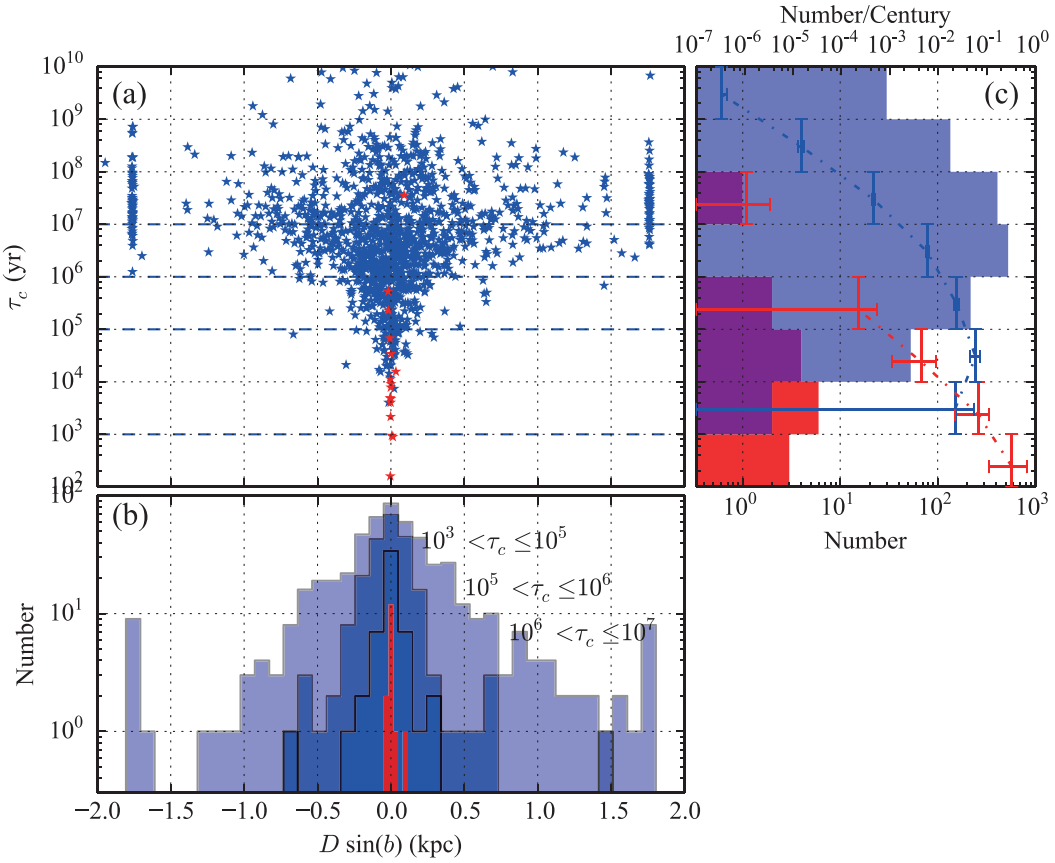

Figure 6.8: (a) Spatial distributions of magnetars (red) and radio pulsars (blue). Horizontal and vertical axises mean distance from the Galactic plane (= D sin(b)) and characteristic age, respectively. (b) Projection of panel (a) onto the direction perpendicular to the Galactic plane. Radio pulsars are divided into three subgroups according to their age. (c) Age distributions of the objects, produced by projecting panel (a) onto the time axis. Histograms represent numbers of pulsars with ages in that logarithmic interval, while crosses tied by a dotted line show the object number per century.

6.3.4 Impacts of the present results

Based on the *Suzaku* results and other considerations, we have developed the concept of magnetic field decay in magnetars. It is expected to give impacts to our our understanding of NSs in the following aspects.

1. Our view has successfully solved, on the grounds of basic physics without any ad-hoc assumptions, the age problem in the 1E 2259+586/CTB 109 system which used to be a considerable nuisance.

2. The result gives an independent support to the basic postulate of magnetars, that they are radiating by a release of their magnetic energies. Conversely, the age problem is an intrinsic consequence of magnetars as magnetically-driven NSs.

3. The result implies that magnetar activity lasts for a much shorter time than thought previously. Therefore, as shown in figure 6.8 (c), magnetars must be born with comparable, or even higher, rates than ordinary pulsars. This raises a novel possibility that a significant fraction of NSs are in fact born as magnetars, rather than the $B \sim 10 - 12$ objects which were so far considered "standard.

4. The suggested high birth rate of magnetars is consistent with the fact that CTB 109 is similar, in their metal abundances and explosion energy, to average core-collapse SNRs.

5. There must be a large population of aged or dead magnetars, which already spent up their magnetic energies. Some of them might be hidden among mass accreting binary X-ray pulsars (Sasano 2014).

Table 6.1: Parameters for Figure 6.6.

#	Pulsar/SNR	P (ms)	$\dot{P}$ (ss^{-1})	B ($\times 10^{12}$ G)	τ_c (kyr)	τ_{SNR} (kyr)
1	1E 1841-045/Kes73	11778	4.5×10^{-11}	730	4	0.75 - 2.1
2	SGR 0501+4516/G160.9+2.6	5762	5.8×10^{-12}	190	16	4 - 7
3	J171405.7-381031/CTB37B	3824	5.9×10^{-11}	480	0.96	$0.65^{+25}_{-0.3}$
4	1E 2259+586/CTB 109	6979	4.8×10^{-13}	58	230	10 - 16
5	J1846-0258/Kes75	326	7.1×10^{-12}	49	0.7	0.9 - 4.3
6	J1119-6127/G292.2-0.5	407	4.0×10^{-12}	41	1.6	4.2 - 7.1
7	J1124-5916/G292.0+1.8	135	7.5×10^{-13}	10	2.9	2.93 - 3.05
8	J1513-5908/G320.4-1.2	151	1.5×10^{-12}	15	1.6	1.9
9	J0007+7303/G119.5+10.2	315	3.6×10^{-13}	11	14	13
10	J1930+1852/G54.1+0.3	136	7.5×10^{-13}	10	2.9	2.5 - 3.3
11	J1856+0113/W44	267	2.1×10^{-13}	7.5	20	6 - 29
12	J0633+0632/G205.5+0.5	297	8.0×10^{-14}	4.9	60	30 - 150
13	Crab	33	4.2×10^{-13}	3.8	1.2	0.959
14	J0205+6449/3C 58	65	1.9×10^{-13}	3.6	5	1-7
15	J1833-1034/G21.5-0.9	61	2.0×10^{-13}	3.6	5	0.72 - 1.07
16	J1747-2809/G0.9+0.1	52	1.6×10^{-13}	2.9	5	1.9
17	J1813-1749/G12.8-0.0	44	1.3×10^{-13}	2.4	6	1.2
18	J1811-1925/G11.2-0.3	64	4.4×10^{-14}	1.7	2.3	0.96 - 3.4

Data for P and $\dot{P}$ of pulsar were collected from ATNF Pulsar catalogue (Manchester et al., 2005)[1]
Data for τ_{SNR} were collected from Ferrand & Safi-Harb (2012) [2]

Chapter 7

Conclusion

In the present thesis, we analyzed Suzaku data of the SNR CTB 109 hosting the magnetar 1E 2259+586, mainly to clarify the birth conditions of highly magnetized NSs. The derived results can be summarized in the following 6 points.

1. We reconfirmed that CTB 109 consists of two plasma components with different temperature of 0.24 keV and 0.59 keV, (§5.2.4), The plasma with lower temperature is identified as the shock-heated ambient medium, while that with higher temperature is considered to be the ejecta from the progenitor (§5.4.3). The SNR is in the Sedov-adiabatic phase, expanding with a velocity of 450 km s^{-1}, and the reverse shock has reached the center.

2. Although CTB 109 lacks its western half where molecular clouds are present, no evidence of increased absorption was detected from the western SNR edge. Therefore, the peculiar half-moon shape of CTB 109 is not due to obscuration by molecular clouds that are in foreground. Instead, we successfully explained the SNR morphology by presuming that the molecular clouds collided with the SNR from western backside, and obstructed its further expansion.

3. The initial mass of the progenitor and explosion are estimated as $39 \pm 7\ M_{\odot}$ and 0.7×10^{51} erg, respectively (§5.5.1). The abundance pattern of the ejecta, when compared with theoretical predictions, supports the mass estimate (§6.1.2). While the estimated explosion energy is quite normal as a CC SN, derived mass agree with some theoretical works predicting that magnetars should be produce by rather massive stars.

4. Considering explosion dynamics, we estimated the age of CTB 109 as 13 kyr, which is supported by independently by considering the evolution of plasma ionization age in an expanding volume. Since this SNR age is much younger than the characteristic age of 1E 2259+586, we reconfirmed the age problem.

5. Employing the power-raw like magnetic decay model, we successfully ascribed the age discrepancy to a systematic overestimation of the characteristic age of 1E 2259+586 (§5.1.3). This age overestimation also applies to other SNR-hosted magnetars. This view is also supported by a difference between magnetars and other pulsars in their galactic latitude distributions.

6. We conclude that the magnetic field decay of magnetars has made them appear much older than their real age. In other words, magnetars are much younger population than so far thought. This further implies that a considerable fraction of NSs are born as magnetars.

These results give one of the first observational elucidations of the birth conditions of magnetars. At the same time, they are expected to innovate our understanding of NSs, because those with $\sim 10^{12}$ G magnetic fields may no longer be considered as a prototype of young NSs.

These results imply that magnetars are more frequently prodded by SN, which are expected to give a high impact on the population study of NSs, especially new born NSs in SN explosions.

Bibliography

Alpar, M. A., Ertan, U., & ÇalÅkan, c. 2011, The Astrophysical Journal, 732, L4

Anders, E. & Grevesse, N. 1989, Geochimica et Cosmochimica Acta, 53, 197

Archibald, R. F., Kaspi, V. M., Ng, C.-Y., et al. 2013, Nature, 497, 591

Balucinska-Church, M. & McCammon, D. 1992, The Astrophysical Journal, 400, 699

Baykal, A., Swank, J. H., Strohmayer, T., & Stark, M. J. 1998, Astronomy and Astrophysics

Bignami, G. F., Caraveo, P. A., De Luca, A., & Mereghetti, S. 2003, Nature, 423, 725

Blondin, J. M., Wright, E. B., Borkowski, K. J., & Reynolds, S. P. 1998, The Astrophysical Journal, 500, 342

Bocchino, F., Maggio, A., & Sciortino, S. 1999, Astronomy and Astrophysics

Carlini, A. & Treves, A. 1989, Astronomy and Astrophysics (ISSN 0004-6361), 215, 283

Castro, D., Slane, P., Ellison, D. C., & Patnaude, D. J. 2012, The Astrophysical Journal, 756, 88

Chevalier, R. A. 1974, The Astrophysical Journal, 188, 501

Chevalier, R. A. 1977, Annual Review of Astronomy and Astrophysics, 15, 175

Chevalier, R. A. 1982, The Astrophysical Journal, 258, 790

Cline, T. L., Desai, U. D., Pizzichini, G., et al. 1980, The Astrophysical Journal, 237, L1

Coe, c. & Jones, c. 1992, Monthly Notices of the Royal Astronomical Society (ISSN 0035-8711), 259, 191

Coe, c., Jones, c., & Lehto, c. 1994, Monthly Notices of the Royal Astronomical Society, 270

Colpi, M., Geppert, U., & Page, D. 2000, The Astrophysical Journal, 529, L29

Corbet, R. H. D., Smale, A. P., Ozaki, M., Koyama, K., & Iwasawa, K. 1995, The Astrophysical Journal, 443, 786

DallOsso, S., Granot, J., & Piran, T. 2012, Monthly Notices of the Royal Astronomical Society, 422, 2878

Davies, B., Figer, D. F., Kudritzki, R.-P., et al. 2009, The Astrophysical Journal, 707, 844

Davies, c., Coe, c., Payne, c., & Hanson, c. 1989, Monthly Notices of the Royal Astronomical Society (ISSN 0035-8711), 237, 973

den Hartog, P. R., Kuiper, L., & Hermsen, W. 2008, Astronomy and Astrophysics, 489, 263

Dib, R. & Kaspi, V. M. 2014, The Astrophysical Journal, 784, 37

Duncan, R. C. & Thompson, C. 1992, The Astrophysical Journal, 392, L9

Duncan, R. C. & Thompson, C. 1996, in AIP Conference Proceedings, Vol. 366 (AIP), 111–117

Enoto, T., Nakazawa, K., Makishima, K., et al. 2010a, The Astrophysical Journal, 722, L162

Enoto, T., Nakazawa, K., Makishima, K., et al. 2010b, The Astrophysical Journal, 722, L162

Fahlman, G. G. & Gregory, P. C. 1983, IN: Supernova remnants and their X-ray emission; Proceedings of the Symposium, 445

Fahlman, G. G., Gregory, P. C., Middleditch, J., Hickson, P., & Richer, H. B. 1982, The Astrophysical Journal, 261, L1
Ferrand, G. & Safi-Harb, S. 2012, Advances in Space Research, 49, 1313
Figer, D. F., Najarro, F., Geballe, T. R., Blum, R. D., & Kudritzki, R. P. 2005, The Astrophysical Journal, 622, L49
Gaensler, B. M., McClure-Griffiths, N. M., Oey, M. S., et al. 2005, The Astrophysical Journal, 620, L95
Gaunt, J. A. 1930, Philosophical Transactions of the Royal Society A: Mathematical, Physical and Engineering Sciences, 229, 163
Gavriil, F. P. 2004, in AIP Conference Proceedings, Vol. 714 (AIP), 302–305
Ghavamian, P., Laming, J. M., & Rakowski, C. E. 2007, The Astrophysical Journal, 654, L69
Gibson, S. J., Taylor, A. R., Higgs, L. A., Brunt, C. M., & Dewdney, P. E. 2005a, The Astrophysical Journal, 626, 195
Gibson, S. J., Taylor, A. R., Higgs, L. A., Brunt, C. M., & Dewdney, P. E. 2005b, The Astrophysical Journal, 626, 214
Goldreich, P. & Julian, W. H. 1969, The Astrophysical Journal, 157, 869
Gotthelf, E. V. & Halpern, J. P. 2009, The Astrophysical Journal, 695, L35
Gotthelf, E. V., Halpern, J. P., & Alford, J. 2013, The Astrophysical Journal, 765, 58
Gregory, P. C. & Fahlman, G. G. 1980, Nature, 287, 805
Haberl, F. 2005, EPIC-XMM-Newton Consortium Meeting - 5 years of Science with XMM-Newton : Proceedings of the 2005 EPIC XMM-Newton Consortium Meeting
Haberl, F., Schwope, A. D., Hambaryan, V., Hasinger, G., & Motch, C. 2003, Astronomy and Astrophysics, 403, L19
Halpern, J. P. & Gotthelf, E. V. 2010, The Astrophysical Journal, 709, 436
Halpern, J. P. & Gotthelf, E. V. 2011, The Astrophysical Journal, 733, L28
Hanson, c., Dennerl, c., Coe, c., & Davis, c. 1988, Astronomy and Astrophysics (ISSN 0004-6361), 195, 114
Heinke, C. O. & Ho, W. C. G. 2010, The Astrophysical Journal, 719, L167
Hessels, J. W. T., Ransom, S. M., Stairs, I. H., et al. 2006, Science (New York, N.Y.), 311, 1901
Hewish, A., Bell, S. J., Pilkington, J. D. H., Scott, P. F., & Collins, R. A. 1968, Nature, 217, 709
Heydari-Malayeri, M., Kahane, C., & Lucas, R. 1981, Nature, 293, 549
Heyl, J. S. & Hernquist, L. 1999, Monthly Notices of the Royal Astronomical Society, 304, L37
Hobbs, G., Lorimer, D. R., Lyne, A. G., & Kramer, M. 2005, Monthly Notices of the Royal Astronomical Society, 360, 974
Hobbs, G., Manchester, R., Teoh, A., & Hobbs, M. 2004, Young Neutron Stars and Their Environments
Hughes, V. A., Harten, R. H., Costain, C. H., Nelson, L. A., & Viner, M. R. 1984, The Astrophysical Journal, 283, 147
Hughes, V. A., Harten, R. H., & van den Bergh, S. 1981, The Astrophysical Journal, 246, L127
Hulleman, c., vanKerkwijk, c., Verbunt, c., & Kulkarni, c. 2000, Astronomy and Astrophysics
Hummer, D. G. 1988, The Astrophysical Journal, 327, 477
Hurford, A. P. & Fesen, R. A. 1995, Monthly Notices of the Royal Astronomical Society, 277, 549
Hurley, K., Li, P., Kouveliotou, C., et al. 1999, The Astrophysical Journal, 510, L111
Igoshev, A. P. & Popov, S. B. 2013, Monthly Notices of the Royal Astronomical Society, 432, 967
Ikebe, Y., Makishima, K., Fukazawa, Y., et al. 1999, The Astrophysical Journal, 525, 58

Ishisaki, Y., Maeda, Y., Fujimoto, R., et al. 2007, Publications of the Astronomical Society of Japan
Israel, G. L., Esposito, P., Rea, N., et al. 2010, Monthly Notices of the Royal Astronomical Society, 408, 1387
Israel, G. L., Mereghetti, S., & Stella, L. 1994, The Astrophysical Journal, 433, L25
Ivanenko, D. D. & Kurdgelaidze, D. F. 1967, Astrophysics, 1, 251
Iwasawa, K., Koyama, K., & Halpern, J. P. 1992, PASJ: Publications of the Astronomical Society of Japan (ISSN 0004-6264), 44, 9
Kaastra, J. S. & Jansen, F. A. 1993, Astronomy and Astrophysics Supplement Series (ISSN 0365-0138), 97, 873
Karzas, W. J. & Latter, R. 1961, The Astrophysical Journal Supplement Series, 6, 167
Kaspi, c., Gavriil, c., & Woods, c. 2002, The Astronomer's Telegram
Kaspi, V. M., Chakrabarty, D., & Steinberger, J. 1999, The Astrophysical Journal, 525, L33
Kellogg, E., Baldwin, J. R., & Koch, D. 1975, The Astrophysical Journal, 199, 299
Kothes, R. & Foster, T. 2012, The Astrophysical Journal, 746, L4
Kothes, R., Uyaniker, B., & Yar, A. 2002, The Astrophysical Journal, 576, 169
Koyama, K., Hoshi, R., & Nagase, F. 1987, Astronomical Society of Japan, 39, 801
Koyama, K., Nagase, F., Ogawara, Y., et al. 1989, Astronomical Society of Japan, 41, 461
Koyama, K., Tsunemi, H., Dotani, T., et al. 2007, Publications of the Astronomical Society of Japan
Kumar, H. S., Safi-Harb, S., Slane, P. O., & Gotthelf, E. V. 2014, The Astrophysical Journal, 781, 41
Leahy, D. A. & Roger, R. S. 1991, The Astronomical Journal, 101, 1033
Lee, S.-H., Patnaude, D. J., Ellison, D. C., Nagataki, S., & Slane, P. O. 2014, The Astrophysical Journal, 791, 97
Lyne, A. G., Pritchard, R. S., & Graham-Smith, F. 1993, Monthly Notices of the Royal Astronomical Society, 265
Makishima, K., Mihara, T., Nagase, F., & Tanaka, Y. 1999, The Astrophysical Journal, 525, 978
Manchester, R. N., Hobbs, G. B., Teoh, A., & Hobbs, M. 2005, The Astronomical Journal, 129, 1993
Marcaide, J. M., Alberdi, A., Ros, E., et al. 1997, The Astrophysical Journal, 486, L31
Marcaide, J. M., Martí-Vidal, I., Alberdi, A., et al. 2009, Astronomy and Astrophysics, 505, 927
Martí-Vidal, I., Marcaide, J. M., Alberdi, A., et al. 2011, Astronomy & Astrophysics, 526, A142
Masai, K. 1984, Astrophysics and Space Science, 98, 367
Matsuhara, H., Shibai, H., Onaka, T., & Usui, F. 2005, Advances in Space Research, 36, 1091
McKee, C. F. 1974, The Astrophysical Journal, 188, 335
McKee, C. F. & Ostriker, J. P. 1977, The Astrophysical Journal, 218, 148
Mereghetti, S., Israel, G. L., & Stella, L. 1998, Monthly Notices of the Royal Astronomical Society, 296, 689
Mitsuda, K., Bautz, M., Inoue, H., et al. 2007, Publications of the Astronomical Society of Japan
Muno, M. P., Clark, J. S., Crowther, P. A., et al. 2006, The Astrophysical Journal, 636, L41
Nakamura, R., Bamba, A., Ishida, M., et al. 2009, Publications of the Astronomical Society of Japan, 61, S197
Nomoto, K., Tominaga, N., Umeda, H., Kobayashi, C., & Maeda, K. 2006, Nuclear Physics A, 777, 424
Nozawa, S., Itoh, N., & Kohyama, Y. 1998, eprint arXiv:astro-ph/9804204
Olausen, S. A. & Kaspi, V. M. 2014, The Astrophysical Journal Supplement Series, 212, 6
Ostriker, J. P. & Gunn, J. E. 1969, The Astrophysical Journal, 157, 1395

Ouyed, R., Leahy, D., & Koning, N. 2014, Astrophysics and Space Science, 352, 715
Ozawa, M. 2010, Ph. D theisis, Kyoto University
Ozawa, M., Koyama, K., Yamaguchi, H., Masai, K., & Tamagawa, T. 2009, The Astrophysical Journal, 706, L71
Palmer, D. M., Barthelmy, S., Gehrels, N., et al. 2005, Nature, 434, 1107
Palomba, C. 2000, Astronomy and Astrophysics
Pandey, c. 1996, Astronomy and Astrophysics
Parmar, A. N., Oosterbroek, T., Favata, F., et al. 1998, Astronomy and Astrophysics
Patel, S. K., Kouveliotou, C., Woods, P. M., et al. 2001, The Astrophysical Journal, 563, L45
Porquet, D., Mewe, R., Dubau, J., Raassen, A. J. J., & Kaastra, J. S. 2001, Astronomy and Astrophysics, 376, 1113
Raymond, J. C. & Smith, B. W. 1977, The Astrophysical Journal Supplement Series, 35, 419
Rea, N., Israel, G. L., Pons, J. A., et al. 2013, The Astrophysical Journal, 770, 65
Rea, N., Pons, J. A., Torres, D. F., & Turolla, R. 2012, The Astrophysical Journal, 748, L12
Regimbau, T. & de Freitas Pacheco, J. A. 2001, Astronomy and Astrophysics, 374, 182
Rho, J. & Petre, R. 1997, The Astrophysical Journal, 1
Ripero, c., Garcia, c., Rodriguez, c., et al. 1993, IAU Circ.
Romano, P., Mangano, V., Cusumano, G., et al. 2011, Monthly Notices of the Royal Astronomical Society: Letters, 412, L30
Sasaki, M., Kothes, R., Plucinsky, P. P., Gaetz, T. J., & Brunt, C. M. 2006, The Astrophysical Journal, 642, L149
Sasaki, M., Plucinsky, P. P., Gaetz, T. J., & Bocchino, F. 2013, Astronomy & Astrophysics, 552, A45
Sasaki, M., Plucinsky, P. P., Gaetz, T. J., et al. 2004, The Astrophysical Journal, 617, 322
Sato, T., Bamba, A., Nakamura, R., & Ishida, M. 2010, Publications of the Astronomical Society of Japan, 62, L33
Schure, K. M., Kosenko, D., Kaastra, J. S., Keppens, R., & Vink, J. 2009, Astronomy and Astrophysics, 508, 751
Schwope, A. D., Hambaryan, V., Haberl, F., & Motch, C. 2005, Astronomy and Astrophysics, 441, 597
Sedov, c. 1959, Similarity and Dimensional Methods in Mechanics
Serlemitsos, P. J., Soong, Y., Chan, K.-W., et al. 2007, Publications of the Astronomical Society of Japan, 59, S9
Shklovskii, I. S. 1962, Soviet Astronomy, 6
Sofue, Y., Takahara, F., & Hirabayashi, H. 1983, Astronomical Society of Japan, 35, 447
Spitzer, c. 1962, Physics of Fully Ionized Gases
Staelin, D. H. & Reifenstein, E. C. 1968, Science (New York, N.Y.), 162, 1481
Sutherland, R. S. & Dopita, M. A. 1993, The Astrophysical Journal Supplement Series, 88, 253
Takahashi, T., Abe, K., Endo, M., et al. 2007, Publications of the Astronomical Society of Japan
Tatematsu, c., Fukui, c., Nakano, c., et al. 1987, Astronomy and Astrophysics (ISSN 0004-6361), 184, 279
Tatematsu, c., Nakano, c., Yoshida, c., Wiramihardja, c., & Kogure, c. 1985, Astronomical Society of Japan, 37, 345
Tatematsu, K., Fukui, Y., Iwata, T., Seward, F. D., & Nakano, M. 1990, \apj, 351, 157
Taylor, A. R., Gibson, S. J., Peracaula, M., et al. 2003, The Astronomical Journal, 125, 3145

Taylor, G. 1950, Proceedings of the Royal Society A: Mathematical, Physical and Engineering Sciences, 201, 175
Tendulkar, S. P., Cameron, P. B., & Kulkarni, S. R. 2012, The Astrophysical Journal, 761, 76
Tendulkar, S. P., Cameron, P. B., & Kulkarni, S. R. 2013, The Astrophysical Journal, 772, 31
Thompson, C. & Duncan, R. C. 1995, Monthly Notices of the Royal Astronomical Society, 275, 255
Tian, W. W., Leahy, D. A., & Li, D. 2010, Monthly Notices of the Royal Astronomical Society: Letters, 404, L1
Tiengo, A., Esposito, P., Mereghetti, S., et al. 2013, Nature, 500, 312
Tong, H. 2014, The Astrophysical Journal, 784, 86
Torii, K., Tsunemi, H., Dotani, T., et al. 1999, The Astrophysical Journal, 523, L69
Truelove, J. K. & McKee, C. F. 1999, The Astrophysical Journal Supplement Series, 120, 299
Tucker, W. H. & Gould, R. J. 1966, The Astrophysical Journal, 144, 244
Usov, V. V. 1994, The Astrophysical Journal, 427, 984
Vink, J. 2008, Advances in Space Research, 41, 503
Vink, J. 2011, The Astronomy and Astrophysics Review, 20, 49
Vink, J. & Kuiper, L. 2006, Monthly Notices of the Royal Astronomical Society: Letters, 370, L14
Vogel, J. K., Hascoët, R., Kaspi, V. M., et al. 2014, The Astrophysical Journal, 789, 75
Woltjer, L. 1972, Annual Review of Astronomy and Astrophysics, 10, 129
Woods, P. M. 2004, in AIP Conference Proceedings, Vol. 714 (AIP), 298–301
Woods, P. M., Kouveliotou, C., Finger, M. H., et al. 2007, The Astrophysical Journal, 654, 470
Wu, J. H. K., Hui, C. Y., Huang, R. H. H., et al. 2013, Journal of the Korea Space Science Society, 30, 83
Yamaguchi, H., Ozawa, M., Koyama, K., et al. 2009, The Astrophysical Journal, 705, L6
Zhou, P., Chen, Y., Li, X.-D., et al. 2014, The Astrophysical Journal, 781, L16

Acknowledgement

First of all, I am deeply grateful to Prof. Kazuo Makishima for his continuous guidance and kindly help. I greatly appreciate my colleague, Mr. Soki Sakurai and Mr. Makoto Sasano. I could not finish this thesis without their help. I would like to thank Dr. Teruaki Enoto, Dr. Junko. S. Hiraga, Dr. Hideki Uchiyama and Prof. Hidehiro Kaneda for helpful comments about analysis.

I would also like to thank my predecessors, especially Mr. Kenta Nakajima, Mr. Hirofumi Noda, Mr. Hiroyuki Nishioka and Mr. Shunsuke Torii (old M2s), Mr Shin'ya Yamada and Mr. Takayuki Yuasa. I had a very enjoyable time with them. I would also like to thank most of the members of the Hongo X-ray laboratory. Mr. Hiroaki Murakami, Mr. Shogo Kobayashi and Mr. Terukazu Nishida, I was surprised by your wonderful abilities. I am looking forward to further progress in X-ray astronomy by new doctoral students in our laboratory, Mr. Katsuma Miyake, Mr. Koh Ono and Mr. Yuichi Kato. Mr Yoshihiro Furuta and Ms. Yuuki Murota, It was a short while, but I had a good time with you.

I am very proud to be surrounded by many marvelous people in my life so far, especially Mr. Kenji Takahashi, Mr. Shinji Takahashi (T's guitar) and Mr. Yu Kinoshita (Kino Factory). I am taking a different field now, however, I never forget what I learned from working with you. When I am in trouble, I always remember that. Finally, I would like to thank my grandfather.

This work is supported by Grant-in-Aid for JSPS Fellows.